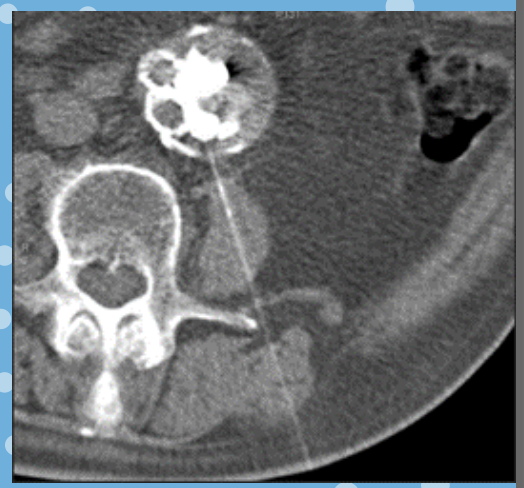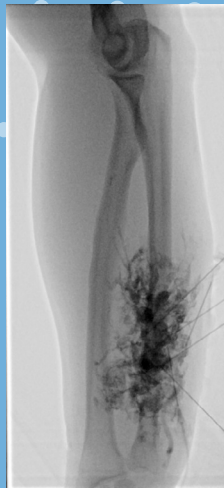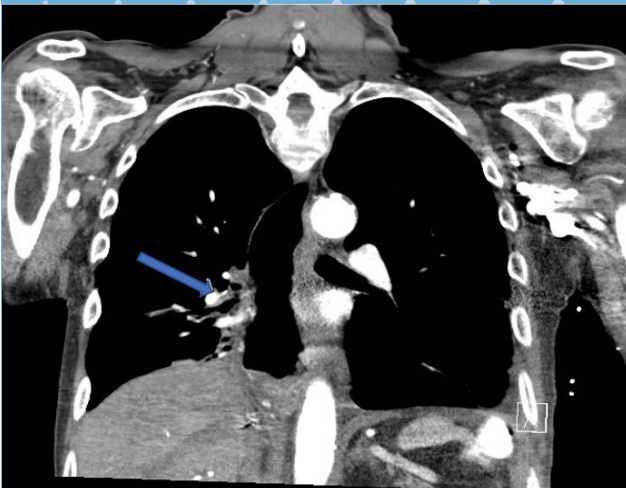# 2022 RADIOLOGY DEPARTMENTAL RESEARCH SYMPOSIUM

Thursday, October 20, 2022

UNC School of Dentistry
University of North Carolina

160 Dental Circle Drive | Chapel Hill, NC 27514

UNC | SCHOOL OF MEDICINE
Radiology

Table of Contents

Front cover images taken by the following individuals, left to right:
Image 1
Stephen M Himmelberg, UNC Medical student
Marinelda Perleshi, UNC Medical student, researcher
Clayton Commander, MD, PhD, Assistant Professor of UNC Radiology, Vascular Interventional Radiology

Image 2
Kyung Rae Kim, MD, Associate Professor of UNC Radiology, Vascular Interventional Radiology

Image 3
Johannes du Pisanie, MD, 5th-year UNC Radiology Integrated Interventional Radiology Resident
Clayton Commander, MD, PHD, Assistant Professor of UNC Radiology, Vascular Interventional Radiology
Hyeon Yu, MD, Professor of UNC Radiology, Vascular Interventional Radiology
Charles Burke, MD, Professor of UNC Radiology, Vascular Interventional Radiology

Welcome Letters

Dear Colleagues:

Welcome to the 2022 Radiology Departmental Research Symposium! This day will highlight advances in clinical and translational imaging research by showcasing the research of our faculty, fellows, residents, medical students, and graduate trainees. We have accepted a total of 40 poster presentations and 8 oral presentations to be presented throughout the day. In addition, we will also host Sharmila Majumdar, PhD and Bruce Rosen, MD, PhD as our keynote speakers.

This symposium is also a tremendous opportunity for our clinical and radiological sciences faculty to network and find others that share common scientific interests. I hope that you are able to use this opportunity to form future collaborations and research endeavors. For those of you who are unable to step away from the reading rooms, we hope that you can join virtually and attend the in-person sessions as able. Please also join me at the conclusion of the day for the happy hour to conclude the celebration of the Department's research accomplishments.

I am grateful for the work of the planning committee for their efforts in putting this event together over the past several months. We were very fortunate to have many members of the Department involved in reviewing and scoring abstracts as well as reviewing presentations for the selection of awards for our trainees.

Thank you for participating in this special day for the Department!

Sincerely,

Maureen Kohi

Maureen P. Kohi, MD, FSIR, FCIRSE, FAHA
Ernest H. Wood Distinguished Professor and Chair

RESEARCH SYMPOSIUM KEYNOTE PRESENTATION: MORNING SESSION

Kirkland Auditorium, Koury Oral Health Sciences Building UNC Adams School of Dentistry

9 a.m. - 10 a.m., Thurdsay, October 20, 2022

"Intelligent Imaging: The role of deep learning and Artificial Intelligence (AI) in Imaging"

SHARMILA
MAJUMDAR, MD, PhD

Margaret Hart Surbeck Distinguished Professor in Advanced Imaging & Vice Chair for Research, The University of California, San Francisco

Dr. Majumdar serves as the Executive and Scientific Director at the Center for Intelligent Imaging, and as Director Musculoskeletal and Quantitative Imaging Research Group, in the department. She holds courtesy appointments as Professor in the Departmentts of Orthopedic Surgery and Bioengineering & Therapeutic Sciences. Dr. Majumdar has led NIH funded programs in musculoskeletal diseases, run industrial collaborations and clinical trials, and has a strong focus on diversity with numerous diversity supplements associated with her NIH awards.

Dr. Majumdar has served as the mentor for 49 post-doctoral fellows, providing both direct research supervision and guidance in establishing independent positions. As a senior faculty member in her department, she has also mentored junior faculty members, advising them on the various aspects required for establishing research programs, teaching experience, and other requirements for promotion and a successful career.

She has been a strong advocate for women researchers,

students, and staff. Dr. Majumdar has been/is an active member of the ISMRM, participated in annual meetings from the earliest days in 1983, when the two MR societies were separate entities; missing only a few for life events, such as growing her family. She was one of the earliest members of the musculoskeletal study group, served as a member of various ISMRM committees, given educational courses, chaired sessions, and actively supports ISMRM members. She is a strong proponent of career development, advocacy for women, support for under-represented researchers, and junior colleagues.

She was selected as a fellow of the American Institute of Medical and Biological Engineers in 2004 and a fellow of the International Society of Magnetic Resonance in Medicine (ISMRM) in 2008. In 2007, the UCSF Haile T. Debas Academy of Medical Educators at UCSF awarded her the "Excellence in Direct Teaching and/or Excellence in Mentoring and Advising Award". She was awarded the ISMRM Gold medal in 2016. She is a Distinguished Investigator of the Academy of Radiology Research.

RESEARCH SYMPOSIUM KEYNOTE PRESENTATION: AFTERNOON SESSION

Kirkland Auditorium, Koury Oral Health Sciences Building UNC Adams School of Dentistry

12 p.m. - 1 p.m., Thurdsay, October 20, 2022

"Advances in Neuroimaging"

BRUCE
ROSEN, MD, PhD

Laurence Lamson Robbins Professor of Radiology AND
Vice Chair of Research, Harvard Medical School

Dr. Bruce Rosen is Director of the Athinoula A. Martinos Center for Biomedical Imaging at Massachusetts General Hospital and is the Vice Chair of Research in the Department of Radiology at Massachusetts General Hospital. Dr. Rosen received his MD degree from Hahnemann Medical College in Philadelphia in 1982 and his PhD degree from MIT in 1984, and subsequently completed an internship and residency at Mass General and research fellowships at Mass General and the Harvard-MIT Division of Health Sciences and Technology (HST). He joined the faculty of Harvard Medical School in 1987.

Dr. Rosen has received numerous awards in recognition of his contributions to biomedical imaging, including the Outstanding Researcher award from the Radiological Society of North America (RSNA) and the Rigshospitalet's International KFJ Prize from the University of Copenhagen/Rigshospitalet. He is a Fellow of the International Society for Magnetic Resonance in Medicine (ISMRM); a Gold Medal winner from ISMRM for his contributions to the field of functional neuroimaging; a Fellow of the American

Institute for Medical and Biological Engineering; and a member of the Institute of Medicine of the National Academies, the American Academy of Arts and Sciences, and the National Academy of Inventors.

Among his many achievements in the biomedical sciences, Dr. Rosen is a pioneer in the field of functional neuroimaging. In the early 1990s, he oversaw development of the technique functional magnetic resonance imaging (fMRI), which measures the hemodynamic and metabolic changes associated with brain activity in both health and disease. More recently, his work has focused on the integration of fMRI data with information from other imaging modalities, including positron emission tomography (PET), magnetoencephalography (MEG) and noninvasive optical imaging. Many of the tools he has introduced are now used by research centers and hospitals around the world to study and evaluate patients with stroke, brain tumors, dementia, and neurologic and psychological disorders.

8:30 AM - 8:50 AM   **Catered Breakfast and Registration**
Main Street (Ground Floor)

8:50 AM - 9:00 AM   **Opening Remarks**
Kirkland Auditorium

9:00 AM - 10:00AM   **Keynote Lecture 1**
Sharmila Majumdar, MD, PhD
"Intelligent Imaging: The role of deep learning and Artificial Intelligence (AI) in Imaging"
Kirkland Auditorium

10:00 AM - 10:05AM   **Break**

10:05 AM - 10:30AM   **Terry Magnuson**
"Introduction to the School of Data Science and Society"

10:30 AM - 11:10AM   **Oral Presentations Session 1**
Kirkland Auditorium

11:10AM - 12:00 PM   **Catered Lunch**
Main Street (Ground Floor)

12:00 PM - 1:00 PM   **Keynote Lecture 2**
Bruce Rosen, MD, PhD
"Advances in Neuroimaging"
Kirkland Auditorium

1:00 PM - 1:15 PM   **Break**

1:15 PM - 2:15 PM   **Oral Presentations Session 2**
Kirkland Auditorium

2:15 PM - 2:30 PM   **Presentation of Awards & Prizes**
Kirkland Auditorium

2:30 PM - 4:00 PM   **Poster Presentations**
Main Street (Ground Floor)

4:00 PM - 6:00 PM   **Happy Hour**
Atrium

— Oral Presentations —

— Poster Presentations —

21 **Longitudinal development of regional cerebellar volumes during the first 800 days**
Ya Wang, MD

22 **Neural network on cortical surfaces for prediction of infant cognitive scores**
Jiale Cheng, PhD

24 **A Longitudinally-consistent Deep Framework for Joint Subcortical Segmentation and Registration of Infant Brains**
Liangjun Chen, PhD

25 **Four-dimensional Mapping of Dynamic Subcortical Development of Infant Brains**
Liangjun Chen, PhD

26 **Evaluation of paraspinous muscle signal fat fraction using chemical shift encoded MRI: Comparison with CT attenuation**
Clayton W. Commander, MD, PhD

27 **CT Fluoroscopy-Guided Percutaneous Direct type II Endoleak Embolization using n-BCA Glue**
Lourens du Pisanie, MD, PGY5

29 **Imaging utilization of acute trauma in a resource-poor setting: Analysis of the Malawi trauma surveillance registry**
Jordan Taylor, MD, PGY3

30 **Sarcopenia and Associated Imaging Biomarkers in Patients Undergoing Transjugular Intraheaptic Portosystemic Shunt Placement**
Vedang J. Patel, MS4

31 **Radiation Safety Education and Diagnostic Imaging in Pediatric Patients with Surgically Treated Hydrocephalus: The Patient and Family Perspective**
Diane M. Armao, MD

32 **Case Report: Pituitary adenoma associated with xanthogranuloma**
Peter Noone, MD

33 **Prevalence of exposures that modify breast density prior to breast cancer screening**
Ley A. Killeya-Jones, PhD

34 **Interactions between Bifidobacterium and Bacteroides and human milk oligosaccharides are associated with infant cognition**
Seoyoon Cho, MS, Graduate Student

35 **Advanced MRI Imaging of the Ascending Auditory Pathway to Evaluate Hearing Loss**
Pirapat M. Rerkpattanapipat, MS2

36 **Healthy Eating Indices are associated with early cognitive and temperament development**
Jiarui Tang, Graduate student

37 **The development and application of a cost-effective cervical spine phantom for use in fluoroscopically guided lateral C1-C2 puncture training**
Victoria Risner, MS3

38 **A retrospective chart review exploring lesion characteristics, treatment, and outcomes of adenoid cystic carcinoma of the breast**
Victoria Risner, MS3

39 **19F Cenya BEACONs magnetic resonance imaging parameter optimization**
Sang Hun Chung, PhD

40 **Association of Liver Reporting and Data System Treatment Response (LR-TR) and modified Response Evaluation Criteria in Solid Tumor (mRECIST) Classification Systems for Stereotactic Body Radiation Therapy (SBRT)-treated Hepatocellular Carcinoma (HCC) Lesions**
Diwash Thapa, MS4

41 **Transcatheter Fluoroscopic Embolization of Rabbit Fallopian Tube Using n-butyl-2-cyanoacrylate (NBCA): A Pilot Study for Non-Surgical Sterilization**
Diwash Thapa, MS4

43 **Charting normal knee cartilage thickness trajectories and localizing individual cartilage changes using data from the entire Osteoarthritis Initiative cohort**
Tengfei Li, PhD

44 **Lumps and Bumps around the Gallbladder Fossa: A potential LI-RADS pitfall**
Naishal Patel, MS4

46 **Predictors of Recommended Follow-up after a Positive Lung Cancer Screening Examination**
Louise M. Henderson, PhD

47 **Lung Cancer Screening In Individuals With And Without Lung-related Comorbidities**
Eman M. Metwally MD-PhD

48 **Uncommon Causes of Hemoptysis: A Post-surgical Case Study**
Stephen M. Himmelberg, MS4

49 **Clinical developments of a stationary head CT using CNT x-ray source arrays**
Alex Billingsley, Graduate student

Abstract # - 03: TI-RADS: Improving patient care or just a pain in the neck, a retrospective review

Tyler Rogers, Anthony Dyer, Jacob Nelson, Ellie Lee, Katrina McGinty

University of North Carolina, Chapel Hill, NC

Background: The purpose of this study was to evaluate the American College of Radiology Thyroid Imaging Reporting and Data Systems (TI-RADS) by correlating TI-RADS score with biopsy results to validate or reaffirm the recommendation of fine needle aspiration (FNA) in the higher scoring nodules. Other covariables investigated included patient age, gender, FDG avidity on Positron Emission Tomography (PET), and echogenic foci as possible independent predictors of malignancy.

Materials and Methods: This was a retrospective study performed at a large academic institution. 624 nodules underwent ultrasound (US) examination and US-guided FNA over a three-year period. Chart review included: age, gender, TI-RADS score, presence of echogenic foci, nodule size, pathology from FNA, and method of detection. Both TI-RADS scoring and FNA of nodules were performed by abdominal fellowship trained radiologists. Results were categorized as benign, indeterminate, or malignant based on the Bethesda System for Reporting Thyroid Cytopathology or non-diagnostic.

The study implemented a multinomial logistic regression model where the TI-RADS category was the main independent variable, with the following control variables: gender, age, echogenic foci, and PET detection. Additionally, the study evaluated all possible 2-way interactions of control variables using a backwards elimination strategy to remove interactions with $p<0.05$. An ordinal logistic regression was used to determine if higher TI-RADS scores were associated with higher probability of malignancy.

Results: The percentage of malignant nodules in each TI-RADS (TR) category were as follows: TR 2- 0%, TR 3-4.9%, TR 4-3.6%, TR 5-16.3%. The odds ratio for a 1-unit increase in TIRADS was 3.16 [95% CI: 1.25, 7.98, $p=0.015$] for malignant pathology, consistent with increasing malignant risk with increasing TI-RADS score. No control variables or 2-way interactions were significant.

Conclusion: The study supports the use of the TI-RADS model at our institution. The higher TI-RADS scores were significantly associated with malignant pathology on FNA. This validates the recommendation of FNA in nodules with higher TI-RADS scores.

Clinical relevance statement: The higher TIRADS scores were associated with higher probability of malignant pathology at FNA. The decision to biopsy thyroid nodules should continue to be based on TIRADS score.

Statement Regarding Human Subjects: This is an IRB approved retrospective chart review that did not require informed consent or HIPAA authorization. All identifying patient information has been removed.

Statement Regarding Conflicts of Interest: The authors have no conflicts to disclose

Abstract # - 4 Comparison of Iterative Reconstruction and Post Reconstruction Deep Learning Noise Reduction Methods utilizing Philips Brilliance iCT 256 Phantom Data and Clinical Images

Michael Winkler, MD[1]; Martin Halicek, MD,PhD[2]; Akira Hasegawa, PhD[3]; Anobel Maghsoodpour PhD[2]

[1]UNC Chapel Hill, Dept of Radiology, Chapel Hill, NC. [2]Medical College of Georgia, Augusta, GA. [3]AlgoMedica, Inc, Sunnyvale, CA

Introduction: The quality of coronary computed tomographic angiography (CCTA) post processing is dependent on special noise reduction (NR) techniques, such as Iterative Reconstruction (IR). While IR lowers noise amplitude, it also lowers central noise frequency (CNF), distorting margins and adding a waxy quality to CCTA images. Fortunately, new deep learning (DL) NR algorithms preserve CNF maintaining sharp image features without distortion. The most versatile of these new NR techniques is applicable after filtered back projection (FBP) and is thus vendor agnostic. In this presentation, we validate the relative CNF stability of an FDA-approved DL algorithm (PixelShine, AlgoMedica Inc) through Noise Power Spectrum (NPS) analysis, comparing its performance to that of the IR NR methods of a major CT vendor. We also provide a gallery of clinical comparisons.

Methods: Phantom data was obtained with a Brilliance iCT 256 scanner (Philips) using 120 kVp and a wide range of mAs settings. Images were created via two IR methods (iDose and IMR) and with application of PixelShine to FBP images. The NPS of each image was obtained. CNF Ratio (CFR) and Noise Magnitude Ratio (NMR) were calculated to compare the noise frequency distribution and amplitude of NR of the three methods. The results were correlated qualitatively to CCTA images created with each technique.

Images
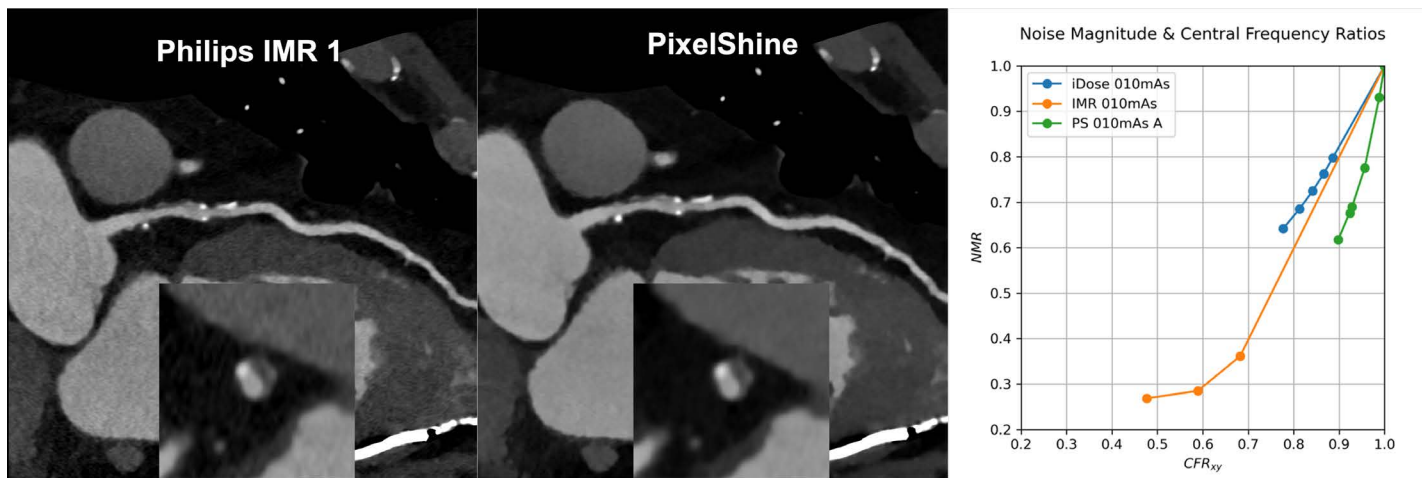
Results: While iDose and IMR obtained NMRs as low as 0.65 and below 0.3, the CFR was shifted to values as low as 0.8 and 0.5 respectively, introducing undesired blurriness. PixelShine produced NMRs as low as 0.55 while still maintaining CFR values above 0.85. Clinical CCTA axial and post processed images (e.g., CPR and 3D reconstructions) also demonstrated the superior noise texture of PixelShine.

Conclusion: Compared to iDose and IMR, PixelShine produces comparable NR while maintaining central frequency fidelity.

_____

Abstract # - 17 The synthesis and evaluation of 64Cu labeled Neurotensin Receptor antagonists for thera-nostic application

Xinrui Ma; Tao Zhang, PhD; Muyun Xu, PhD; German Fonseca Cabrera, PhD; Zhanhong Wu, PhD; Zibo Li, PhD

Biomedical Research Imaging Center, University of North Carolina, Chapel Hill, NC

Introduction: Accumulating evidence suggests that neurotensin (NTS) and neurotensin receptors (NTSRs) play key roles in lung cancer progression by triggering multiple oncogenic signaling pathways including PKC/ERK and AKT. Recently, several attempts have been made to synthesize radiometal labeled NTRS agents, most of which demonstrated only moderate tumor uptake and retention. The aim of this study is to develop novel NTSR1 targeted agents for both imaging and therapy applications.

Methods: A series of NTR antagonists were synthesized with variable propylamine (PA) linker length and different chelators, including 64Cu-CB-iPA-NT (i=1, 2, 3), 64Cu-NOTA-2PA-NT, 64Cu-DOTA-2PA-NT, and 64Cu-DOTA-2PA-NT-VS. Radiolabeling reactions were performed under 95-degree heating for CB precursors, while 37 degrees for NOTA and DOTA precursors. Western blot was used to determine NTR expression in human lung cancer cell lines. We assessed the candidate compounds' in vitro binding affinity to H1299 cells. To evaluate the agents' biodistribution properties, small animal PET/CT scans were performed using H1299 xenografts at 2, 4, 24, and 48h post injection.

Images

[⁶⁴Cu]Cu-CB-1PA-NT	[⁶⁴Cu]Cu-CB-2PA-NT	[⁶⁴Cu]Cu-CB-3PA-NT
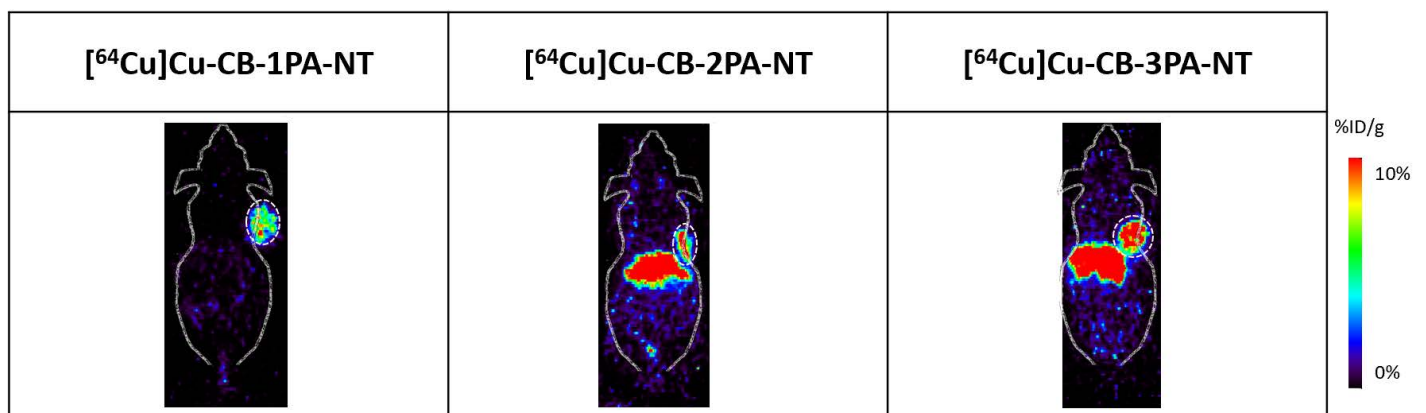
Results: NTSR1 was confirmed to have high expression in H1299 cells by western blot. NT-CB-2PA showed good binding affinity towards H1299 cells with IC50 to be 3.038 nM. Small animal PET/CT showed prominent tumor uptake, high tumor-to-background contrast, and long tumor retention up to 48 h post

injection. The lead agent, NT-CB-2PA, demonstrated 8.41±1.33 %ID/g tumor uptake, which was maintained at 9.72±4.89 %ID/g at 48h. Moderate liver uptake (7.72±4.68 %ID/g at 48h) was observed along with low uptake in most other organs. Compared to NT-CB-2PA, NT-CB-1PA had a lower background including low liver uptake at 24h and 48h after injection (0.27 ± 0.14 %ID/g at 24h and 0.08 ± 0.05 %ID/g at 48h) while tumor uptake remained high (6.06 ± 2.28 %ID/g at 24h and 4.52 ± 1.90 %ID/g at 48h). Meanwhile, CB-3PA showed increased uptake in both tumor and liver.

Conclusions: Through the side-by-side comparison, CB-2PA-NT was identified as the lead agent for further evaluation based on its high and persistent tumor uptake and moderate liver uptake. The success of this theranostic approach will not only lead to an accurate imaging-based method to efficiently detect NTSR1 expression in lung cancer (for diagnosis, patient screening, and treatment monitoring), but also the radionuclide-based agent for lung cancer therapy.

Statement Regarding Human Subjects: This study does not involve human subjects.

Statement Regarding Conflicts of Interest: A patent related has been filed.

_____

Abstract # - 20 Regionally Specific Efficiency Development of Brain Functional Networks in Infancy

Weixiong Jiang, Guoshi Li, Weiyan Yin, Gang Li, Li Wang, Brittany Howell, Martin Styner, Han Zhang, Dinggang Shen, Weili Lin

University of North Carolina at Chapel Hill, Chapel Hill, NC

Background
The infant brain experiences rapid growth in the first few years of life. Previous graph theory-based studies on infant brain networks have mainly focused on the global network topology. Yet, regional features may be unique and sensitive to the development of early cognitive abilities.

Materials and Methods: Leveraging a longitudinal, large cohort infant fMRI dataset (UNC/UMN Baby Connectome Project) acquired from typically developing infants during natural sleep, we aimed to uncover regional efficiency-based developmental trajectories and their associations with cognitive abilities. With an infant-dedicated fMRI processing pipeline, we first quantified region-specific topological efficiency using nodal global efficiency and nodal local efficiency; then characterized different developmental trajectories using a linear, log-linear (natural logarithm), and a quadratic age model based on linear mixed effect regression; finally we assessed the associations between efficiency changes and various infant cognitive abilities.

Results: Our results revealed a highly complex, spatiotemporally heterogeneous development of nodal global (Figure 1A) and local efficiency (Figure 1B) , particularly, we revealed the nonlinear development during the infancy. In addition, the trajectory of the regional global efficiency at the left temporal occipital fusiform and bilateral occipital fusiform gyrus was positively associated with cognitive abilities ($P < 0.05$, FDR corrected) (Figure 1C), including visual reception, expressive language, receptive language, and early learning composite scores, while these associations were weakened with age ($P < 0.05$, FDR corrected).

Conclusion: In this study, we depicted the regional developmental trajectory day by day using linear and nonlinear models for the first time and revealed their association with cognition. These results provided evidence of continuingly optimized brain networks at local levels, and new insights into regional developmental features of brain topologies and their associations with cognitions.

Clinical Relevance: The developmental trajectories of nodal efficiency obtained from typically developing children could serve as normative data to early identify children who may deviate from normal trajectories so as to, potentially, provide timely interventions and minimize or even avoid long-term neurodevelopmental disabilities.

Images
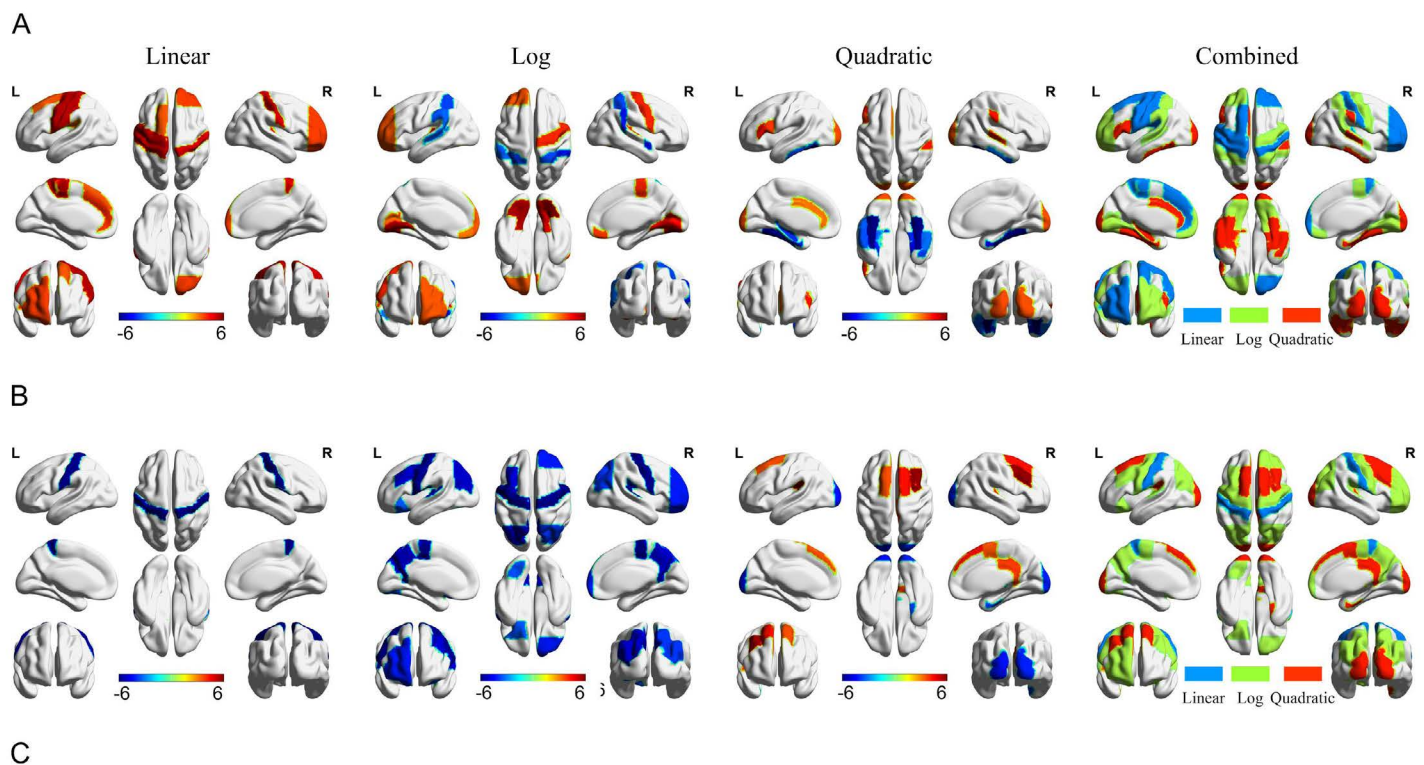
	TOF_L vs ELC			OFG_L vs ELC			OFG_R vs ELC			OFG_L vs RLS			OFG_R vs VRS			OFG_L vs ELS			OFG_R vs ELS		
	β	T	P	β	T	P	β	T	P	β	T	P	β	T	P	β	T	P	β	T	P
(Intercept)	0.0165	0.23	0.8173	0.0440	0.65	0.5130	0.0411	0.64	0.5198	0.1134	2.60	0.0096	0.0951	1.96	0.0502	0.0610	1.22	0.2224	0.0949	1.98	0.0487
Site	0.0034	1.39	0.1647	0.0013	0.61	0.5400	-4.36E-04	-0.20	0.8416	0.0015	0.70	0.4841	-5.10E-04	-0.23	0.8155	8.22E-04	0.39	0.6962	-0.0010	-0.4	0.6653
Gender	0.0042	1.90	0.0585	-1.01E-05	-0.01	0.9957	-0.0022	-1.16	0.2474	2.31E-04	0.12	0.9018	-0.0024	-1.23	0.2212	-5.69E-05	-0.03	0.9754	-0.0024	-1.2	0.2214
CogScore	9.46E-04	2.90	3.89E-03 *	8.88E-04	2.88	0.0041 *	8.25E-04	2.83	0.0048 *	0.0023	2.89	0.0040 *	0.0022	2.63	0.0087 *	0.0032	3.57	3.96E-04 *	0.0023	2.66	0.0080 *
ln(d)	0.0415	3.55	4.26E-04 *	0.0370	3.37	8.12E-04 *	0.0366	3.46	6.02E-04 *	0.0258	3.58	3.85E-04 *	0.0283	3.52	4.79E-04 *	0.0351	4.24	2.68E-05 *	0.0289	3.59	3.71E-04 *
ln(d):CogScore	-1.49E-04	-2.78	5.75E-03 *	-1.42E-04	-2.83	0.0049 *	-1.32E-04	-2.72	0.0067 *	-3.69E-04	-2.78	0.0057 *	-3.63E-04	-2.56	0.0107 *	-5.32E-04	-3.54	4.40E-04 *	-3.88E-04	-2.6	0.0086 *

*: P<0.05 with FDR corrected. TOF: temporal occipital fusiform cortex; OFG: occipital fusiform gyrus; ELC: early learning compisite score; VRS: visual receptive score; RLS: receptive language score; ELS: expressive language score; L: left; R: right.

Figure 1. Significant early development of nodal global efficiency (A) and nodal global efficiency (B), and Significant association between cognitive scores and nodal global efficiency development using a linear cognitive model (P < 0.05, FDR corrected). T-value from the model fitting was showed in A and B after FDR correction (P < 0.05) and model selection.

Statement Regarding Human Subjects: UNC/UMN Baby Connectome Project was approved by the Institutional Review Boards at UNC/UMN. Written informed consent was obtained from a parent or guardian prior to any study procedures.

Statement Regarding Conflicts of Interest: The authors have no conflicts to disclose

Abstract # - 23 Is routine follow-up chest radiography required in all patients following computed tomography-guided lung biopsy?

Jared T. Weinand, MD; Johannes du Pisanie, MD; Clayton Commander, MD, PhD; Hyeon Yu, MD

UNC Hospitals, Chapel Hill, NC

Background: Chest radiography is routinely performed to evaluate for pneumothorax after CT-guided lung/pleural lesion biopsy. This study was performed to help determine the utility of routine one-hour post procedural chest radiograph for the detection of pneumothorax (PTX) following computed tomography-guided lung biopsy.

Materials and Methods: Patient and procedure data were collected from all lung biopsy cases performed at a single center between May 2014 and August 2021. Inclusion criteria necessitated procedural computed tomography (CT) guidance, biopsy of a lung nodule/mass, age greater than 18, immediate post procedure CT, one-hour post procedure chest radiograph (1hr-CXR), and final pathology results.

Results: A total of 308 lung biopsies were reviewed. A total of 276 cases performed in 267 patients were included. All patients with symptomatic and/or increasing PTX on post procedural imaging (CT or 1hr-CXR) underwent chest tube placement. Eighty-five (30.9%) PTXs were detected in total. Seventy-six (27.6%) PTXs were first detected on post-procedure CT and 9 (3.3%) PTXs were first detected on 1hr-CXR. Chest tubes were placed in 7 (8.2%) patients, all of whom had PTX first detected on CT. No patient with PTX first detected on 1hr-CXR required chest tube placement. Five (6%) patients with PTX on post procedural CT underwent PTX aspiration with none having PTX on 1h-CXR.

Conclusion: Routine use of follow-up chest radiography may not be required in patients who do not have PTX on post lung biopsy CT unless they develop symptoms of PTX during recovery.

Clinical Relevance: This study lends evidence to help improve periprocedural management of patients undergoing lung nodule biopsy.

Images
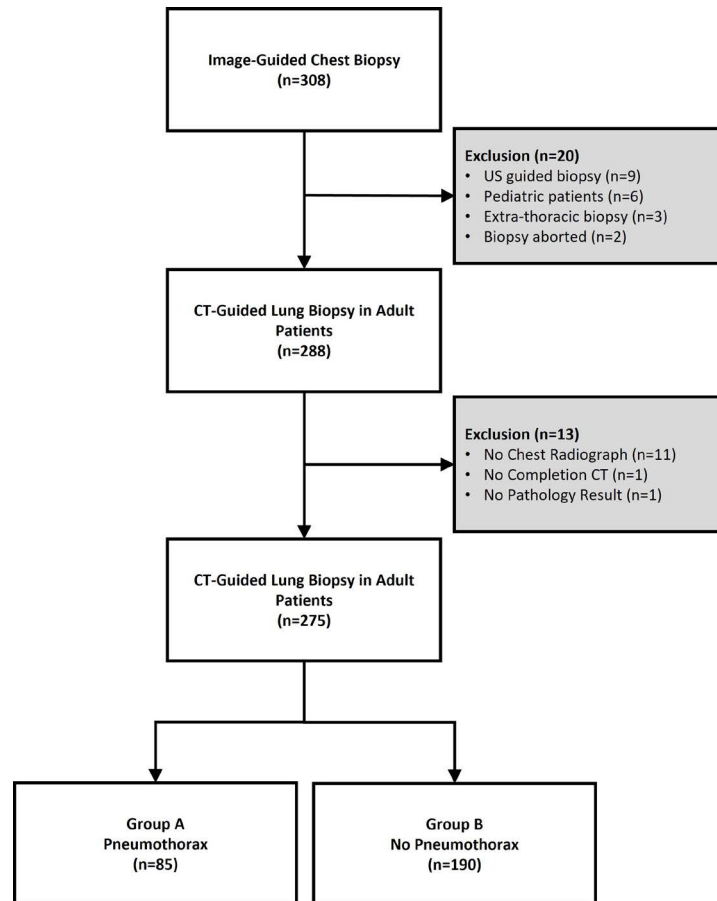
```
Image-Guided Chest Biopsy
(n=308)
```

Exclusion (n=20)
• US guided biopsy (n=9)
• Pediatric patients (n=6)
• Extra-thoracic biopsy (n=3)
• Biopsy aborted (n=2)

```
CT-Guided Lung Biopsy in Adult
Patients
(n=288)
```

Exclusion (n=13)
• No Chest Radiograph (n=11)
• No Completion CT (n=1)
• No Pathology Result (n=1)

```
CT-Guided Lung Biopsy in Adult
Patients
(n=275)
```

```
Group A
Pneumothorax
(n=85)
```

```
Group B
No Pneumothorax
(n=190)
```

Statement Regarding Human Subjects: This study was approved by the Institutional Review Board with waiver of informed consent and was compliant with the Health Insurance Portability and Accountability Act.

Statement Regarding Conflicts of Interest: The authors have no conflicts to disclose.

_____

Abstract # - 28 Incidence of Reversible Superior Ophthalmic Vein Dilatation in Adult Patients with Trauma

Joshua Schoen, MD; Sheng-Ch Hung MD

UNC Hospitals, Chapel Hill, NC

Background: Dilated superior ophthalmic vein (SOV) is thought to be an uncommon radiographic finding after head injury and is associated with a wide spectrum of etiologies ranging from reversible dilatation secondary to intubation and increased intracranial pressure to life-threatening situations, such as carotid-cavernous sinus fistula and venous thrombosis, which requires additional vascular imaging work-up. The authors seek to investigate the prevalence of SOV dilatation and prevalence of its reversibility in patients imaged for trauma indications with available follow-up imaging, as well as the presence of factors that may be associated with SOV dilatation reversibility.

Materials & Methods: Consecutive adult head CT studies performed for trauma indications over three months at one Level 1 trauma center were reviewed and patients with a second follow-up head or maxillofacial CT imaging performed within one week to six months were selected. Bilateral SOV diameters were measured on axial series and patients were sorted into dilated (one or both SOV diameters ≥ 2.5 mm) and non-dilated (<2.5 mm). SOV diameters were measured on follow-up imaging to evaluate for resolution or persistence of SOV dilatation. Finally, patient imaging reports and medical records were reviewed for factors that were considered possibly associated with SOV dilatation, including: body mass index (BMI), gender, intracranial hemorrhage, skull base fracture, intracranial mass, presence of endotracheal tube or tracheostomy, chronic obstructive pulmonary disease, and acute chest trauma.

Results: Head CT imaging of 851 individuals between January and March 2021 was reviewed. 116 of these individuals had subsequent CT imaging and were selected for SOV measurement. 25% (29/116) of these individuals had unilateral or bilateral dilated SOVs on initial imaging. On follow-up imaging, 10 of 29 (34.5%) had resolution of SOV dilatation. The group with reversible SOV dilatation has a trend to have smaller BMI than the non-reversible group (23.2 ± 4.8 vs. 28.5 ± 7.5, P = 0.055). There is no significance in other factors between the groups with reversible and nonreversible SOV dilatation.

Conclusions/ Clinical Relevance: SOV dilatation in the trauma population is more common than expected, with a relatively high rate of reversibility. The findings suggest that further vascular imaging in asymptomatic individuals in similar populations for incidentally noted SOV dilatation may not be warranted.

Statement Regarding Human Subjects: Waiver of informed consent and HIPAA authorization granted after IRB review.

Statement Regarding Conflicts of Interest: The authors have no conflicts of interest to disclose.

_____

Abstract # - 42 Whole Body Skeletal Tomosynthesis Scanner Based on Carbon Nanotubes (CNT) X-ray Sources

Diwash Thapa, BS; Alex Billingsley, BS; Yueting Luo, PhD; Christy Inscoe, PhD; Jianping Lu, PhD; Otto Zhou, PhD; Yueh Lee, MD, PhD

University of North Carolina School of Medicine, Chapel Hill, NC.

Background: Conventional tomosynthesis is performed with specific anatomy within a limited field of view (FOV). Extended FOV tomosynthesis is beneficial for whole-body skeletal imaging in austere environments due to tomosynthesis' increased fracture detection sensitivity. Current research and commercial systems are built on large gantries making them unsuitable for mobile applications. We present a novel tomosynthesis system built with carbon nanotubes (CNT) x-ray sources, herein named orthogonal tomosynthesis (OT). We test different reconstruction algorithms and characterize system attributes.

Materials and Methods: OT consists of a linear x-ray tube positioned orthogonally to a small FOV area detector. Sources are collimated to a rectangular strip on the detector and projections are acquired in a step-and-shoot image acquisition scheme as shown in figure 1 a. In preprocessing, all projections from a given source were stitched. Reconstructions were performed with two algorithms: simultaneous iterative

reconstruction technique (SIRT) and simultaneous algebraic reconstruction technique (SART). Entrance dose at 100 cm source to detector distance was measured using the RaySafe X2 R/F sensor (figure 1 b) and the dose area product (DAP) within the FOV was calculated. Projection space scatter to primary ratio (S/P) and scatter degradation factor (SDF) was calculated.

Results: Reconstruction images using SIRT and SART are displayed in figure 1 c, d. Ten iterations of SIRT and two of SART was enough for convergence. The compiled SIRT algorithm took 3.44 s while SART took 21.6 s for completion. Both reconstructions were found to be anatomically correct and provided good resolution of all osseous structures. With collimation, DAP was calculated to be 170.0 mGy whereas without collimation DAP was 207.1 mGy to image the 540 cm2 FOV of the chest phantom reconstructions. The average S/P and SDF with collimation across all sources was 0.31 and 0.77 while the same was 0.69 and 0.59 respectively without the collimator.

Conclusion: This work demonstrates the feasibility of the OT system. Due to collimation, this system has significantly reduced scatter (> 50% decrease in S/P), and radiation (18% decrease in DAP) burden compared to conventional tomosynthesis.

Clinical Relevance: The OT system presented here can be mounted on the back of an ambulance for trauma imaging. The reduced scatter and radiation also makes OT suitable for repetitive use such as scoliosis imaging.
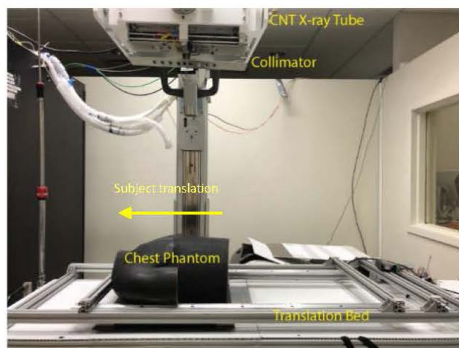
Images

Figure 1 a: System Setup of CNT-based orthogonal tomosynthesis scanner

Figure 1 b: Entrance dose measurement within the collimated field with the RF probe

Figure 1 c: SIRT recon with 10 convergent iterations at the level of the thoracic vertebrae

Figure 1 d: SART recon with 2 convergent iterations at the level of the thoracic vertebrae

Statement Regarding Human Subjects: No human subjects were used.

Statement Regarding Conflicts of Interest: The authors do not have any COI.

_____

Abstract # - 45 Examining Patient Characteristics and Digital Breast Tomosynthesis Choice

Louise Henderson, PhD; Michael Pritchard; Thad Benefield, MS

University of North Carolina, Chapel Hill, NC

Background: Screening with digital breast tomosynthesis (DBT) is reported to reduce recall rates and increase cancer detection rates. In an effort to reduce monetary barriers to prevention, many insurance providers in the United States now cover screening DBT. We sought to determine the characteristics of women who, when given the choice between 2D digital mammography (DM) and DBT, choose screening DBT, and to evaluate recall rates on DM versus DBT.

Methods: We utilized data from mammography facilities that offer DBT and DM based on woman's preference and that participate in a North Carolina population-based breast imaging registry. We included 23,476 exams from 19,026 women ages 40-79 years who underwent screening DBT or DM between 1/2/2015 and 4/4/2018. We explored whether patient differences exist in screening DBT use by implementing multilevel random effects logistic regression models, controlling for woman-level and facility-level correlations and adjusting for multiple comparisons. Given the large sample size, we also calculated Cohen's H values to evaluate clinical significance. Finally, we compared recall rates for DBT and DM.

Results: Approximately half of screening exams were performed with DBT (49.3% n=11,527) and half with DM (50.7%, n=11,904). Patient characteristics associated with increased screening DBT use included white race (p<0.0001), increasing age (p<0.0001), public insurance (p-value<0.0001), dense breasts (p=0.0025), personal history of breast cancer (p=0.0007), family history of breast cancer (p<0.0001), and a prior breast biopsy (p<0.0001). Cohen's H values ranged from 0.044 for the breast density comparison to 0.471 for the comparison of public versus other insurance. Adjusted recall rates were significantly lower for DBT versus DM (3.8% vs. 4.7% respectively, p=0.0015).
Conclusions: Despite financial coverage for screening DBT, women with known risk factors were more likely to request and undergo screening DBT than DM.

Clinical Relevance: Efforts to educate women on emerging breast imaging modalities will allow women the opportunity to make informed choices.

Statement Regarding Human Subjects: This study has a wavier of both informed consent and HIPAA authorization.

Statement Regarding Conflicts of Interest: The authors have no conflicts of interest to disclose

Abstract # - 2 Evaluation of Coronary Artery Calcification using Gated StationaryChest Tomosynthesis Through 4D Extended Cardiac-torso (XCAT) Phantom Simulation

Umer Ahmed Sh, Christy R. Inscoe, Shuang Xu, Truc Nguyen, Yueh Z. Lee

University of North Carolina School of Medicine, Chapel Hill, NC

Background: A rapidly expanding body of literature has provided evidence that coronary calcium (CAC) scoring has a strong positive predictive value for future major adverse coronary events (MACEs). CAC scoring relies upon cardiac computed tomography (CT), which is associated with high radiation dose and cost. Thus, routine imaging to monitor changes in CAC scores is impractical with CT. Our carbon nanotube-based (CNT) gated stationary digital chest tomosynthesis system (SDCT) provides a low radiation, low cost, and potentially portable alternative. In this study, we aimed to evaluate the ability of SDCT to perform CAC scoring using 4D digital phantom software, which allows for the generation of lesions of different sizes and densities in different coronary vessels.

Materials and Methods: We evaluated the ability of this system to perform CAC scoring using a 4D extended cardiac-torso (XCAT) phantom software, which allowed us to generate digital phantoms with varying levels of calcification in different coronary vessels. A total of six phantoms were generated with calcified plaques of either low or high density in segments of the right coronary, left circumflex, or left anterior descending vessels. Each phantom was then scanned through both CT and SDCT projector software, which enabled simulated images to be generated. CAC scoring was performed on both sets of images and then compared.

Results: CAC scoring of the CT images using the Agatson method demonstrated that five of the phantoms fell within the moderate range of CAC scores (100-399) and one phantom was in the severe range (400-999). Scoring of the SDCT images was performed by attaining total area of the plaque in all slices. Correlation of the SDCT plaque total area and CT Agatson score resulted in an R^2 of 0.607. Average difference between SDCT plaque total area and CT Agatson score was 1361.6, 95% CI [-2440.3, 5163.5]. Conclusion: SDCT is a potential alternative to CT for routine monitoring of CAC scores. Next steps include CAC scoring using patients in our physical SDCT system and exploring the importance of wider angle tomosynthesis for calcium scoring

Clinical Relevance Statement: Our carbon nanotube-based gated stationary digital chest tomosynthesis system provides a low radiation, low cost, and potentially portable alternative to CT for routine monitoring of coronary calcium scores in patients.
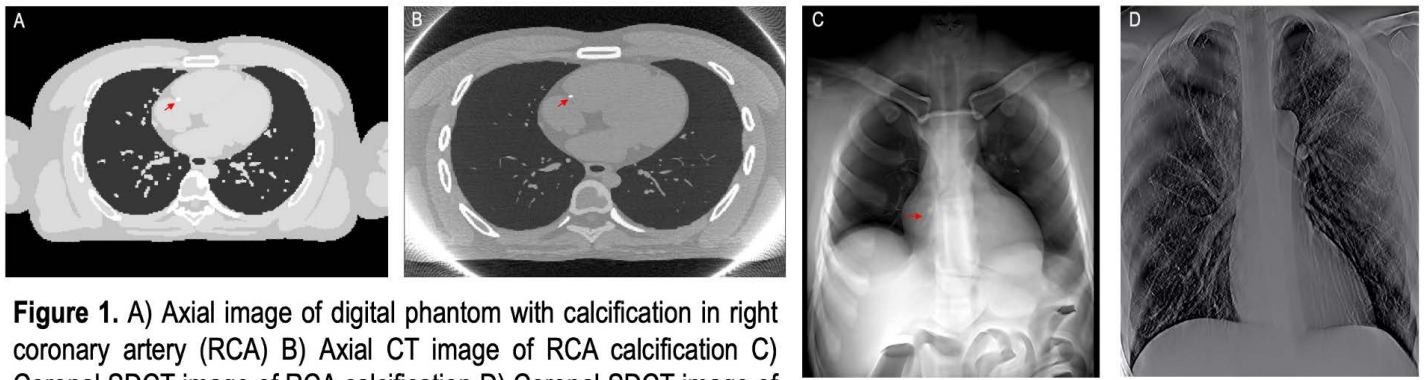
Images

Figure 1. A) Axial image of digital phantom with calcification in right coronary artery (RCA) B) Axial CT image of RCA calcification C) Coronal SDCT image of RCA calcification D) Coronal SDCT image of a real patient

Statement Regarding Conflicts of Interest: Authors have no conflicts to disclose

_____

Abstract # - 5 Comparing the variability of two validated, quantitative breast density measures used in a community-based mammography registry across race and ethnicity

Brianna D. Taffe, MPH[1,2]; Louise Henderson, PhD, MSPH[2]; Cherie M. Kuzmiak, DO, FACR, FSBI[2]; Despina Kontos, PhD[3]; Sarah J. Nyante PhD, MSPH[2]

[1]UNC Gillings School of Global Public Health, Chapel Hill, NC. [2]UNC School of Medicine, Chapel Hill, NC. [3]University of Pennsylvania Perelman School of Medicine, Philadelphia, PA

Background: Breast density (BD), an independent predictor of breast cancer risk, can be quantified in two ways: area-based (2-dimensional (2D)) or volumetric (3-dimensional (3D)). Prior studies have shown that 2D and 3D measures vary by race/ethnicity. We compared the consistency of the relationship between two validated BD measures across racial and ethnic groups.

Materials and Methods: This study used data from 920 women aged 18+ who received a full-field digital screening mammogram at 1 of 6 breast imaging facilities in North Carolina (2017-2018). Race and ethnicity were abstracted from electronic medical records. Quantitative BD was measured from mammograms using (1) 2D estimates of dense breast tissue and total breast area from the Laboratory for Individualized Breast Radiodensity Assessment (LIBRA); and (2) 3D estimates of breast fibroglandular tissue and total breast volume from Volpara. Percent density was calculated as the ratio of dense/fibroglandular tissue to total breast area/volume. Spearman correlation coefficients (R) and 95% confidence intervals (CI) were used to quantify associations between 2D and 3D measures.

Results: Participants were 33-86 years old (M=57.9, SD=11.2) and identified as White (73%), Black (19%), Asian (3%), Other race (6%), and Hispanic ethnicity (5%). Percent density measures were highly correlated, with strong correlations across groups (White: R=0.88, 95% CI: 0.86, 0.90; Black: R=0.81, 95% CI: 0.75, 0.85; Asian: R=0.91, 95% CI: 0.81, 0.96; Other: R=0.86, 95% CI: 0.77, 0.92; Hispanic: R=0.82, 95% CI: 0.71, 0.90; non-Hispanic: R=0.88, 95% CI: 0.87, 0.90). Correlations between the 2D and 3D measures were lower

and consistent across racial groups (White: R=0.41, 95% CI: 0.35, 0.47; Black: R=0.42, 95% CI: 0.29, 0.54; Asian: R=0.33, 95% CI: -0.07, 0.64; Other: R=0.55, 95% CI: 0.32, 0.72). The correlation between the 2D and 3D measures was stronger among Hispanic vs. non-Hispanic women (R=0.62, 95% CI: 0.41, 0.76 vs. R=0.39, 95% CI: 0.33, 0.44); however, the difference was not statistically significant.

Conclusion: Correlations between 2D and 3D density measures were consistent across racial/ethnic groups. Studies with greater representation of Asian and Hispanic women are needed for precise estimates in these groups.

Clinical Relevance: These data suggest that use of 2D vs. 3D measures is unlikely to contribute to between-study heterogeneity in racial/ethnic differences for studies of BD in diverse populations.

Statement Regarding Human Subjects: This research was conducted under a waiver of informed consent and HIPAA authorization confirmed by the University of North Carolina Institutional Review Board.

Statement Regarding Conflicts of Interest: The authors have no conflicts to disclose.

_____

Abstract # - 6 Is Tele-guidance the Future for Rural Emergencies?

Eric M. Cal, MS3

University of North Carolina at Chapel Hill School of Medicine, Chapel Hill, North Carolina

Background: Point-of-care-ultrasound (POCUS) improves diagnostic accuracy and expedites lifesaving procedures. Remote and rural areas disproportionately underutilize ultrasound (US) because of a dearth of US training. The Butterfly IQ tele-guidance function allows remote guidance of image acquisition. The aim of this study was to investigate whether tele-guidance improved US image acquisition by untrained sonographers

Materials and Methods: To determine the effectiveness in tele-guidance for US image acquisition, participants with no US or medical experience gathered US images of the heart, right kidney, and gallbladder of a standardized patient. All participants watched a 10 minute US education video and then were randomized into the control or experimental group. The experimental group was assisted by a trained radiologist with the Butterfly tele-guidance feature for their scans while the control group received no assistance. Time to image capture was recorded for both groups and the images were graded by 4 blinded diagnostic radiologists using the RACE tool. Group differences were determined with independent t-test of time of image acquisition, image interpretability, and image quality for each landmark imaged. Associated Cohen's d effect sizes for each comparison were also reported

Image:

Time to Acquisition			
	Heart	Right Kidney*	Gallbladder*
Control	97 ± 0.04 sec	80 ± 0.02 sec	138 ± 0.05 sec
Experimental	20 ± 0.02 sec	21 ± 0.03 sec	33 ± 0.02 sec
RACE Score: Overall Quality			
	Heart*	Right Kidney*	Gallbladder*
Control	0.8 ±0.4	0.2 ±0.4	0.2 ±0.4
Experimental	1 ±0	1 ±0	1 ±0
RACE Score: Image Generation			
	Heart*	Right Kidney*	Gallbladder*
Control	2.6 ±1.36	0.6 ±1.2	0.6 ±1.2
Experimental	4.75 ± 0.43	5 ± 0	4.25 ± 0.83
*denotes a difference between the control and experimental group			

Results: Images of 10 participants have been processed. The preliminary results show there is significant difference in the time to image acquisition for the right kidney (p=0.005; d=2380) and the gallbladder (p=0.042; d=2625) between the groups. There was also significant difference between the RACE scores for overall quality and image generation for the heart (p=0.0311; d=2.02), right kidney (p=0.00034; d=4.85), and gallbladder (p=0.0025; d=3.45). The overall RACE score for images obtained for by the control group corresponded to the descriptor "Image quality too poor to permit interpretation" while the experimental group was "Good image quality, meaningful image interpretation easy"

Conclusion: Tele-guidance improves the time to image acquisition and the clinical applicability of US images obtained by untrained sonographers. Further data collection and processing is required to expand on this exploratory finding.

Clinical Relevance: The ability for tele-guidance to allow untrained sonographers to obtain interpretable US images in reasonable time can allow for expanded POCUS use in low resource areas and improved patient care.

Statement Regarding Human Subjects: All participants consented to study participation and HIPAA authorization was obtained appropriately.

Statement Regarding Conflicts of Interest: No conflicts of interest to disclose

_____

Abstract # - 7 Factors Affecting Adverse Events after Venous Malformation Sclerotherapy: Single Vascular Anomalies Center Experience

Kyung Rae Kim, MD

University of North Carolina School of Medicine Department of Radiology, Chapel Hill, NC

Background: To evaluate the factors affecting adverse events in percutaneous sclerotherapy for venous malformation (VM).

Materials and Methods: A retrospective review was performed of consecutive patients who received sclerotherapy for VM from 2016 to 2021. VM characteristics (locations, tissue planes and overlying skin involvements) and sclerotherapy details (sclerosants and concentration, dilution method and ratio) were analyzed. Anticoagulation based on D-dimer level was also evaluated. Cutaneous and non-cutaneous adverse events were analyzed.

Results: Three-hundred-one sclerotherapies in 137 patients (median age 19.0 years; interquartile range, 12.8–31.5) were enrolled. VM involving tissue planes were subcutaneous (n=104), intramuscular (n=84), and combined (n=113). Overlying skin involvement was observed in 56%. Sodium tetradecyl sulfate (STS) was mainly used (83%). Periprocedural anticoagulation was used in 16%. Most adverse events were minor, 9.7% (30/301), and major was only 1.7% (5/301) (21 cutaneous and 14 non-cutaneous adverse events). Young age, STS mixed with Lipiodol, and increased treatment sessions affected adverse events. Age under 18 (odds ratio [OR], 4.4502; 95% confidence interval [CI], 1.5607-12.6890; P = .0052), and overlying skin involvement (OR, 7.1794; 95% CI, 1.6226-31.7656; P = .0094) were predictors of cutaneous adverse events. All non-cutaneous adverse events developed in intramuscular VMs, but this association was not statistically significant. There was no severe hematologic adverse event or permanent consequence.

Conclusion: The overall adverse event rate after VM sclerotherapy was 11.6%, but major adverse events were rare (1.7%). Cutaneous adverse events were associated with young age and overlying skin involvement. All non-cutaneous adverse events developed in intramuscular VMs.

Clinical Relevance: The adverse events associated with VM sclerotherapy are preventable and can be appropriately managed with the knowledge of the potential risk factors.

Images

Statement Regarding Human Subjects: The institutional review board approved this study and waived the need for informed consent.

Statement Regarding Conflicts of Interest: The author has no conflicts of interest.

_____

Abstract # - 8 Unsupervised cross-site functional MRI harmonization for automated brain disease identification

Yuqi Fang[1], Guy Potter[2], Mingxia Liu[3]

[1]Department of Radiology and Biomedical Research Imaging Center, University of North Carolina at Chapel Hill, Chapel Hill, NC. [2]Department of Psychiatry and Behavioral Sciences, Duke University Medical Center, Durham, NC. [3]Department of Radiology and Biomedical Research Imaging Center, University of North Carolina at Chapel Hill, Chapel Hill, NC

Background: Resting-state functional magnetic resonance imaging (rs-fMRI) data have been widely used for automated brain disease diagnosis to assist in timely intervention. Multi-site fMRI data have been increasingly employed to augment sample size and improve statistical power for investigating brain disease identification. However, previous studies usually suffer from significant inter-site heterogeneity caused for instance by differences in scanners and/or scanning protocols.

Materials and Methods: We develop a novel discrepancy-based cross-site fMRI harmonization framework (called UFH-Net) for automated brain disease identification. The proposed UFH-Net is designed to model spatio-temporal fMRI patterns of labeled source and unlabeled target samples via an attention-guided graph convolution module, and also leverage a maximum mean discrepancy constrained module for unsupervised cross-site feature alignment between two sites.

Results: Two datasets with rs-fMRI data, i.e., REST-meta-MDD (681 subjects) and ADNI (109 subjects), are used to validate the effectiveness of our proposed method. For REST-meta-MDD, we achieve a promising AUC score of 62.5% in differentiating major depressive disorder patients from healthy controls. For ADNI, we achieve an AUC score of 57.94% in classifying patients with early mild cognitive impairment (MCI) from those with late lMCI.

Conclusion: A cross-site fMRI harmonization framework is designed for automated brain disease identification. Extensive experiments verify the robustness and generalizability of our method.
Clinical Relevance: Our method helps reduce significant inter-site fMRI heterogeneity, a common problem in clinical practice. In particular, our method helps localize disease-related functional connectivity abnormalities and associated brain regions, and therefore, can facilitate fMRI-based analysis of brain diseases.

Images
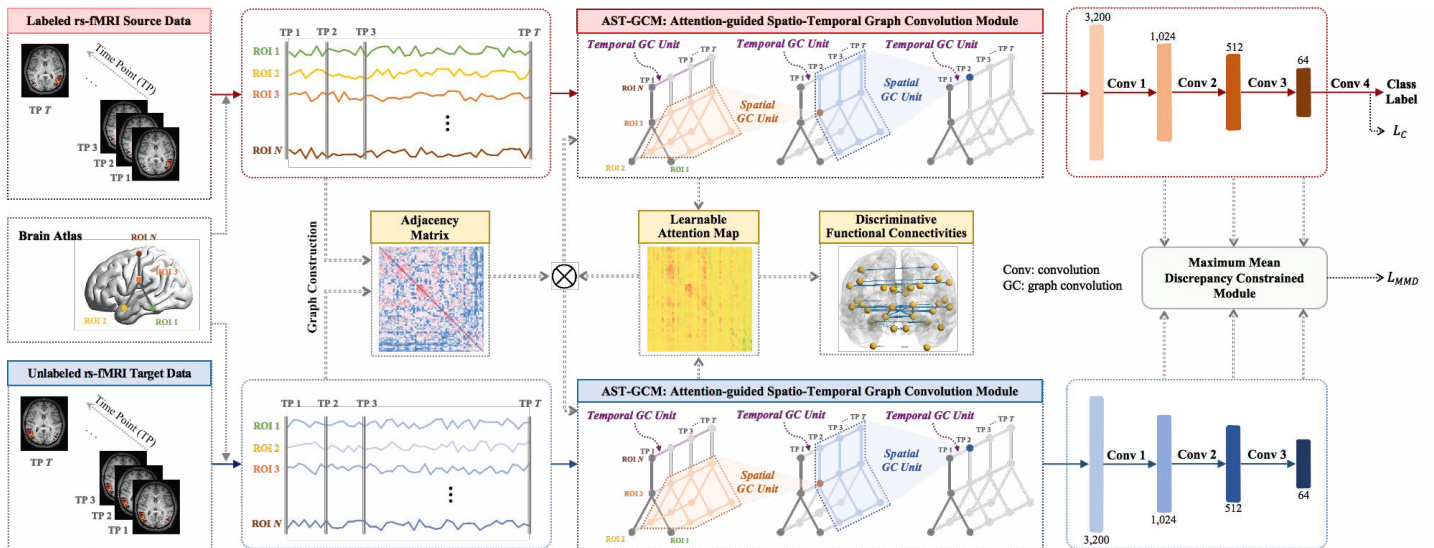
Statement Regarding Conflicts of Interest: The authors have no conflicts.

Abstract # - 9 Human brain atlases across a century of life

Sahar Ahmad, Ph.D; Ye Wu; Zhengwang Wu; Kim-Han Thung; Siyuan Liu; Weili Lin; Gang Li; Li Wang; Pew-Thian Yap

University of North Carolina, Chapel Hill, NC

Background: Human brain atlases integrate structural and functional information in common reference spaces, model age-specific developmental patterns over the life course, and are indispensable for identifying aberrant brain development and maturation. Here, we introduce the first set of age-specific brain surface-volume atlases spanning birth to 100 years of life.

Materials And Methods: To construct the lifespan atlases, we used brain MRI data from five Lifespan Human Connectome Projects (HCPs): (i) developing HCP, 37 - 41 gestational weeks; (ii) Baby Connectome Project, 2 weeks to 5 years; (iii) HCP Development, 5.5 to 22 years; (iv) HCP Young Adult, 22 to 37 years; and (v) HCP Aging, 36 to 100 years. We preprocessed the Baby Connectome Project data using iBEAT v2.0 and used minimal preprocessed data of rest of the studies.

We first construct atlases at four reference time points i.e., 1, 16, 30, and 60 years. For each reference time point, the tissue segmentation maps of subjects scanned within the time window are spatially normalized using surface-constrained dynamic elasticity model based groupwise registration. Then, we compute the atlases by weighed averaging of the warped intensity images and cortical surfaces, and fusing the warped tissue segmentation maps via majority voting.

With these reference atlases, we construct the lifespan atlases by registering the images of the subjects scanned within a time window for each time point to the corresponding reference atlas and then warping the reference atlas with the weighted averaged displacement fields. Our lifespan atlases are defined at birth, every month during infancy and early childhood, every year during middle childhood, every four years during

late childhood and adolescence, every five years during young adulthood, and every twenty years during middle and late adulthood.

Images
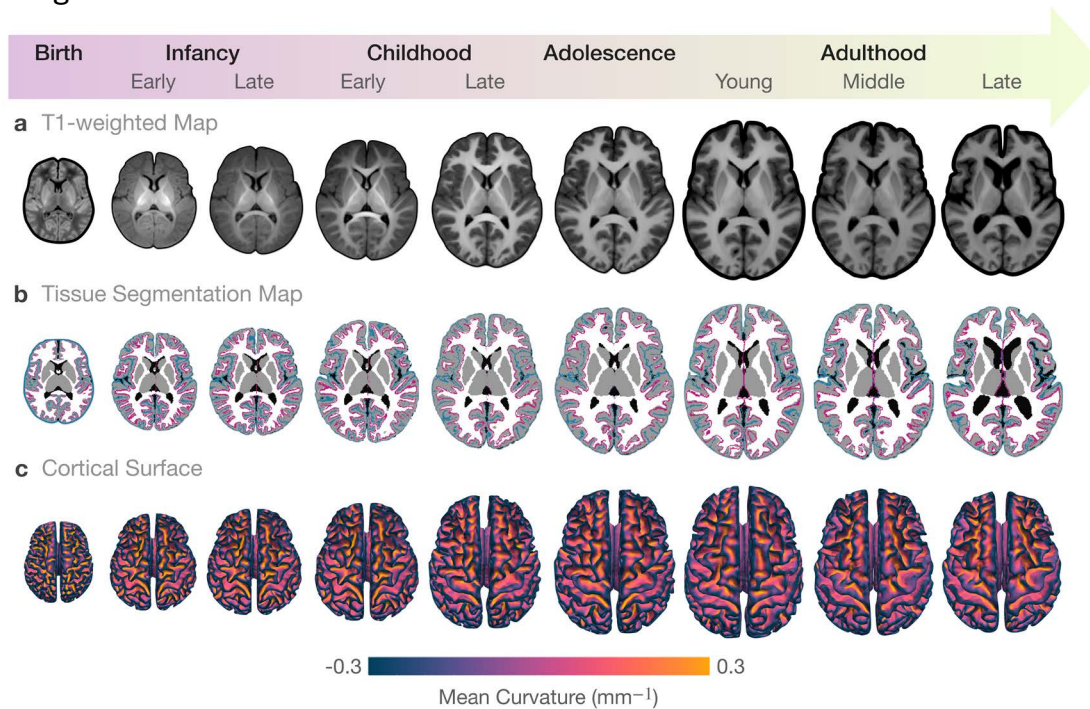
Results: Our brain atlases faithfully capture coarse- and fine-scale anatomical details, preserve typical cortical folding patterns across the human lifespan, and are consistent in surface-volume spaces (Figure 1).

Conclusion: We presented a novel set of surface-volume brain atlases spanning birth to 100 years of life. Our atlases preserve structural fidelity both in image volumes and cortical surfaces.

Clinical Relevance: Our surface-volume atlases provide a unified reference framework to chart brain development and maturation across the lifespan, which can be used to study age-related neurodegeneration.

Statement Regarding Human Subjects: Informed consent was obtained from the participants of all studies involved.

Statement Regarding Conflicts of Interest: The authors declare no conflict of interest.

_____

Abstract # - 10 Use of Radiofrequency Tip Wire to Cross Ureteral Anastomotic Obstruction for Placement of Retrograde Nephroureteral Stent

Venki Ramakrishnan, Rachel Brader, Peter Bream

University of North Carolina, Chapel Hill, NC

Learning Objectives: 1.Present a novel technique of utilizing the PowerWire™ radiofrequency wire to transverse ureteroenteric strictures in patients who have undergone creation of an ileal conduit status post cystectomy with prior failed placement of a retrograde nephroureteral stent. 2.Describe the technical aspects of this procedure. 3.Outline advantages and disadvantages of this technique.

Background: Radiofrequency (RF) tip wires are utilized in recanalization of central venous stenosis where standard practices to transverse occlusions have failed. In the literature, this wire has been utilized in urologic and non-urologic interventions. Ureteroenteric strictures after ileal conduit creation are identified as a late surgical complication. We propose a novel technique utilizing the PowerWire™ radiofrequency device to transverse ureteroenteric strictures in these patients when standard procedures have failed.

Case Details: We present three cases of distal ureteral occlusions at the ileal conduit anastomosis. In the first case, the patient developed a left ureteroenteric anastomotic stricture after ileal conduit creation. A RF wire was utilized to cross this stricture and a retrograde nephroureteral stent was placed. There was a minor complication of abscess formation which resolved with percutaneous drainage. In the second case, the patient developed a left ureteroenteric structure requiring placement of a left nephrostomy tube. During a future visit, internal stent placement with sharp recanalization was attempted but unsuccessful. In a follow up procedure, a RF wire successfully crossed the stricture and a left retrograde nephroureteral stent was placed. The final case is a patient who underwent cystectomy with ileal conduit formation. His post-operative course was complicated by bilateral ureteroenteric strictures. The left stricture was able to be traversed with successful placement of an internal stent. The right stricture was unable to be crossed and the patient returned for right ureteral recanalization. The RF wire was used to cross the right ureteral stricture. Balloon dilation of the stricture was performed resulting in extraluminal contrast extravasation. Subsequently a 7mm x 2.5 cm Viabahn stent graft (Gore, Flagstaff, AZ) was placed across the stricture with a retrograde nephroureteral stent.

Conclusion: The use of a radiofrequency wire is a feasible alternative for recanalization of ureteroenteric strictures after ileal conduit creation.

Statement Regarding Human Subjects: All cases did not require IRB approval.

Statement Regarding Conflicts of Interest: The authors have no conflict of interest to disclose.

_____

Abstract # - 11 One institutions' experience with a true standard 15 mCi dose of I-131 for the treatment of Graves' Disease

Mitchel Muhleman, MD; Ali Fahim; Thad Benefield, MS; Jorge Oldan MD; Amir Khandani, MD

University of North Carolina, Chapel Hill, NC

Introduction: In patients with Graves' Disease, radioactive iodine (RAI) is routinely used to ablate the thyroid gland with the goal of permanent hypothyroidism. Currently, there is a lack of consensus on the fixed dosage of RAI to be administered for this purpose between the main guideline frameworks set forth by the American Thyroid Association (ATA), Society of Nuclear Medicine and Molecular Imaging (SNMMI), European

Association of Nuclear Medicine (EANM) and the European Thyroid Association (ETA).
In this retrospective study, we will investigate the effectiveness of using a standard dose of 15 mCi +/- 10% of RAI in achieving a successful treatment of Graves' Disease at a single institution over a period of approximately 6.5 years.

Methods: This institution utilizes a two-day pre-image/uptake dosage, imaging/uptake measurement and treatment protocol. A retrospective chart review was conducted for the period between 5/1/2014 to 9/2/2020, to identify patients diagnosed with hyperthyroidism due to Graves' Disease. Additional inclusion criteria of the patients identified were treatments with 15 mCi +/- 10%. The exclusion criteria included age <18 years old at the time of treatment, incarceration, decisional impairment or lost to follow-up. The patients were grouped based on outcome and assessed for the efficacy of the dosage of 15 mCi +/- 10% of RAI in a successful treatment. For the purposes of this study, successful treatment is characterized as either permanent hypothyroidism or euthyroidism.

Results: 67 patients were identified that met the inclusion criteria between 5/1/2014 to 9/2/2020. The majority of the included individuals were women women (54 of 67, 80.6%). Of the 67 RAI ablations; 60 patients became hypothyroid (60 of 67, 89.55%), 2 euthyroid (2 of 67, 2.99%) and 5 remained hyperthyroid (5 of 67, 7.46%). The exploratory analysis did not identify any covariates associated with the failure outcome. Conclusions: For the treatment of Graves' Disease, the use of a standard low dose of 15 mCi +/- 10% with the aim of achieving an euthyroid or permanent hypothyroid state has a high success rate without additional measurements or calculations beyond a standard planar image and 24-hr uptake %. The adoption of a standard low dose of 15 mCi of I-131 across institutional guidelines would streamline dosage questions and eliminate the need to determine the weight of the thyroid for calculations in all RAI treatments for hyperthyroidism caused by GD.

Image
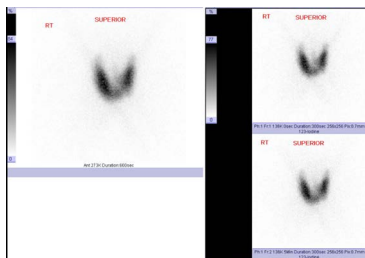
Statement Regarding Human Subjects: All patient identification information was removed from the data collected and no informed consent form was required.

Statement Regarding Conflicts of Interest: There was no conflict of interest involving this study.

_____

Abstract # - 12 Application of Strain-Promoted "Double Click" Reaction for PET Probe Construction

Manshu Li, PhD[1]; Xinrui Ma[1], Christopher J. Molnar[2]; Shuli Wang, PhD[1]; Zhanhong Wu, PhD1; Vladimir V Popik, PhD[2]; Zibo Li, PhD[1]
[1]BRIC-UNC Chapel Hill, Chapel Hill, NC. [2]University of Georgia, Athens, GA

Background: Utilization of radiolabeled prosthetic groups serve as the alternative strategy in PET agent constructions for ligands bearing complicated structures, of which the direct radiolabeling can oftentimes be challenging. However, the cross-couplings of prosthetic groups and cancer ligands are usually done in the radiochemistry cores with cyclotrons and hot cells. Due to the limited capacity of radiochemistry cores, only a small number of new PET agents can be designed and prepared. Meanwhile, many research groups that do not have access to the cyclotron cannot construct PET agents with their own ligands. In addition, most of the cross-coupling methods also suffer from low reaction rates, which require higher ligand loading for compensation. This is impractical in some cases considering the availability of valuable and expensive ligands. These factors created a bottleneck in new PET agent development.

Results and conclusions: To solve this bottleneck in new PET agent constructions, as well as to reduce the barrier to entry for new PET agent development, here we report the utilization of MC-DIBOD as the double-click cross-linking agent in strain-promoted azide-alkyne cyclization (SPAAC) [18F] PET agent constructions with several advantages: 1) Can be distributed from radiochemistry core to imaging facilities, simple ligand cross-coupling can be done outside of radiochemistry cores, allowing more research groups to construct their own PET agents; 2) Fast ligand coupling reaction rate minimizing the amount of valuable ligands needed; 3) Hydrophilicity of the final PET agent can be adjusted to achieve optimized imaging result; 4) Biorthogonal and potential implication in in-vitro and in-vivo labeling.

Images

Lipophilic PET agent   Hydrophilic PET agent
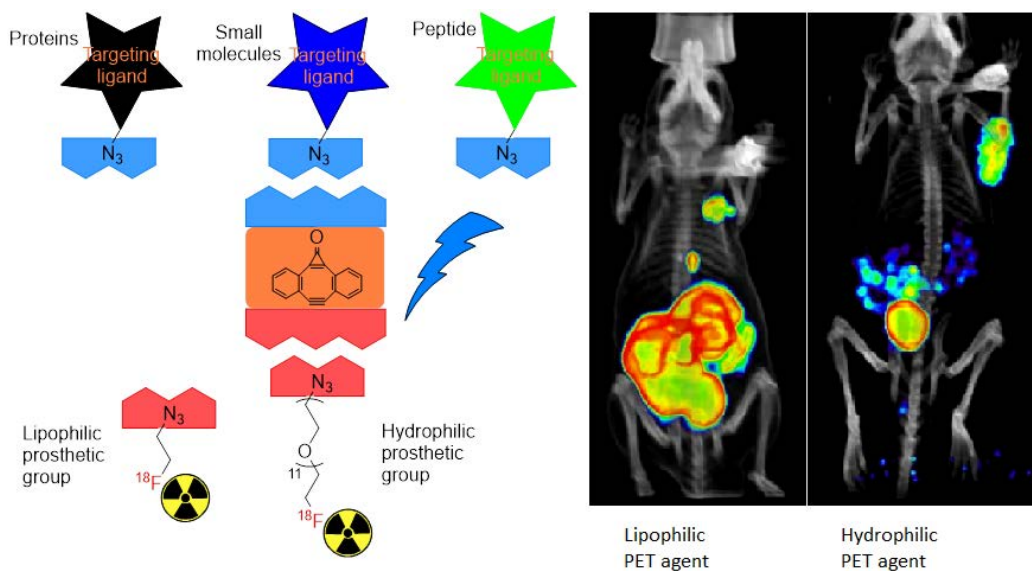
Abstract # - 13 Charting excitation-inhibition balance over the human lifespan

Guoshi Li, PhD; Hoyt Patrick Taylor, PhD; Ye Wu, PhD; Sahar Ahmad, PhD; Kim-Han Thung, PhD; Zhengwang Wu, PhD; Gang Li, PhD; Li Wang, PhD; Weili Lin, PhD; Pew-Thian Yap, PhD

University of North Carolina, Chapel Hill, NC

Background: Excitation-inhibition (E-I) balance is a fundamental property of neuronal circuits and abnormal E-I balance has been hypothesized to be a key driver for multiple brain disorders. However, to date there are still no normative reference charts for E-I balance that can be used to benchmark individual growth trajectory and to predict aberrant E-I balance for early detection of diseases. To fill this important gap, we applied a Multiscale Neural Model Inversion (MNMI) framework to high quality resting-state functional MRI (rs-fMRI) data from the Lifespan Human Connectome Projects (HCP) to chart the trajectory of E-I balance over human lifespan.

Materials and Methods: We modeled the whole-brain network dynamics with the biologically motivated Wilson-Cowan model and estimated excitatory/inhibitory connection strengths among neural populations based on rs-fMRI. The regional E-I balance was defined as the ratio of the recurrent excitation to inhibition strength. We included 100 subjects from the Baby Connectome Project (0-5 years), 100 subjects from the HCP Development (5-21 years), 77 subjects from the HCP Young Adult (22-35 years), and 125 subjects from the HCP Aging (36-100 years) (male: 200; female: 202). Regional BOLD time series were extracted using the Desikan-Killiany atlas with 68 cortical regions grouped into six functional networks (visual, somatomotor, salience, limbic, frontoparietal control and default mode).

Images
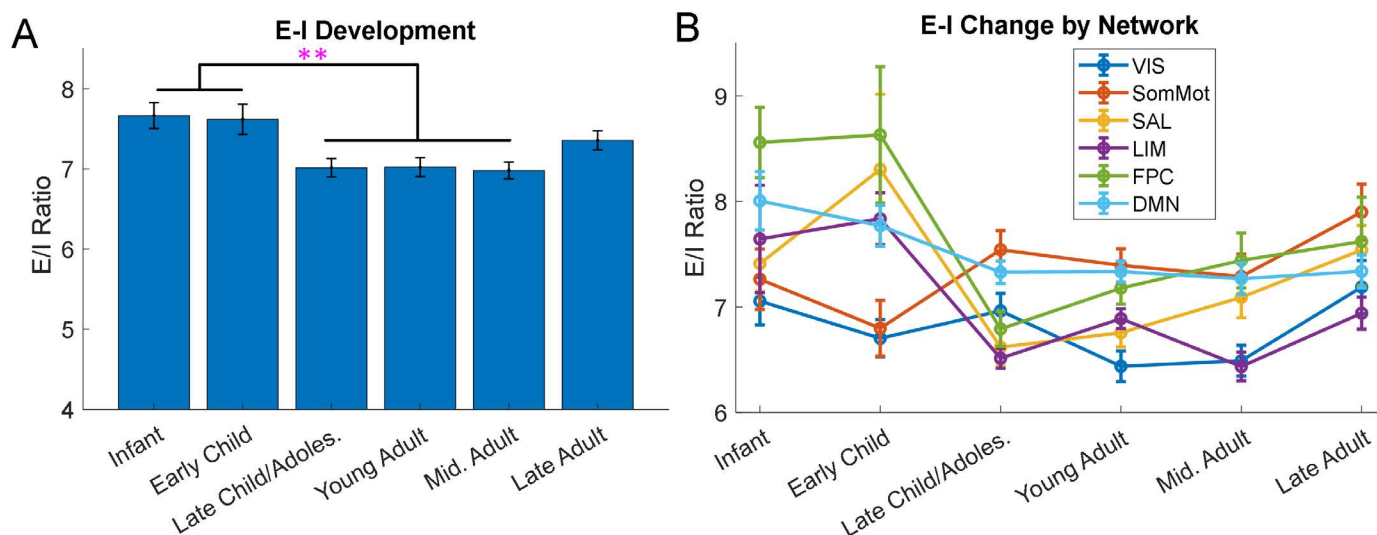
Figure 1. Evolution of E-I balance. (A) Change in E-I ratio over different developmental phases. **(B)** Change in E-I ratio by network over different developmental phases. Double stars indicate significant difference between groups. Infant: 0-1 years; Early child: 2-5 years; Late child/Adolescence: 5-21 years; Young Adult: 22-35 years; Middle Adult: 36-59 years; Late Adult: 60-100 years. VIS: Visual network; SomMot: Somatomotor network; SAL: Salience network; LIM: Limbic network; FPC: Frontoparietal control network; DMN: Default mode network.

Results: We found that the overall E-I balance decreased significantly from infancy/early childhood to late childhood/adolescence ($p < 0.05$, FDR corrected; Fig. 1) and remained relatively stable till middle adulthood followed by a substantial increase in late adulthood ($p < 0.05$, uncorrected). The E-I balance trajectory can be explained well by a quadratic polynomial with the lowest E-I ratio at around 19 years. At the network level, we observed that higher-order networks (e.g., frontoparietal control) started at relatively high E-I balance and displayed more pronounced "U" shape development curves than lower-order networks (visual and somatomotor).

Conclusion: Our study suggests that as the GABAergic system matures, the E-I balance decreases from infancy to adolescence, whereas the natural decline of GABAergic neurotransmission leads to increase of E-I

balance towards late adulthood.

Clinical Relevance: Our study provides an important framework for both standardized assessment of individual growth and early detection of diseases.

Statement Regarding Human Subjects: Our study qualifies for waivers since existing data was used for development and testing of the methodologies.

Statement Regarding Conflicts of Interest: The authors have no conflicts to disclose.

_____

Abstract # -14 Dual Source Computed Tomography & Angiography Disparities In Georgia

Olivia Little, BS[1]; Niayesh Cortese, MD[2]; Martin Halicek, MD, PhD[2]; Weibo Fu[2]; Shaen Deimling[2]; Michael Winkler, MD[3]; Neal Weintraub, MD[2]; Aram Shumavon[4]; Renee Page, MD[2]; Kim Thompson, MD[2]

[1]Mercer University School of Medicine, Savannah, Georgia. [2]Medical College of Georgia at Augusta University, Augusta, Georgia. [3]UNC School of Medicine, Chapel Hill, North Carolina. [4]University of Chicago, Chicago, Illinois

Technology that performs state-of-the-art advanced imaging requires high initial capital expenditure. Areas of the country which may have the highest demand for such technology oftentimes lack the resources to meet such a demand. In Georgia, the Maternal Mortality Rate (MMR) continues to grow and consistently ranks as one of the highest in the nation. Dual source computed tomography (DSCT) is superior to conventional CT for the diagnosis of acute chest pain as it provides superior radiation hygiene and temporal resolution. This technical superiority is particularly important for peripartum women, who experience physiologically elevated heart rates and heightened radiosensitivity.

Ultimately, healthcare systems seeking to address unmet community needs for advanced imaging must seek outside funding, which may take the form of government earmarks, grants from philanthropic foundations, or large gifts.

While data on health disparities is available from the Institute for Health Metrics and Evaluation Global Health Data Exchange (GDHx) to support funding requests and grant applications, geographic data on existing imaging equipment is not available from a single source.

DSCT scanners' location, model, and age was collected from and cross referenced with vendor and healthcare market research firms. Hospitals and imaging centers not included in these databases were contacted by phone. DSCT scanners' locations were used to create a visual representation of their presence within the state. Georgia's MMR data for each county was accessed via the GDHx. Statistical analysis was performed.

Geographical access to DSCT scanners varies significantly across the state. Rural counties with the top 10% MMR have a longer distance to a DSCT (P=0.0006) and results reached significance when analyzed by Wilcoxon's rank sum test (P=0.00094). Counties with the top 25% MMR compared to the counties with the bottom 75% MMR have a longer distance to DSCT scanners (P=0.041). Counties with top 50% MMR have

a longer distance to a DSCT scanner compared to the counties with the bottom 50% of MMR (p=0.0003)

Using a combination of public and industry resources, in addition to our own surveys, we created a database identifying specific DSCT and CT imaging locations. From our data we generated a figure depicting geographic deficits further elucidating regions where installation of additional scanners would maximally benefit public health outcomes.

Images
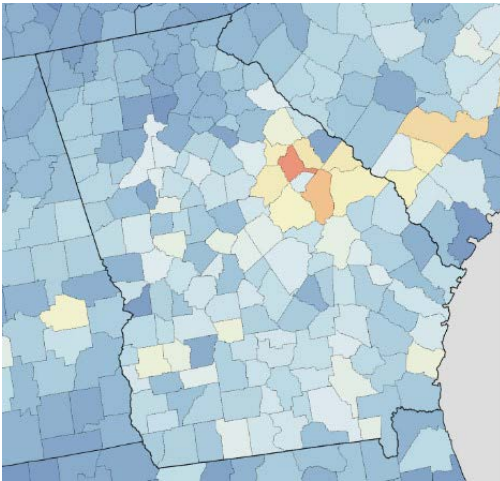
Statement Regarding Human Subjects: We did not use any human subjects in our research.

Statement Regarding Conflicts of Interest: The authors have no conflicts to disclose.

_____

Abstract # - 15 Understanding clinical progression of late-life depression to Alzheimer's disease over 5 years with structural MRI

Lintao Zhang, PhD[1,2]; Mingxia Liu, PhD[1]

[1]Department of Radiology and Biomedical Research Imaging Center, University of North Carolina at Chapel Hill, Chapel Hill, NC. [2]Linyi University, Linyi, Shandong

Background: Previous studies have shown that late-life depression (LLD) may be a precursor of neuro-degenerative diseases and may increase the risk of dementia. At present, the pathological relationship between LLD and dementia, in particularly Alzheimer's disease (AD) is unclear. Structural MRI (sMRI) can provide objective biomarkers for the computer aided diagnosis of LLD and AD, providing a promising solution to understand the clinical progression of brain disorders. But few studies have focused on sMRI based predictive analysis of clinical progression from LLD to AD.

Materials and Methods: We develop a deep learning method to predict the clinical progression of LLD to AD up to 5 years after baseline time using T1-weighted structural MRIs. We also analyze several important factors that limit the diagnostic performance of learning-based methods,including data imbalance, small-

sample-size, and multi-site data heterogeneity, by leveraging a relatively large-scale database to aid model training. To the best of our knowledge, this is among the first attempts to explore the complex pathophysiological relationship between LLD and AD based on structural MRI using a deep learning method. Results: Experimental results on 308 subjects with sMRIs acquired from 2 imaging sites and the publicly available ADNI database demonstrate the potential of deep learning in predicting the clinical progression of LLD to AD.

Conclusion: We investigated the cognitive progression of LLD for the first time with deep learning and machine learning methods based on T1-weighted MRI. Experimental results on 308 subjects with sMRIs acquired from two imaging sites suggested that the potential of learning based methods in automated prediction of LLD progression to AD. We further analyzed and discussed the factors that limit the deep learning classifier in the experiments.

Clinical Relevance: Our method try to predict individuals who progressed to AD within 5 years using baseline T1-weighted MRI. Several important factors that might limit the prediction performance of our method are analyzed by leveraging a relatively large-scale database to aid model training. Our method can help understanding clinical progression of late-life depression to Alzheimer's disease and diagnosis the potential of LDD progressing to AD.

Statement Regarding Conflicts of Interest: All authors have no conflicts to disclose.

_____

Abstract # - 16 DAT: A domain adaptation toolbox for neuroimaging analysis

Hao Guan[1], Mingxia Liu[2]
[1]Department of Radiology, UNC at Chapel Hill, Chapel Hill, NC. [2]Department of Radiology and BRIC, UNC at Chapel Hill, Chapel Hill, NC

Background: Domain adaptation (DA) is an important component of modern machine learning-based medical image analysis which aims at reducing distribution differences between different medical imaging sets. To this end, we have developed the domain Adaptation Toolbox for Medical imaging (DAT) - an open-source software package that is designed for fast facilitation and ease customization of domain adaptation methods for medical image analysis. The DAT toolbox is implemented in MATLAB, and it consists of a collection of popular adaptation algorithms that have been extensively applied in the medical image and machine learning community. Both feature-level and image-level adaptation methods have been integrated into our toolbox. The motivation of the DAT toolbox is to help researchers to facilitate fast configuration, test, visualization, and comparison of different domain methods for medical image analysis.

Materials and Methods: We evaluate different domain adaptation methods on five different datasets. 1) Synthetic datasets; 2) ADNI (with ROI features of structural brain MRIs); 3) fMRI on REST-meta-MDD-Node (Topology feature); 4) fMRI on ABIDE (Topology feature); 5) ABCD (structural MRIs, phantom data). For feature-level adaptation, we use the following evaluation metrics. 1) Direct measure (e.g., distribution difference); 2) Visualization (e.g., t-SNE); 3) Domain-level classification (logistic regression); 4) Indirect measure (category classification).

For image-level adaptation, we use the following evaluation metrics. 1) Peak Signal -Noise Ratio (PSNR); 2)

Correlation Coefficient (CC); 3) Mean Square Error (MSE); 4) Image Visualization (visual inspection).

Results: Overall the domain adaptation can reduce the distribution differences between different medical imaging sites and achieve better performance in terms of those evaluation metrics. In different scenarios, the performance of different adaptation methods may vary.

Conclusion: We develop a toolbox for domain adaptation/data harmonization of different medical imaging sites. The experiment on several benchmark datasets demonstrates its effectiveness, simplicity, and flexibility.

Clinical Relevance: The toolbox can help reduce data heterogeneity among different sites. This is helpful for building larger sites for medical image analysis or make the analysis consistent across sites.

Images
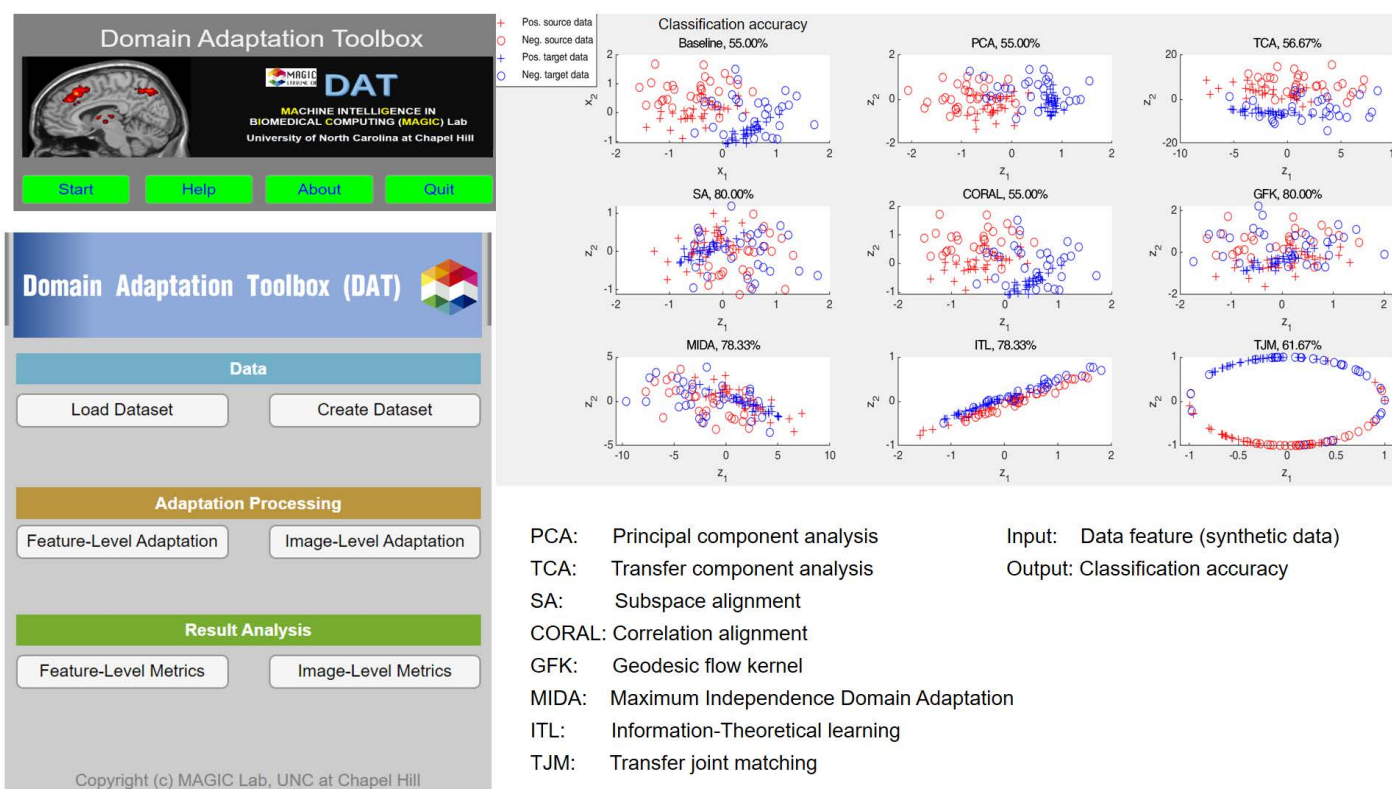
PCA: Principal component analysis
TCA: Transfer component analysis
SA: Subspace alignment
CORAL: Correlation alignment
GFK: Geodesic flow kernel
MIDA: Maximum Independence Domain Adaptation
ITL: Information-Theoretical learning
TJM: Transfer joint matching

Input: Data feature (synthetic data)
Output: Classification accuracy

Statement Regarding Conflicts of Interest: The authors have no conflicts to disclose.

_____

Abstract # - 18 Neural Flexibility as an effective biomarker to discern Attention-Deficit/Hyperactivity Disorder

Weiyan Yin, PhD[1]; Tengfei Li, PhD[1]; Peter J. Mucha, PhD[2]; Jessica R. Cohen, PhD[1]; Hongtu Zhu, PhD[1]; Ziliang Zhu, MS[1]; Weili Lin, PhD[1]

[1]University of North Carolina at Chapel Hill, Chapel Hill, NC. [2]Dartmouth College, Hanover, NH

Background: ADHD is one of the most prevalent psychiatric disorders in children and is often accompanied by deficits in executive function. Recent studies have demonstrated the links between MR-derived neural flexibility and executive function. In this study, we hypothesized that neural flexibility could discern children with ADHD from typically developing children (TDC).

Materials and Methods: We used publicly available data from the ADHD-200 dataset. 67 medication naïve children with ADHD (PKU/NYU: 51/16) and 96 TDC (PKU/NYU: 65/31) were included in this study. RsfMRI data were preprocessed using a well-established pipeline. The mean time series of each ROI was extracted using the Power264 template. A sliding window approach was employed (window width = 30 volumes and increment = 1 volume) and Pearson's correlations were calculated for each pair of ROIs. Dynamic module assignments were detected using the GenLouvain method and neural flexibility of each ROI was calculated. The XGBoost algorithm with nodal neural flexibility as the input was applied to train a model to discern ADHD subjects from TDC. 10-fold cross validation was performed and repeated 10 times using the PKU data. The optimal combination of brain regions was detected. Specifically, we evaluated the performance of top N (1-264) regions based on their importance scores from 10-times 10-fold cross validations and determined a set of brain regions that yielded the optimal performance. Finally, the PKU-trained model was applied to the NYU data as an independent test.

Results: The model was 54.98% accurate in discerning ADHD from TDC within the PKU dataset when using neural flexibility of all 264 regions (sensitivity = 42.43%, specificity = 64.66%, AUC = 56.46%). Accuracy increased markedly (77.2%) when including neural flexibility only of core regions (Fig. 1b; sensitivity = 72.13%, specificity = 80.78%, AUC = 84.32%). When we applied the PKU trained model to the NYU dataset, an accuracy of 74.46% was achieved (sensitivity = 62.5%, specificity = 80.64%, AUC = 67.94%), demonstrating the robustness of the proposed approach.

Conclusion: MR-derived neural flexibility could serve as an effective biomarker to discern children with ADHD from TDC.

Clinical Relevance: Early detection of ADHD could provide an opportunity for intervention to minimize its long-term consequences. We demonstrate the potential of using neural flexibility to identify children with ADHD.

Images
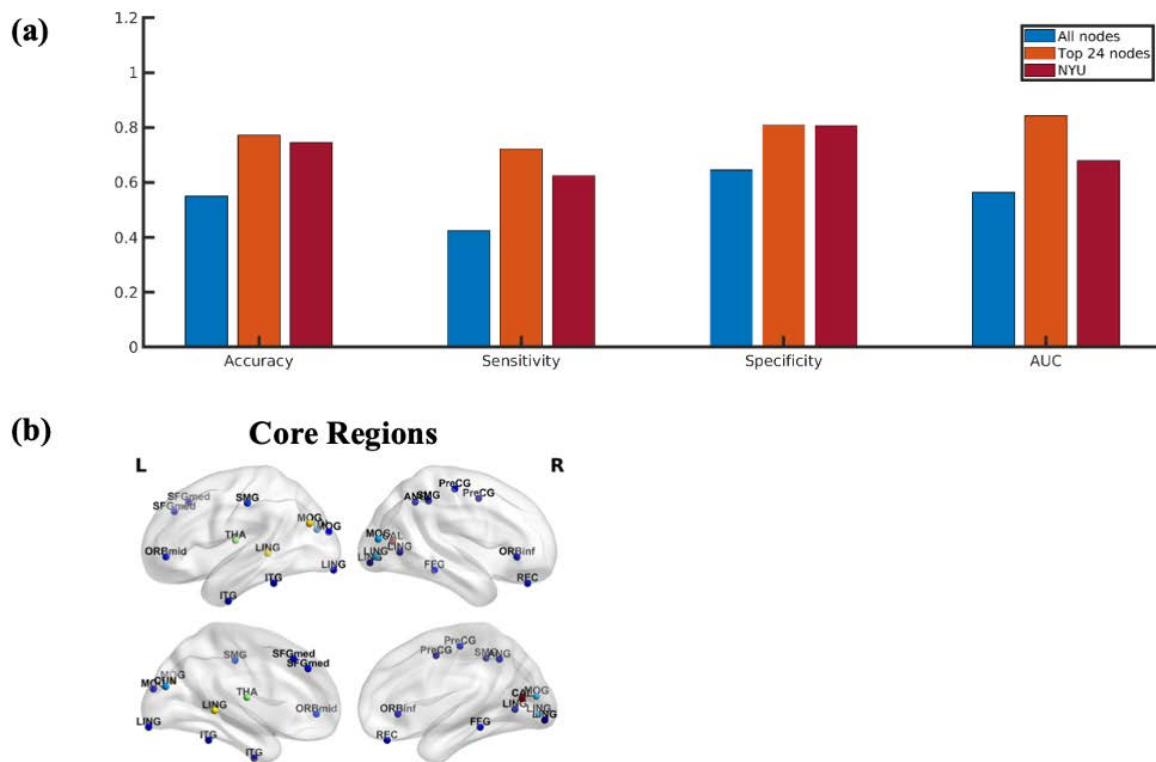
Figure 1. (a) The accuracy, sensitivity and specificity when including all 264 ROIs, the top 24 ROIs, and independent testing using the NYU dataset, respectively. (b) The spatial distribution of the top 24 regions for the ADHD classification model.

Statement Regarding Human Subjects: We used a publicly available ADHD-200 dataset. Written informed consent was obtained by local institutions.

Statement Regarding Conflicts of Interest: The authors declare that they have no conflict of interest.

_____

Abstract # - 19 Superfast Spherical Mapping of Cortical Surface Meshes using Deep Unsupervised Learning

Fenqiang Zhao, PhD; Zhengwang Wu, PhD; Li Wang, PhD; Weili Lin, PhD; Gang Li, PhD

Department of Radiology and Biomedical Research Imaging Center, University of North Carolina, Chapel Hill, NC

Background: In neuroimaging studies, cortical surface-based analysis is known to have special advantages over volumetric analysis of the cerebral cortex. Fig. 1 (a) shows a typical surface-based analysis. As a key step, spherical mapping uses the spherical topology of the cortex to map the surface onto a sphere with minimum distortion, thus providing a simpler space for visualizing and analyzing the folded cortex more conveniently and precisely. Therefore, it has been widely adopted in neuroimaging analysis pipelines, e.g., FreeSurfer, and iBEAT v2.0.

Materials and Methods: We propose an unsupervised learning-based spherical mapping algorithm, Superfast Spherical Surface Mapping (S3Map), to learn the metric-preserving mapping between the original and spherical surface meshes. As shown in Fig. 1(b), S3Map uses Spherical U-Net model to learn the deformation field for minimizing the distortions between the icosahedron-remeshed original and spherical surface meshes. The end-to-end unsupervised learning network requires no ground truth and is very flexible to combine various distortion measures.

We have extensively validated S3Map on three large-scale neuroimage datasets including 867 neonates (25-45 postmenstrual weeks) from the Developing Human Connectome Project, 220 infants (0-6 years) from Baby Connectome Project, and 830 adults (55-90 years) from Alzheimer's Disease Neuroimaging Initiative dataset. The cortical surfaces are reconstructed using dHCP pipeline, iBEAT V2.0 and FreeSurfer, respectively. All inner cortical surfaces are fairly mapped onto the sphere using different methods.

Results: Our S3Map outperforms the state-of-the-art FreeSurfer by an average of 0.28%, 2.74%, 1.6% in metric, area, and angle distortions, respectively. This indicates our method finds a more optimal solution than FreeSurfer to the spherical mapping problem by learning effective representations at high levels of abstraction. Moreover, it runs extremely faster than FreeSurfer, taking only several seconds to process a cortical surface, while FreeSurfer needs 20 minutes, which hinders the big neuroimaging data analysis.

Conclusion: Our method produces more isometric mapping than the state-of-the-art FreeSurfer, and speeds up the process by 200+ times, solving the critical problem of slow computation in this field.

Clinical Relevance: Our S3Map makes large-scale neuroimaging data analysis and real-time clinical data processing more convenient and promising.

Images

(a) Typical computational pipeline of cortical surface-based analysis

Brain MR image   Tissue segmentation   Hemisphere separation   Topology correction

Cortical surface reconstruction   Surface inflation   **Spherical mapping**   Cortical surface registration   Cortical surface parcellation

Surface atlas
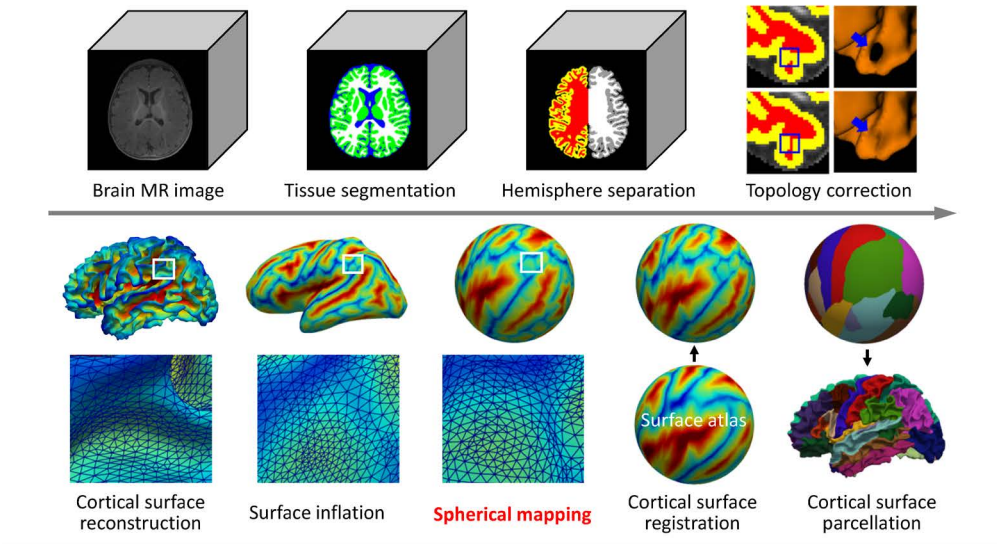
(b) Our spherical mapping method

Step 1
Initial spherical mesh generation

Original surface and its mesh

sulcal fundus
Average convexity
gyral crown

Inflated surface

Initial spherical surface and its mesh

remesh

Icosahedron-reparameterized original mesh

Icosahedron-reparameterized spherical mesh

Distortion J $\min_{\phi} J$

Distortion J $\min_{\phi} J$

Step 2
Distortion correction of spherical mesh

Original surface's metric properties

larger
smaller

Distance (N_vx6)   Area (N_vx6)   Angle (N_vx6)

Spherical U-Net

Scaling and squaring layers

Velocity field ($\vec{u}$)   Deformation field (ϕ)

Spherical transform

Reparameterization again on next resolution

Distortion loss J

Spherical surface's metric properties

Moved spherical mesh

(c) Spherical mapping results of a surface obtained by different methods
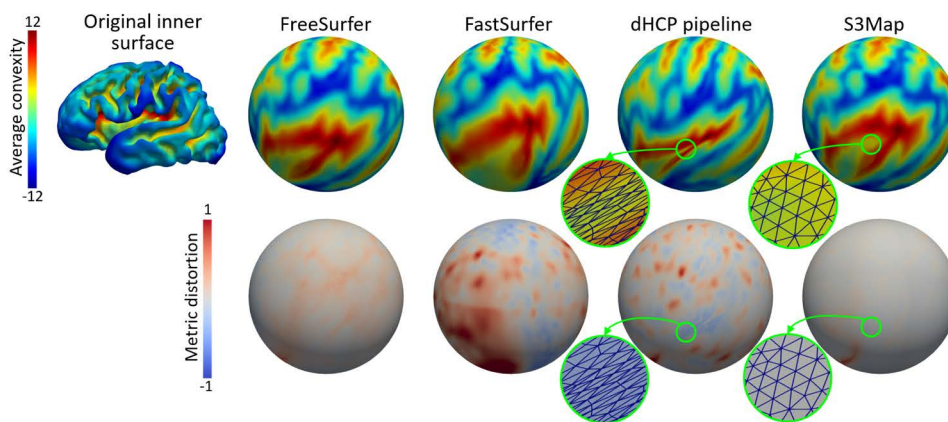
12
Average convexity
-12

Original inner surface   FreeSurfer   FastSurfer   dHCP pipeline   S3Map

1
Metric distortion
-1

Abstract # - 21 Longitudinal development of regional cerebellar volumes during the first 800 days

Ya Wang, MD; Liangjun Chen, PhD; Zhengwang Wu, PhD; Tengfei Li; Yue Sun; Jiale Cheng; Hongtu Zhu; Weili Lin; Li Wang, Gang Li

University of North Carolina, Chapel, NC

Background: The cerebellum plays a key role in many functions beside somatomotor control. The functional activations have been found in different lobules during different cognitive and motor tasks. However, due to the limited availability of longitudinal infant MR images and image processing methods, few studies have characterized regional cerebellar development at early ages, during which the cerebellum undergoes dramatic and nonlinear changes. This study aims to fill this critical gap by exploring the volumetric developmental trajectories of 20 cerebellar compartments within the first 800 days of age.

Materials and Methods: 511 longitudinal structural MRI scans (T1- and T2-weighted images) from 235 normal, term born subjects during the first 800 days were included, which were collected by the UNC/UMN Baby Connectome Project. We first preprocessed the MR images and extracted the cerebellum using the iBEAT V2.0. Then we leveraged a semi-supervised transfer learning method dedicated to infant cerebellum tissue segmentation and the SUIT cerebellum parcellation protocol, which divides each cerebellar hemisphere into 10 subregions. The generalized additive mixed model was employed to fit the population-level volumetric trajectories of each lobule. The gender difference of the fitted population-level volumetric patterns of each lobule were also investigated.

Results: The volumetric developmental trajectory of each subject and the population-level curves by gender are depicted for the lobular volumes in both hemispheres (Fig. 1). Each lobule in both hemispheres exhibits rapid volume increase within the first postnatal year and then relatively slow increase thereafter. Several lobules exhibit longer age ranges of rapid volumetric increase. However, X lobules in both hemispheres shift to a sluggish increase only around 200 days after birth, which are the earliest among all lobules. Besides, the developmental trajectory of each lobule exhibits a larger absolute volume in males than females emerging from different ages ($p < 0.05$).

Conclusion: The early volumetric development of the cerebellar lobules reveals lobule-specific nonlinear growth patterns with rapid increases at first followed by relative sluggish growth thereafter and is sexually dimorphic starting from different ages.

Clinical Relevance: The normative volumetric development of cerebellar lobules is an important reference for understanding abnormal cerebellar development in brain disorders.

Images
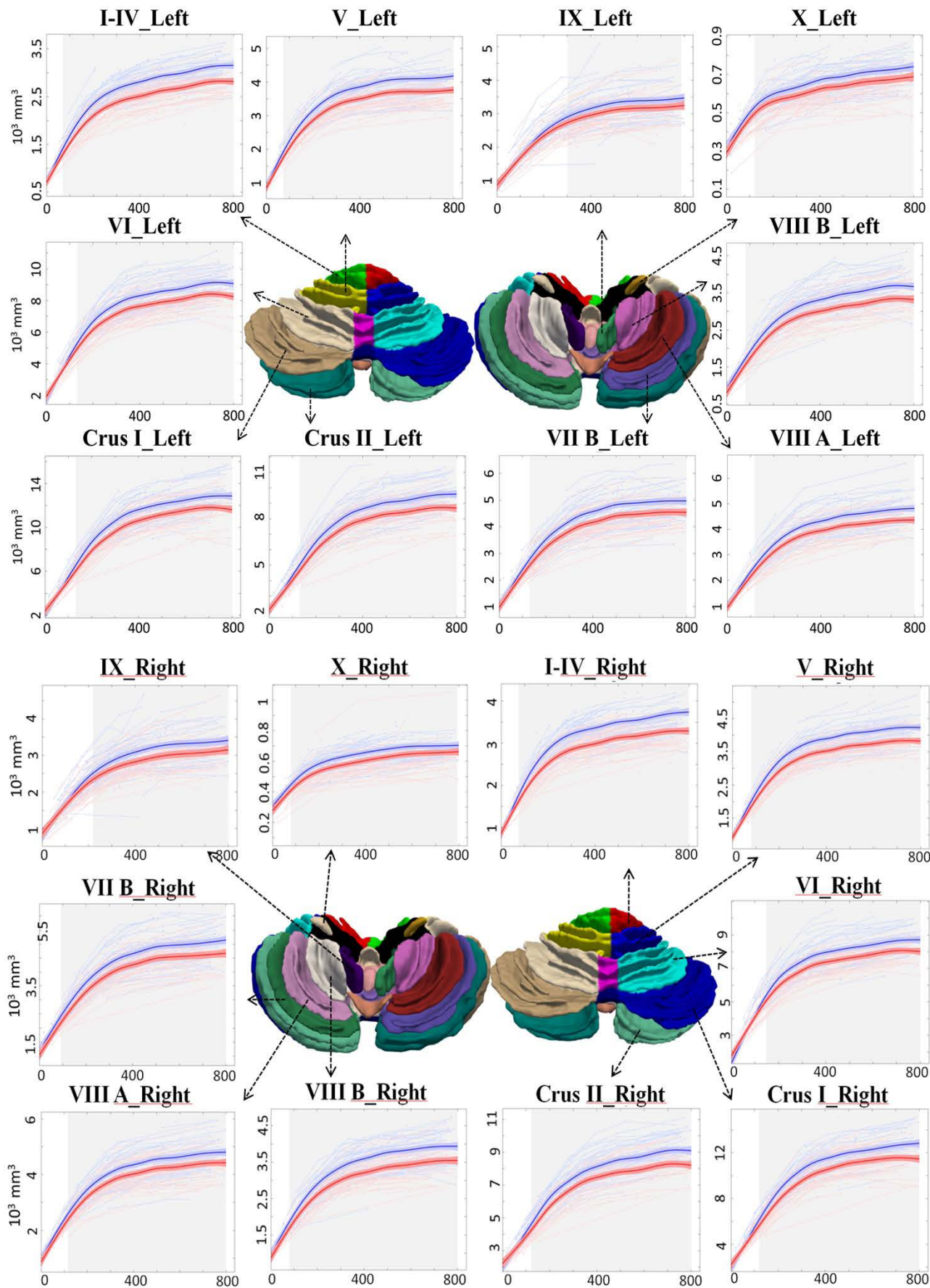
Statement Regarding Human Subjects: All the datasets used in this research are publicly available.

Statement Regarding Conflicts of Interest: The authors have no conflicts to disclose.

_____

Abstract # - 22 Neural network on cortical surfaces for prediction of infant cognitive scores

Jiale Cheng[1], Fenqiang Zhao[1], Zhengwang Wu[1], Xinrui Yuan[1], Li Wang[1], Weili Lin[1], John H Gilmore[1], Xin Zhang[2], Gang Li[1]

[1]University of North Carolina at Chapel Hill, Chapel Hill, North Carolina. [2]South China University of Technology, Guangzhou, Guangdong, China

Background: Extensive population-based studies have revealed a tight connection between brain morphology and cognitive skills. Understanding this intrinsic relationship during infancy is of immense importance as it may help improve the health and well-being of children. In this study, we intended to develop an advanced deep learning-based method to predict each individual infant's cognitive scores based on brain cortical feature maps derived from MR images.

Material and Methods: Brain structural MR images from 110 healthy infants were used and processed by an infant-tailored computational pipeline iBEAT V2.0 to reconstruct cortical surfaces and compute four morphological features of each surface vertex, i.e., cortical thickness, sulcal depth, average convexity, and mean curvature. To quantify the cognitive functioning development level of each participant, five Mullen Scales of Early Learning were measured at their 2 years of age.

Leveraging the intrinsic spherical topology of cortical surfaces, we proposed to partition the cortical surfaces into uniform patches. By applying the innovative Transformer layer, our neural network (Spherical Transformer) can effectively and efficiently extract the fine-grained contextual information within surface patches through computing the pairwise vertices' features correspondence. Together with the down-sampling layers, a hierarchical representation was generated by gradually merging neighboring surface vertices in deeper network layers and further output the predicted cognitive scores, as shown in Fig. 1A.

Results: We adopted the five-fold cross-validation strategy. Our proposed method obtained an average root mean squared error of 0.157±0.025 for the five cognitive scales, which is significantly better than two widely adopted methods, i.e., SUNet (0.163±0.025) and UGSCNN (0.165±0.028) with p-value < 0.05, as shown in Fig. 1B.

Conclusion: A spherical transformer-based neural network has been proposed in this study to predict the infant cognitive scores based on cortical surface feature maps. It differs from the previous methods with its content-based feature aggregation function, which can more effectively model long-range dependency. Promising results were obtained by testing on 110 infants.

Clinical Relevance: This study preliminarily validated the existence of predictable intrinsic relationship between infant brain morphology and cognitive skills.

Images

Fig. 1A. Illustrations of (a) the backbone, (b) the Spherical Transformer block. The detailed structure of Spherical Transformer layer is illustrated in (c). V and N_i denotes the number of vertices in the surface patch and the i-th spherical subdivision respectively, while C^l denotes the number of channels at the l-th layer.

(a)

(c)

(b)
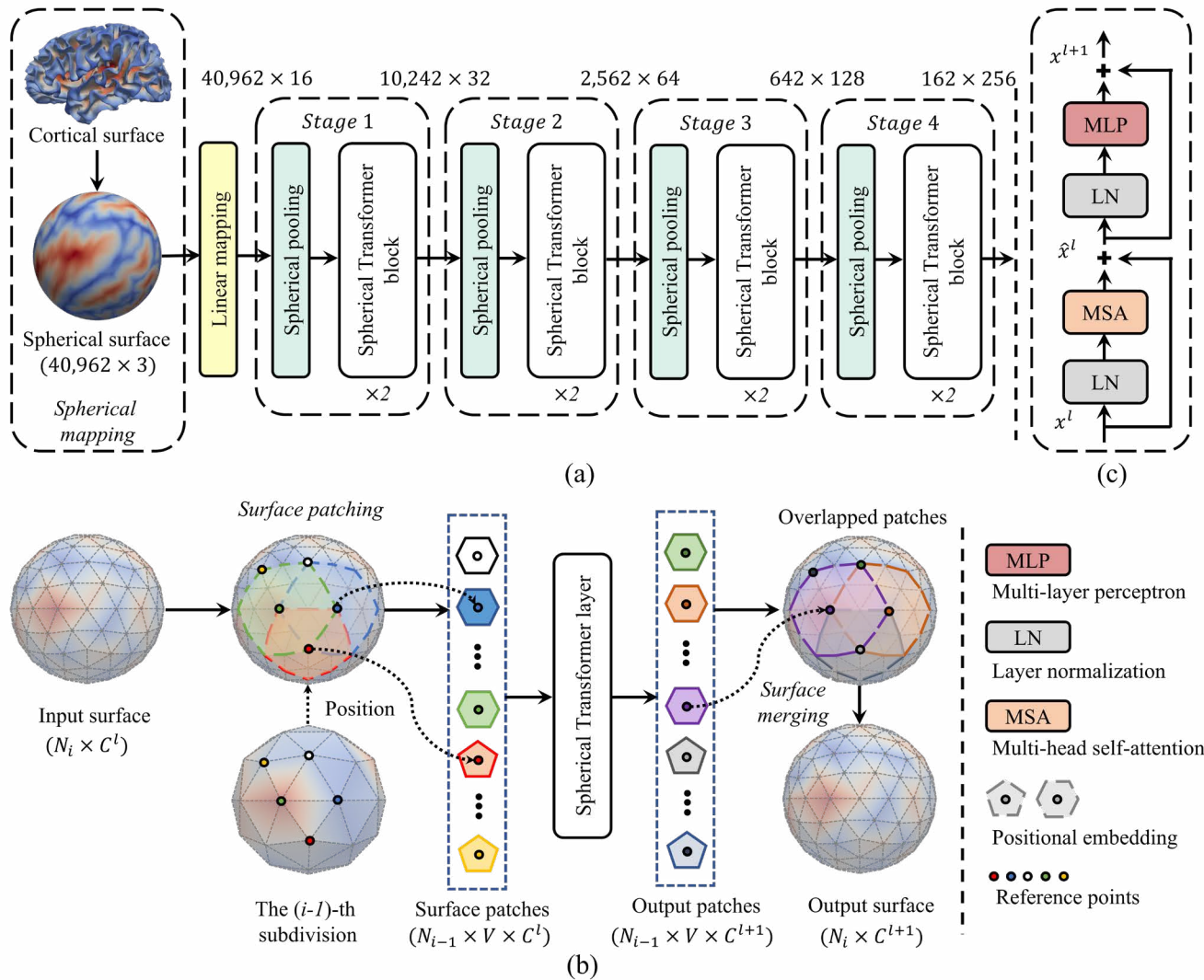
Fig. 1B. Comparison of different network architectures for predicting five cognitive scales, i.e., Visual Receptive Scale (VRS), Fine Motor Scale (FMS), Receptive Language Scale (RLS), Expressive Language Scale (ELS), and Early Learning Composite Scale (ELC), at 2 years of age using cortical surface data at birth by root mean square error. * indicates significantly better results than other methods with p-value<0.05 by paired t-test.

Methods	VRS	FMS	RLS	ELS	ELC	Average
UGSCNN [31]	0.20 ± 0.02	0.15 ± 0.04	0.15 ± 0.03	0.15 ± 0.04	0.17 ± 0.04	0.165 ± 0.028
SUNet [40]	0.19 ± 0.02	0.14 ± 0.04	0.16 ± 0.03	0.16 ± 0.04	0.17 ± 0.04	0.163 ± 0.025
Proposed	$\mathbf{0.18 \pm 0.02^*}$	$\mathbf{0.12 \pm 0.04^*}$	$\mathbf{0.15 \pm 0.03}$	$\mathbf{0.15 \pm 0.04}$	$\mathbf{0.16 \pm 0.04}$	$\mathbf{0.157 \pm 0.025^*}$

Statement Regarding Human Subjects: All the datasets used in this research are publicly available.

Statement Regarding Conflicts of Interest: The authors have no conflicts to disclose.

Abstract # - 24 A Longitudinally-consistent Deep Framework for Joint Subcortical Segmentation and Registration of Infant Brains

Liangjun Chen, Zhengwang Wu, Fenqiang Zhao, Ya Wang, Weili Lin, Li Wang, Gang Li

University of North Carolina, Chapel Hill, NC

Background: Subcortical segmentation and registration are critical in studying early subcortical development and related neurodevelopmental disorders. However, these two closely related tasks are conventionally performed independently, ignoring their reciprocity and mutual benefits and leading to low accuracy in the infant brain MR images typically exhibiting dynamic imaging appearance and low contrast. Besides, existing subcortical segmentation methods are typically cross-sectionally trained, thus frequently leading to temporally inconsistent results in longitudinal studies.

Materials and Methods: We develop a coarse-to-fine framework (Fig. (A)) to jointly conduct both affine and deformable registrations and subcortical segmentation of longitudinal scans. In the coarse stage, the registration and segmentation branches share one encoding part, allowing them to assist each other to capture more generalized features and resulting in improved accuracy in both tasks. Moreover, we jointly input multiple longitudinal scans from each subject in training to learn the within-subject anatomical correspondences as longitudinal guidance to ensure longitudinal consistency. Besides, we incorporate the signed distance maps as spatial contextual guidance into the fine-stage network to refine segmentation and registration results.

239 T1w and T2w MRI scans (high resolution: 0.8x0.8x0.8 mm3) from 64 normative infant subjects (with at least three longitudinal scans) covering the age range from 6 to 26 months from the UNC/UMN Baby Connectome Project (BCP) were leveraged in this study.

Results: We quantitatively compared our methods to six SOTA methods. As shown in Fig. 1 (B), our method consistently maintained advantageous performance on both segmentation and registration tasks on all subcortical structures. As shown in Fig. 1 (C), compared to SOTA cross-sectionally trained segmentation method, our method leads to smoother and monotonically increased growth patterns of the amygdala, suggesting its superior longitudinal consistency.

Conclusion: We propose a coarse-to-fine deep learning framework to jointly perform infant subcortical segmentation and registration to encourage longitudinal consistency and achieve high segmentation and registration accuracy.

Clinical Relevance: Our method achieved longitudinally consistent segmentations on subcortical structures, making it helpful for precise and consistent charting development of small subcortical structures during infancy.
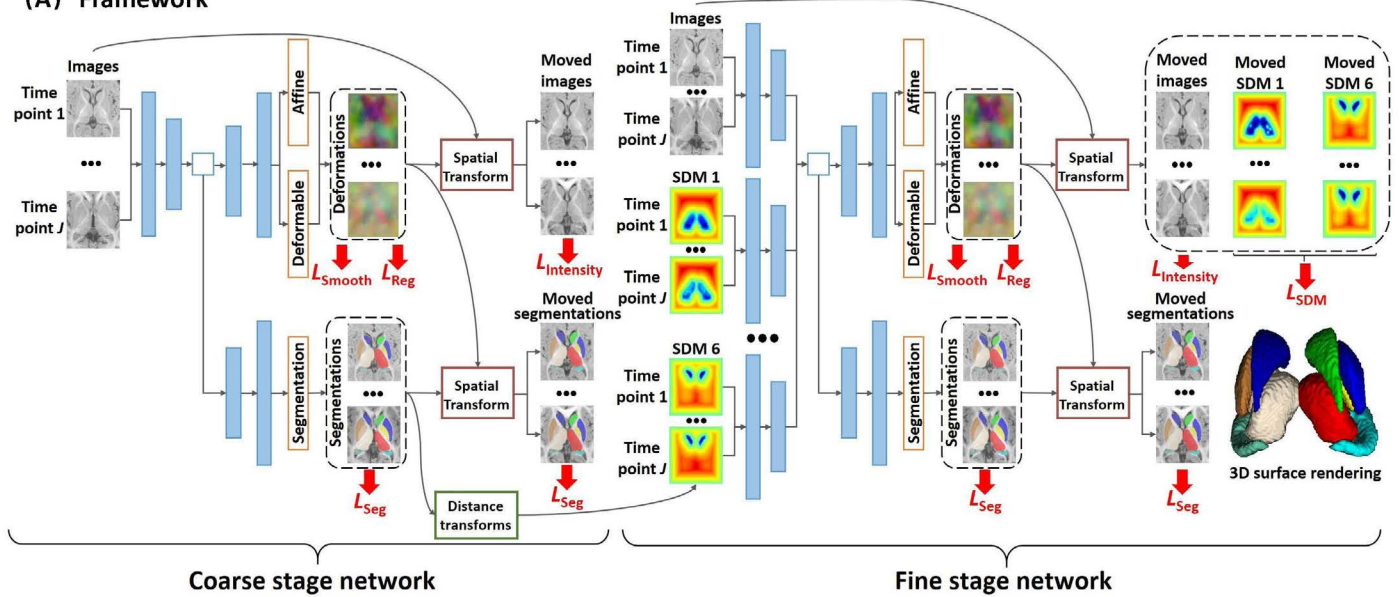
Images

(A) Framework

Table 1. Segmentation accuracy (DSC) on 12 subcortical structures. *indicate statistically significant improvements with $p-value < 0.05$, compared to competing methods.

DSC (%)	FIRST	V-net	IFSubSeg	U-ReSNet	Proposed (CSNet)	Proposed (w/o L_{SDM})	Proposed
Thalamus_L	87.6 ± 2.5	90.1 ± 2.4	96.4 ± 1.3	92.5 ± 2.2	94.7 ± 1.6	95.7 ± 0.9	**96.4 ± 0.7**
Caudate_L	86.4 ± 2.3	88.2 ± 3.0	94.7 ± 1.5	91.4 ± 2.6	93.0 ± 0.9	94.9 ± 1.6	**95.1 ± 1.4**
Putamen_L	81.3 ± 4.6	87.2 ± 2.7	94.7 ± 1.6	92.4 ± 2.0	93.7 ± 1.6	94.8 ± 1.3	**95.3 ± 1.0**
Pallidum_L	81.2 ± 5.5	87.6 ± 3.7	94.0 ± 1.4	92.4 ± 1.9	92.9 ± 1.9	94.1 ± 2.1	**94.7 ± 1.2***
Hippocampus_L	76.3 ± 7.4	80.4 ± 5.5	91.4 ± 1.6	87.2 ± 5.5	89.7 ± 5.9	91.7 ± 2.5	**92.2 ± 2.2***
Amygdala_L	48.8 ± 16.0	73.7 ± 6.9	87.8 ± 2.9	86.8 ± 7.0	87.9 ± 7.9	88.5 ± 2.6	**89.8 ± 3.3***
Thalamus_R	86.8 ± 3.3	89.5 ± 2.7	96.2 ± 1.0	92.6 ± 2.6	94.2 ± 1.8	96.0 ± 3.2	**96.6 ± 2.2**
Caudate_R	87.9 ± 3.0	88.8 ± 2.5	94.8 ± 1.4	91.3 ± 2.8	92.9 ± 1.0	94.2 ± 2.5	**95.0 ± 2.2**
Putamen_R	83.5 ± 3.7	87.0 ± 2.8	94.3 ± 1.2	91.4 ± 1.9	92.6 ± 2.7	94.5 ± 3.9	**94.9 ± 0.7**
Pallidum_R	84.5 ± 4.3	84.9 ± 5.5	93.0 ± 1.5	89.9 ± 3.0	92.1 ± 3.1	93.1 ± 3.7	**93.8 ± 3.5***
Hippocampus_R	78.9 ± 8.5	80.9 ± 7.5	90.5 ± 2.2	86.1 ± 6.2	88.7 ± 8.3	90.7 ± 2.1	**91.2 ± 2.0***
Amygdala_R	56.4 ± 14.1	73.2 ± 8.3	88.4 ± 2.3	86.9 ± 7.1	87.4 ± 4.3	88.8 ± 2.9	**89.6 ± 2.3***

Table 2. Registration accuracy (DSC) on 12 subcortical structures. *indicate statistically significant improvements with $p-value < 0.05$, compared to competing methods.

DSC (%)	ANTS	Voxelmorph	U-ReSNet	Proposed (CSNet)	Proposed (w/o L_{SDM})	Proposed
Thalamus_L	87.1 ± 4.1	87.7 ± 5.1	88.2 ± 4.8	88.6 ± 4.4	91.3 ± 3.8	**92.3 ± 4.0***
Caudate_L	87.4 ± 4.7	88.0 ± 3.3	88.6 ± 4.9	89.1 ± 4.7	90.7 ± 4.4	**91.6 ± 3.7***
Putamen_L	87.7 ± 3.7	88.0 ± 4.3	88.3 ± 4.3	88.9 ± 4.9	90.9 ± 4.1	**91.6 ± 4.1***
Pallidum_L	85.8 ± 4.6	86.0 ± 5.9	86.4 ± 4.7	89.1 ± 4.6	91.1 ± 4.0	**92.8 ± 4.1***
Hippocampus_L	84.3 ± 3.7	84.1 ± 5.5	85.0 ± 4.0	85.5 ± 2.1	88.0 ± 4.2	**88.5 ± 4.3***
Amygdala_L	82.7 ± 6.3	82.8 ± 7.0	83.6 ± 6.2	84.3 ± 6.6	86.8 ± 4.7	**88.0 ± 4.5***
Thalamus_R	87.6 ± 2.7	88.1 ± 5.1	89.0 ± 4.3	89.9 ± 4.1	91.2 ± 4.0	**92.8 ± 3.4***
Caudate_R	86.4 ± 3.8	87.2 ± 5.1	88.0 ± 4.2	88.7 ± 4.9	89.9 ± 4.1	**90.4 ± 4.3***
Putamen_R	86.0 ± 4.1	86.7 ± 5.2	87.5 ± 4.9	88.5 ± 4.7	89.7 ± 4.5	**90.8 ± 4.2***
Pallidum_R	85.6 ± 5.8	86.5 ± 5.6	88.0 ± 5.2	88.3 ± 4.3	90.9 ± 4.2	**92.0 ± 4.1***
Hippocampus_R	84.0 ± 4.1	83.7 ± 5.2	84.7 ± 5.1	85.1 ± 4.6	87.9 ± 4.1	**89.4 ± 3.9***
Amygdala_R	81.6 ± 7.1	82.3 ± 7.5	83.5 ± 6.6	84.1 ± 6.1	86.0 ± 4.0	**86.9 ± 4.0***

(B) The segmentation and registration accuracies
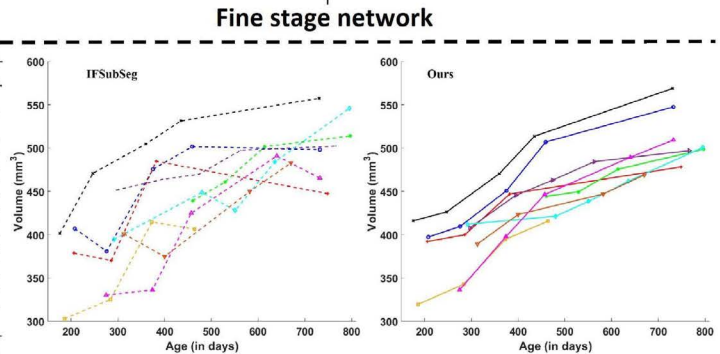
(C) Volume changes of the amygdala

Fig. 1. (A) A schematic illustration of the proposed framework, consisting of a coarse stage network and a fine stage network. **(B)** The segmentation and registration accuracies of our method, compared to competing methods in terms of Dice similarity coefficient (DSC). **(C)** Volume changes of the amygdala from subjects with 4 or more longitudinal scans (in different colors). Ours (solid lines); IFSubSeg (dash lines).

Statement Regarding Human Subjects: All the datasets used in this research are publicly available.

Statement Regarding Conflicts of Interest: The authors have no conflicts to disclose.

Abstract # - 25 Four-dimensional Mapping of Dynamic Subcortical Development of Infant Brains

Liangjun Chen, Ya Wang, Zhengwang Wu, Yue Shan, Tengfei Li, Sheng-Che Hung, Hongtu Zhu, Weili Lin, Li Wang, Gang Li

University of North Carolina, Chapel Hill, NC

Background: The subcortical structures directly control many cognitive outcomes and are closely associated with various brain disorders. It is important to characterize and understand the early normative developmental patterns of the subcortex, which features a complex, dynamic, and regionally-heterogeneous process. However, due to the limited availability of longitudinal data and dedicated image processing methods, few studies focused on the infant subcortex. This study aims to investigate the early developmental patterns of the thalamus, caudate, putamen, pallidum, hippocampus, and amygdala.

Materials and Methods: 513 longitudinal T1w and T2w MRI scans from 231 normative infant subjects within the first two postnatal years from the UNC/UMN Baby Connectome Project (BCP) were leveraged in this study. All MRI scans were processed using iBEAT V2.0. An infant dedicated deep framework was employed for subcortical segmentation. Then we constructed 12 subcortical surfaces based on a 0-month atlas subcortical label from our constructed 4D infant brain atlas and successively warped them to each individual image by using the 4D atlas as the bridge to calculate the surface areal expansion. The generalized additive mixed model was used to fit the population-level developmental trajectories of the total volume and vertex-wise surface area.
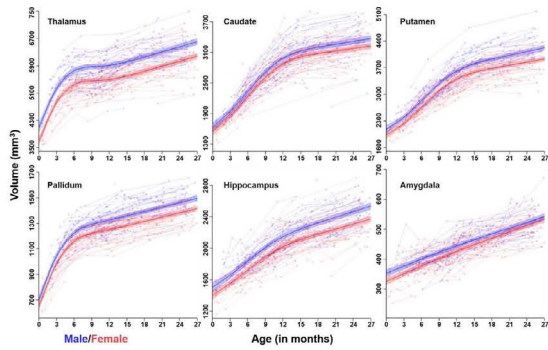
Images

Fig. 1 (A). Longitudinal volumetric developmental trajectories of different subcortical structures. Plots show both the individual-level (thin lines) and fitted population-level (solid curves) developmental trajectories of the bilaterally averaged volumes of thalamus, caudate, putamen, pallidum, hippocampus, and amygdala structures. The shaded ribbon around each curve denotes 95% confidence intervals.

Fig. 1 (B). Statistically significant high-growth and low-growth regions (FDR < 0.05) at different ages for bilateral (a) thalamus and amygdala, (b) caudate and putamen, (c) pallidum and hippocampus. Red colors denote high-growth areas. Blue colors denote low growth areas.

Results: Fig. 1 (A) delineates the volumetric trajectories of each subject's subcortical structures and the fitted population's developmental trajectories. Each subcortical structure (except for the amygdala with an approximately linear increase) exhibits a rapid expansion after birth, then the growth rate decreases starting at different ages. Besides, each subcortical structure exhibits a significantly larger absolute volume in males than females throughout the first two years (p < 0.05). The statistically significant high- and low-growth subregions of each subcortical structure are illustrated in Fig. 1 (B). Some subcortical subregions grow faster during different age ranges. Overall, the surface areal expansion of each subcortical structure exhibits distinct, age-dependent, region-specific, and bilaterally quasisymmetric patterns.

Conclusion: Our study has charted volumetric developmental trajectories and spatiotemporally high- and low-growth subregions of six subcortical structures during infancy.

Clinical Relevance: This study is highly useful for the early diagnosis of various brain disorders associated with the subcortex.

Statement Regarding Human Subjects: All the datasets used in this research are publicly available.

_____

Abstract # - 26 Evaluation of paraspinous muscle signal fat fraction using chemical shift encoded MRI: Comparison with CT attenuation

Clayton W. Commander, MD, PhD; Hyeon Yu, MD, FSIR; Charles T. Burke, MD, FSIR, FACR

University of North Carolina Department of Radiology, Chapel Hill, NC

Background: Correlating measures of quantified intramuscular fat on CT and MRI would allow for more robust studies of sarcopenia. The purpose of this study was to compare the estimated signal fat fraction (FF) of the paraspinous musculature (PSM) using chemical shift encoded MRI with average attenuation of the PSM on CT.

Materials and Methods: A total of 128 adults (60 female, 68 male; mean age, 57.8 ± 15.4 years) who underwent abdominopelvic CT and MRI in 2019 with a maximum of 15 days between the examinations were included. A single slice from both studies at the level of the superior mesenteric artery origin was selected for analysis. PSM was manually segmented and cross-sectional areas were measured on CT and MRI. The intramuscular signal FF was calculated using in-phase and opposed-phase MRI sequences. Average attenuation of the segmented PSM was used as a surrogate for intramuscular fat on CT images. Measures from both CT and MRI were compared. Subgroup analyses were performed for patients who underwent contrast-enhanced CT and non-enhanced CT as well as by gender.
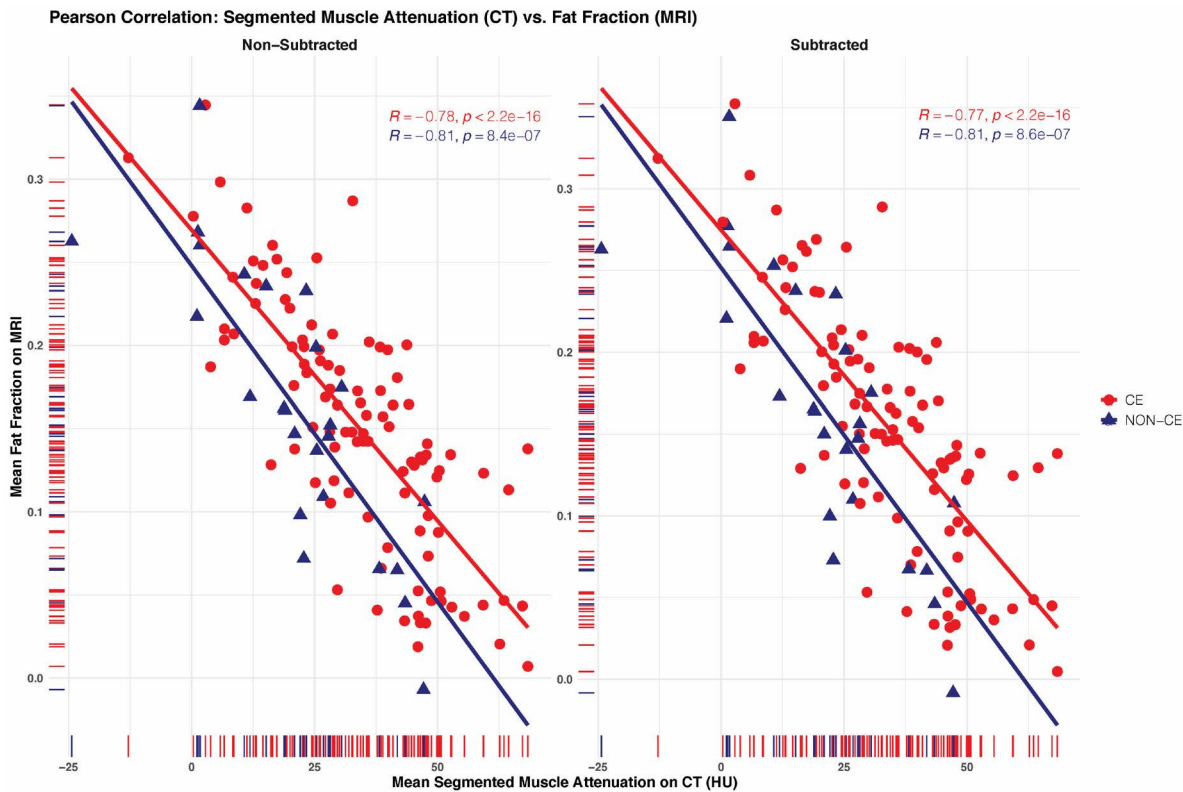
Results: There was no significant difference between the segmented areas on CT and MRI per patient, though male patients have a significantly higher PSM area than females ($p < .001$). While there was a difference in average CT attenuation between males and females ($p < .001$), there was no difference in the MRI fat fraction by gender ($p = .98$). MRI signal FF was strongly correlated with average attenuation on both contrast-enhanced CT ($r = -0.78$, $p < .001$) and non-enhanced CT ($r = -0.81$, $p < .001$). Similar results were found for male and female patients. These findings are robust and resistant to background noise and varying signal-to-noise ratios.

Conclusions: CT and chemical shift encoded MRI sequences can be used nearly interchangeably to quantify myosteatosis, an important imaging biomarker.

Clinical Relevance:
1. Segmented cross-sectional areas of the paraspinal musculature on CT and MRI are not significantly different.
2. MRI signal fat fraction of the paraspinal musculature correlates strongly with average attenuation of the paraspinal musculature on both contrast-enhanced and non-enhanced CT.
3. MRI signal fat fraction of the paraspinal musculature calculated using two-point chemical shift encoded sequences is robust and resistant to background noise and varying signal-to-noise ratios.

Images

Pearson Correlation: Segmented Muscle Attenuation (CT) vs. Fat Fraction (MRI)

Non–Subtracted · Subtracted

Non-Subtracted: $R = -0.78$, $p < 2.2e{-}16$; $R = -0.81$, $p = 8.4e{-}07$

Subtracted: $R = -0.77$, $p < 2.2e{-}16$; $R = -0.81$, $p = 8.6e{-}07$

Y-axis: Mean Fat Fraction on MRI. X-axis: Mean Segmented Muscle Attenuation on CT (HU). Legend: CE, NON–CE.

Statement Regarding Human Subjects: This was a retrospective cohort study approved by the Institutional Review Board with a waiver of informed consent.

Statement Regarding Conflicts of Interest: None of the authors has a conflict of interest related to this project.

_____

Abstract # - 27 CT Fluoroscopy-Guided Percutaneous Direct type II Endoleak Embolization using n-BCA Glue

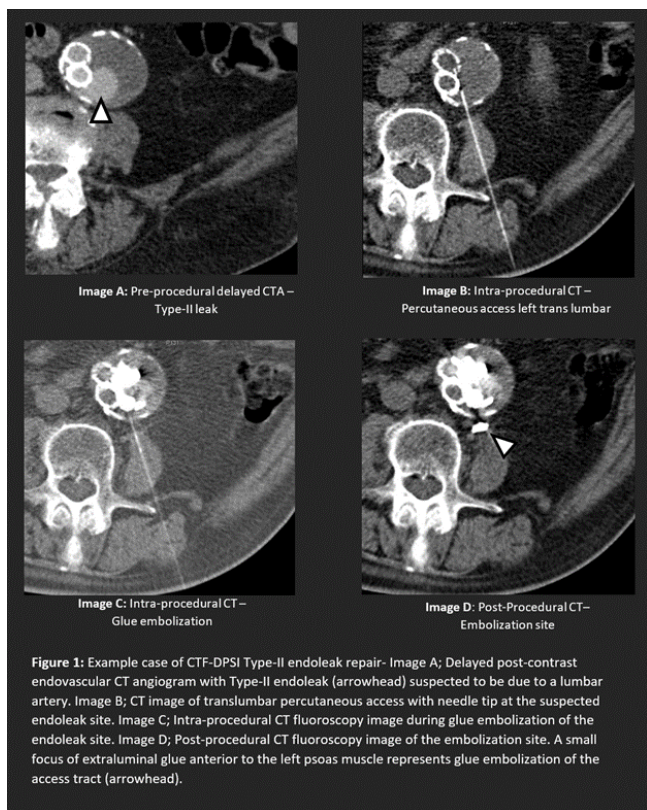Johannes du Pisanie, MD; Clayton Commander, MD, PhD, Hyeon Yu, MD; Charles Burke MD

University of North Carolina, Chapel Hill, NC

Background: The most performed Type-II endoleak leak repair methods utilize either transarterial or direct percutaneous sac puncture approaches with CT and/or fluoroscopic guidance. We investigate the technical and clinical feasibility of a novel modified direct percutaneous sac injection (DPSI) technique for treating type II endoleaks using CT fluoroscopy (CTF) guidance.

Materials and Methods: Data were retrospectively collected from 33 procedures performed on 29 patients (Mean age: 77.8 years ± 4.9; Male: female = 21:3) with Type II endoleaks between August 2019 and June 2022. Technical (intra-sac embolic deployment, complications, dose, and procedural time) and clinical (aortic aneurysm and endoleak size change) parameters were evaluated. The methodology includes using intermittent CT fluoroscopy to percutaneously guide a 20 or 21-gauge needle into the excluded aneurysm

sac. The position of the needle at the endoleak site is confirmed by imaging and by blood return through the needle. N-butyl cyanoacrylate glue (Histoacryl) and lipiodol are mixed in a 1:4 ratio. The needle, the glue mixture syringe, and a syringe of D5W (5% dextrose in water) are attached to a three-way stopcock. The glue mixture is slowly and intermittently injected in small aliquots. The needle is flushed with D5W between glue injections to prevent occlusion of the needle. Intermittent CT fluoroscopy is used to monitor for non-target embolization and appropriate filling of the endoleak channel.

Images

Image A: Pre-procedural delayed CTA – Type-II leak

Image B: Intra-procedural CT – Percutaneous access left trans lumbar

Image C: Intra-procedural CT – Glue embolization

Image D: Post-Procedural CT– Embolization site

Figure 1: Example case of CTF-DPSI Type-II endoleak repair- Image A; Delayed post-contrast endovascular CT angiogram with Type-II endoleak (arrowhead) suspected to be due to a lumbar artery. Image B; CT image of translumbar percutaneous access with needle tip at the suspected endoleak site. Image C; Intra-procedural CT fluoroscopy image during glue embolization of the endoleak site. Image D; Post-procedural CT fluoroscopy image of the embolization site. A small focus of extraluminal glue anterior to the left psoas muscle represents glue embolization of the access tract (arrowhead).

Results: There was no statistically significant difference in both aneurysm sac size (71.9 mm ± 15.3 vs 74.5 mm ± 16.5; p=0.56) and endoleak size (30.9 cm3 ± 21.4 vs 24.4 cm3 ± 40; p=0.47) before and after embolization. Average follow up was 9.2 months ± 5.3. Average radiation dose was 623.4 mGy*cm ± 334.6, procedure time was 38.5 min ± 17.1 and sedation time was 37.1 min ± 14. Two complications are reported including nontarget inferior mesenteric artery embolization resulting in patient death and needle bowel tenting on CT without clinical consequence.

Conclusions: CT fluoroscopy-guided direct percutaneous aneurysmal sac injection of glue is a safe and effective method for embolization of Type II endoleaks.

Clinical Relevance: The novel CTF-DPSI technique offers lower procedure times and radiation exposure as compared to conventional techniques. It also obviates the need for inter-suite transport and a guidewire-catheter system while maintaining intraprocedural embolic observation.

Statement Regarding Human Subjects: This study was approved by the IRB with waiver of informed consent.

Statement Regarding Conflicts of Interest: None of the Authors have a conflict of interest

Abstract # - 29 Imaging utilization of acute trauma in a resource-poor setting: Analysis of the Malawi trauma surveillance registry

Jordan Taylor, MD[1]; Thad Benefield, MS[1]; Benjamin Brown, MD, MPH[1]; Jared Gallaher, MD, MPH[2]; Anthony Charles MD, MPH[2,3]; Katrina McGinty, MD[1]

[1]Department of Radiology, University of North Carolina School of Medicine, Chapel Hill, NC. [2]Department of Surgery, University of North Carolina School of Medicine, Chapel Hill, NC. [3]Department of Surgery, Kamuzu Central Hospital, Lilongwe, Malawi

Background: Radiology offers rapid diagnoses in the acute trauma setting. However, in low to middle-income countries (LMIC), limited infrastructure and resources impair radiology utilization. The Malawi Trauma Score (MTS) was developed as a tool for trauma triage in Sub-Saharan Africa to predict injury-associated mortality based on history and physical. The role of radiology in the initial evaluation of trauma in this setting is not well understood. This study evaluates utilization of radiology during initial trauma assessment in a sub-Saharan health care setting.

Materials and Methods: A retrospective analysis was performed on all patients in the Kamuzu Central Hospital trauma surveillance registry in Lilongwe, Malawi, from 2019-2021. Analysis was limited to initial radiology studies performed in the emergency department. Using the Markov Chain Monte Carlo method, we imputed-and analyzed 20 complete-case data sets. Models were run to evaluate the association between number of studies and MTS (2-32), number of studies and operations performed, number of studies and level of care (LOC), and number of operations and MTS.

Results: 29,678 patients were included. The mean age is 27.5 years (SD 15.44) with a primarily male sample (78.14%). The number of studies performed were 7,376. The total number of operative interventions was 2,160. The number admitted was 4,789. MTS is negatively associated with number of studies (p<0.0001). Number of operations performed is positively associated with number of studies (p<0.0001). MTS is negatively associated with the number of operations (p<0.0001). Of patients admitted, there is evidence that an intermediate LOC is associated with an increased number of studies (p<0.0001). There is insufficient evidence of association between the number of studies and ward or ICU LOC (p=0.073 and 0.90).

Conclusion: In the acute trauma setting, the total number of imaging studies negatively correlates with MTS. Number of operations performed is positively associated with number of imaging studies. MTS is negatively associated with number of operations. Last, the number of imaging studies is positively correlated with an intermediate LOC.

Clinical Relevance: The MTS assists clinical officers in trauma triage. In cases of higher injury severity, there may be a decreased need for imaging, as unstable patients may need immediate operative intervention. Our findings will help inform health care resource allocation in austere settings.

Statement Regarding Human Subjects: This study has been approved by the UNC IRB.
Study #: 17-1210

Study Title: Secondary Analyses of Kamuzu Central Hospital Trauma Registry Data

This submission, Reference ID 357785, has been approved by the IRB.

Statement Regarding Conflicts of Interest: The authors have no conflicts of interest to disclose.

_____

Abstract # - 30 Sarcopenia and Associated Imaging Biomarkers in Patients Undergoing Transjugular Intraheaptic Portosystemic Shunt Placement

Vedang J. Patel BA; Marinelda Perlleshi, BS; Hyeon Yu, MD; Clayton W. Commander, MD, PhD

University of North Carolina School of Medicine, Chapel Hill, North Carolina

Background: For patients with decompensated cirrhosis, treatment of portal hypertension related complications such as variceal bleeding, refractory ascites, and hepatic hydrothorax often involves image-guided intervention. Most commonly, transjugular intrahepatic portosystemic shunt (TIPS) placement and obliteration of varices. Sarcopenia is defined as the progressive loss of muscle mass and strength, often induced by a systemic inflammatory response. In patients with decompensated cirrhosis, particularly those with diuretic-refractory ascites, sarcopenia is a major clinical concern and often a barrier to transplant.

Materials and Methods: A retrospective review of historical medical records at UNC Vascular and Interventional Radiology 2010 to 2022 was conducted, consisting of patients who underwent TIPS during the study period. Patients were organized into two groups based on the indication for TIPS (refractory ascites/hydrothorax and variceal hemorrhage). Segmentation of the paraspinous muscles was performed on computed tomography (CT) scans, allowing for skeletal muscle index (SMI) and skeletal muscle density (SMD) to be determined.

Results: Sixty-six patients met inclusion criteria with an average interval between CT and TIPS of 1 month, ranging from 1 day to 3 months. Sarcopenia was defined as an SMI < 10.4 (cm2/m2). The incidence of sarcopenia was significantly higher in patients who underwent TIPS for ascites/hepatic hydrothorax than those with variceal bleeding (p<0.001). In patients with sarcopenia, SMD in venous phase imaging was significantly higher relative to those without sarcopenia (p<0.01). There was no difference in MELD score or mortality between the two groups (p=0.58) or between patients with and without sarcopenia (p=0.22).

Conclusions: The increased incidence of sarcopenia in patients with ascites/hepatic hydrothorax is consistent significant protein wasting in comparison to those with variceal bleeding. It is unclear why SMD was higher in patients with sarcopenia however we theorize this finding may reflect underlying systemic inflammation, known to be present in cirrhotic patients with ascites. Further retrospective and prospective validation is warranted as incorporation of sarcopenia as a predictive factor may reduce associated morbidity and healthcare cost.

Clinical Relevance: Sarcopenia is an important imaging biomarker which can help predict outcomes for patients undergoing percutaneous intervention for portal hypertension.

Statement Regarding Human Subjects: Institutional IRB (22-1343) approval was obtained prior to study commencement that included waivers for informed consent. Data was collected from existing patient records and recorded in a deidentified database.

_____

Abstract # - 31 Radiation Safety Education and Diagnostic Imaging in Pediatric Patients with Surgically Treated Hydrocephalus: The Patient and Family Perspective

Diane M. Armao, MD[1]; Terry S. Hartman, MPH, MS, CCRC[2]; Laurence Katz, MD[3]; Christopher Shea, MA, MPA, PhD[4]; Jenna Koschnitzky, PhD[5]; Richard Yang, MD[6]; Keith Smith, MD[7]; Carolyn Quinsey MD[8]

[1]UNC School of Medicine Department of Radiology, Chapel Hill NC, NC. [2]UNC School of Medicine, Chapel Hill, NC. [3]UNC School of Medicine Dept. Emergency Medicine, Chapel Hill, NC. [4]UNC Gillings School of Global Public Health, Chapel Hill, NC. [5]former Director of Research Hydrocephalus Association, Bethesda, MD. [6]former summer research intern student at UNC School of Medicine Dept. Radiology, Chapel Hill NC, NC. [7]UNC School of Medicine Dept. Radiology, Chapel Hill NC, NC. [8]UNC School of Medicine Dept. Neurosurgery, Chapel Hill, NC

Background: Children with surgically treated hydrocephalus receive numerous head computed tomography (CT) scans throughout their lifetime. Most providers and patients/caregivers believe that the risks of radiation should be communicated before CT scans. Despite this, the communication of risks and benefits with caregivers is inconsistent and unknown. This study aimed to survey patients and caregivers about radiation safety in CT and obtain communication preferences.

Materials and Methods: A interactive educational workshop about pediatric CT radiation safety and diagnostic imaging was held for patients and caregivers at a national conference on hydrocephalus. To measure the impact of the session and communication preferences, pre-/post-session surveys were used to obtain feedback from participants.

Results: A total of 34 participants attended our workshop and all attendees completed the surveys. Of these, 28 attendees were parents of individuals with hydrocephalus. A total of 24 (71%) of participants were not informed by healthcare providers about the risks and benefits of CT scans and all participants (N=34) wanted this conversation prior to the CT. Following the session, 26 participants (76%) demonstrated that their knowledge of risks of radiation exposure increased (p<0.01). A total of 33 participants felt that informed consent should be obtained prior to CT scans after the session, an increase from 30 prior to the session. The median number of CT scans that individuals received for shunt evaluation was 25 (IQR 20) and 14% of children and young adults received over 100 scans.

Conclusions: Based on our study, caregivers uniformly want to be informed of radiation risks and benefits. Mechanisms for communication could include education and co-designed care plans. Collaboration between radiologists, providers and parents is essential for the development and testing of credible, high-quality online and social media resources. Future research priorities include the development and testing of resources covering diagnostic imaging specifically tailored to the needs and expectations of providers and parents of surgically treated hydrocephalus patients.

Clinical Relevance: Since head CTs are frequently required for the evaluation of shunt malfunction in an emergent setting, proactive dialogue between providers and patients, and educational resources that are

accurate and easily accessible may prove the best pathway.

Images
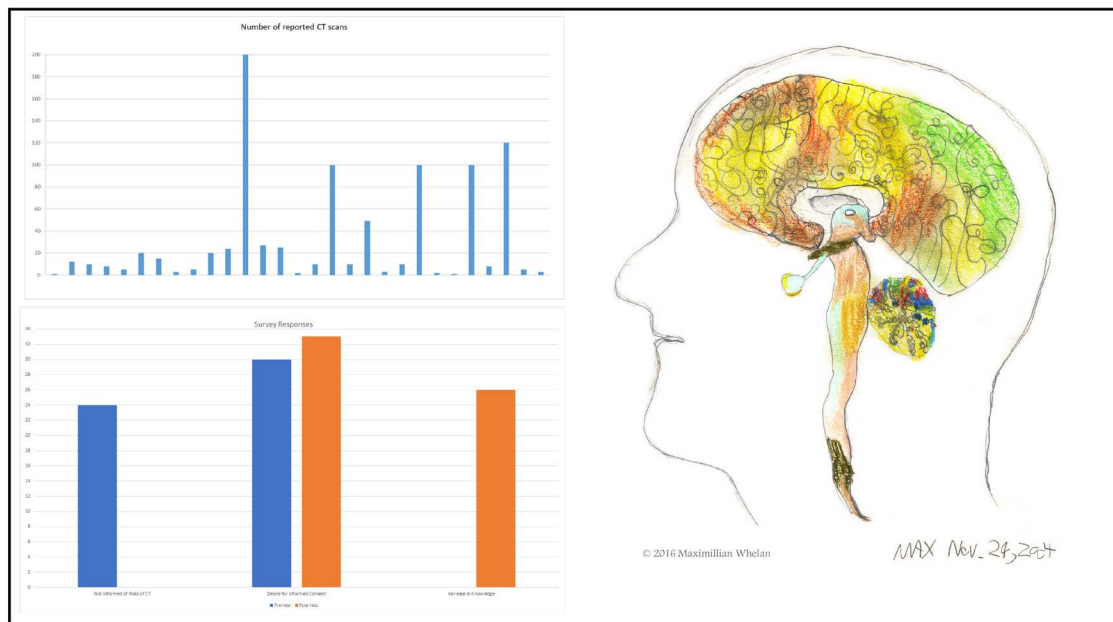
Statement Regarding Human Subjects: The University of North Carolina at Chapel Hill Biomedical IRB determined that this study was exempt from IRB review 492 Childs Nerv Syst (2021) 37:491–497 under 45 CFR 46.101(b).

Statement Regarding Conflicts of Interest: The authors have no conflicts to disclose.

Abstract # - 32 Case Report: Pituitary adenoma associated with xanthogranuloma

Peter Noone, MD[1]; Diane M. Armao[2]; Valerie Jewells, MD[2]

[1]Former Neuroimaging Fellow, UNC School of Medicine Dept. Radiology, Chapel Hill, NC. [2]UNC School of Medicine, Dept. Radiology, Chapel Hill, NC

Background: Pituitary adenoma with an associated xanthogranuloma (XG) is very rare with only a few reported cases. XG of the sellar region is rare, with an incidence < 1% of all sellar lesions. Sellar XG is an independent clinical entity recognized by the World Health Organization since 2020. Cases of pituitary adenoma with concomitant XG are extremely rare, with a total of 16 cases in the literature. Pituitary adenoma with an associated XG lacks specific clinical and radiologic signs, making pre-operative diagnosis challenging. Herein, we report a case of pituitary adenoma accompanied by a XG and describe the radiologic and pathologic characteristics and clinical outcome.

Case Description: A 40-year-old male patient presented to an outside hospital with a one-month history of decreased and blurry vision in the left eye. Ophthalmologic examination revealed a bitemporal visual field defect. A brain MRI showed a solid and cystic sellar mass with suprasellar extension and compression of the optic chiasm, consistent with pituitary macroadenoma [Fig.1]. The patient was referred to our institution

for evaluation and treatment. Endocrinologic evaluation revealed mild hyperprolactinemia presumably due to stalk effect, concurrent hypogonadotropic hypogonadism and a clinically non-functional pituitary macroadenoma. Gross total resection of the sellar mass was performed using an endoscopic endonasal transsphenoidal approach. There were no procedural complications. Histopathological findings revealed pituitary adenoma with xanthogranulomatous features, immunophenotypically consistent with a type 1 silent corticotroph adenoma. The XG component was separate from the adenoma and showed focal necrosis, hemosiderin deposition, fibrosis, multinucleated giant cells and cholesterol clefts [Fig.1]. Four-month follow-up MRI revealed no evidence of residual or recurrent disease. Endocrinologic assessment at five-months showed the patient to be in a state of good health, without need for steroids or hormone replacement therapy. Ophthalmologic evaluation at five-months revealed resolution of the bitemporal visual field defects.

Conclusion: We discuss the possible histogenesis of XGs, and the clinical features and neuroimaging findings that could serve to alert clinicians to including this entity in the differential diagnosis.

Images
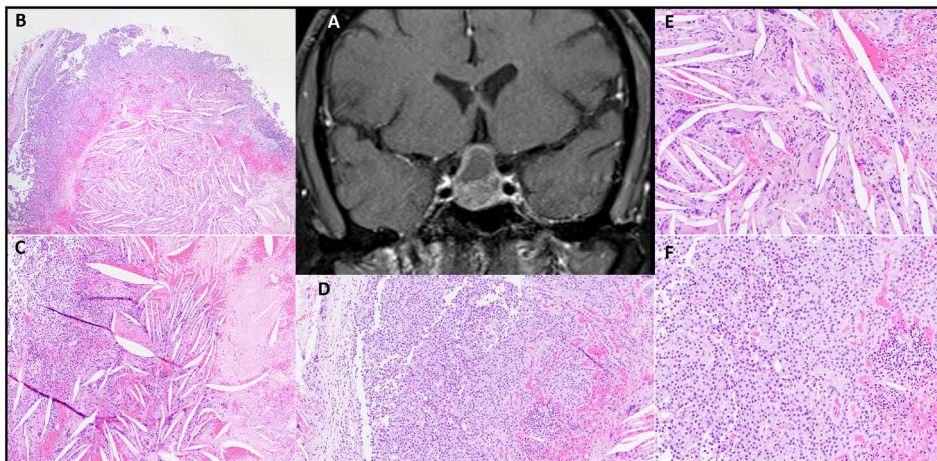
Statement Regarding Human Subjects: This case was presented at a multidisciplinary conference, did not contain patient identifiers and is HIPPA compliant.

Statement Regarding Conflicts of Interest: The authors have no conflicts to disclose.

_____

Abstract # - 33 Prevalence of exposures that modify breast density prior to breast cancer screening

Ley A. Killeya-Jones, Yukie Kajita, Cherie M. Kuzmiak, Jessica R. Barbee, Sarah J. Nyante

University of North Carolina at Chapel Hill, Chapel Hill, NC

Background: Dense breast tissue is associated with delayed breast cancer detection due to its ability to obscure tumors on mammography. Several modifiable factors are associated with breast density, including alcohol use (associated with higher density) and smoking and non-steroidal anti-inflammatory drug (NSAID) use (both associated with lower density). We evaluated the prevalence of smoking, alcohol, and NSAID use immediately prior to screening, with the hypothesis that recent exposure is common.

Materials and Methods: Participants were women attending UNC Hospitals for a screening mammogram between October 2020 and March 2022. Eligible women were postmenopausal, had no prior history of breast cancer or implants, and had not used hormonal birth control, menopausal hormones, or chemoprevention within 30 days. 301 women provided informed consent and self-reported smoking history (cigarette and electronic [e-] cigarette), alcohol use (in past 24 hours), and NSAID use (in past 48 hours) at the time of their mammogram. Body mass index (BMI) was calculated from self-reported height and weight. Age, race, and ethnicity were obtained from medical records. Chi-square and Mann-Whitney U tests were used to compare data distributions.

Results: Participants' mean age was 64.7 years (SD=8.0, min=49, max=84). Race was identified as White (69%), Black (25%), or Other (6%); 4% of participants were Hispanic. The mean BMI was 29.5 kg/m2 (SD=6.8). Overall, 8% of women smoked cigarettes, 2% smoked e-cigarettes, 23% drank alcohol, and 44% used an NSAID prior to their mammogram. The mean time since last smoking was 7.4 hours (SD=10.9) for cigarettes and 7.2 hours (SD=7.4) for e-cigarettes. Smoking was more common among younger women (P<0.01), alcohol use was more common among women who were White (P=0.01), older (P=0.03), and had a lower BMI (P<0.01), and NSAID use was more common among women with a higher BMI (P=0.01).

Conclusion: Recent NSAID and alcohol use was common among postmenopausal breast cancer screening participants, with differences in use according to personal characteristics. Future analyses will examine whether NSAID use or alcohol use is associated with breast texture or the screening exam assessment.

Clinical Relevance: High breast density is associated with tumor masking and delayed cancer detection. Awareness of exposure to factors that modify breast density may aid diagnostic interpretation.

Statement Regarding Human Subjects: This study was approved by the Institutional Review Board of the University of North Carolina at Chapel Hill (Study #19-0793). All participants provided written informed consent and HIPAA authorization.

Statement Regarding Conflicts of Interest: The authors have no conflicts of interest to disclose.

_____

Abstract # - 34 Interactions between Bifidobacterium and Bacteroides and human milk oligosaccharides are associated with infant cognition

Seoyoon Cho, MS[1]; Kristine Baluyot[1]; Brittany R Howell[2]; Heather C. Hazlett[1]; Jed T. Elison[3]; Weili Lin[1]

[1]University of North Carolina at Chapel Hill, Chapel Hill, NC. [2]Virginia Polytechnic Institute and State University, Roanoke, Virginia. [3]University of Minnesota, Minneapolis, Minnesota

Background: Gut microbiota composition and human milk (HM) oligosaccharide (HMO) have been shown to be associated with infant cognition. We aimed to determine how interactions of HMOs and species of Bacteroides and Bifidobacterium genera in human gut microbiota could lead to associations with early cognitive development, and how the associations depend on the Alpha-Tetrasaccharide (A-tetra) status in HM.

Materials and Methods: 170 HM samples from 105 typically developing children who were at least

predominantly breastfed were enrolled. The primary outcome measures were the Mullen Scales of Early Learning (MSEL) scores for assessing early cognitive development. Linear mixed effects models (LMEMs) including both HMOs and gut microbiota as main effects and their interactions were employed for the association analyses with group least absolute shrinkage and selection operator for variable selection. Unstratified, detectable A-tetra (A-tetra+), and undetectable A-tetra (A-tetra-) stratified LMEMs were fitted.

Results: Gross motor was positively associated with B. fragilis and B. vulgatus at multiple LMEMs. Fine motor showed significant positive association with B. ovatus and significant negative association with the interaction between Lacto-N-tetraose (LNT) and B. longum. Using A-tetra+ stratified model, visual reception showed significant positive association with 3-Fucosyllactose (3-FL), negative associations with B. catenulatum and its interaction with Lacto-N-fucopentaose-I. At unstratified model, expressive language had significant negative association with A-tetra. Finally, at A-tetra- stratified model showed significant positive associations with the interaction between 3'-Sialyllactose (3'-SL) and B. bifidum, 6'-SL and B. fragilis, and 3-FL and B. catenulatum as well as significant negative associations with the interaction between LNT and B. breve and LNT and B. longum.

Conclusion: Our results showed that species of Bacteroides and Bifidobacterium and HMOs could be independently associated with infant cognition. More importantly, interactions between gut microbiota and HMOs uncovered additional associations with cognition, suggesting different biological mechanisms among HMOs yielding effects on early cognitive development.

Clinical Relevance: The understanding of how HMOs in HM, gut microbiota and their interactions may be associated with cognition underscores the importance of breast feeding in early cognitive development.

Statement Regarding Human Subjects: All participating subjects signed informed consent.

Statement Regarding Conflicts of Interest: Weili Lin is a consultant of and had received travel support from Nestlé SA, Switzerland.

_____

Abstract # - 35 Advanced MRI Imaging of the Ascending Auditory Pathway to Evaluate Hearing Loss

Pirapat M. Rerkpattanapipat, MS; Yueh Z. Lee, MD, PhD

University of North Carolina School of Medicine, Chapel Hill, NC

Background: Sensorineural hearing loss (SNHL) can be multifactorial and results from dysfunction in the cochlea or spiral ganglion. One of the proposed etiologies of SNHL involves abnormalities in the stria vascularis (SV) found in the cochlea. The SV, which is critical to producing hearing, requires significant blood flow to retain function. Structures such as the cochlear nuclei and inferior colliculi are also vital to the ascending auditory pathway. These structures are on the order of 0.5 to 1.0 mm and are difficult to visualize on conventional MRI based imaging approaches. However, given their importance in hearing loss, developing focused approaches would improve our understanding of the pathophysiology of hearing loss, as well as enable diagnostic tools that would improve surgical outcomes on procedures in the temporal bone. This study utilizes specialized MRI sequences, time-of-flight magnetic resonance angiography (TFA MRA), and diffusion tensor imaging (DTI) to visualize these inner brain structures and inner ear blood flow.

Materials and Methods: 1. The FLAWS sequences have been shown to enable visualization of brainstem nuclei. This study analyzes FLAWS acquisitions on 3T MRI case studies and will apply FLAWS at 7T MRI to enable visualization of critical structures in the ascending auditory pathway.

2. Apply TOF MRA approaches to identify and evaluate flow in the stria vascularis and other vascular structures of the cochlea.

3. Analyze DTI white matter connectivity patterns to help visualize the critical ascending auditory structures.
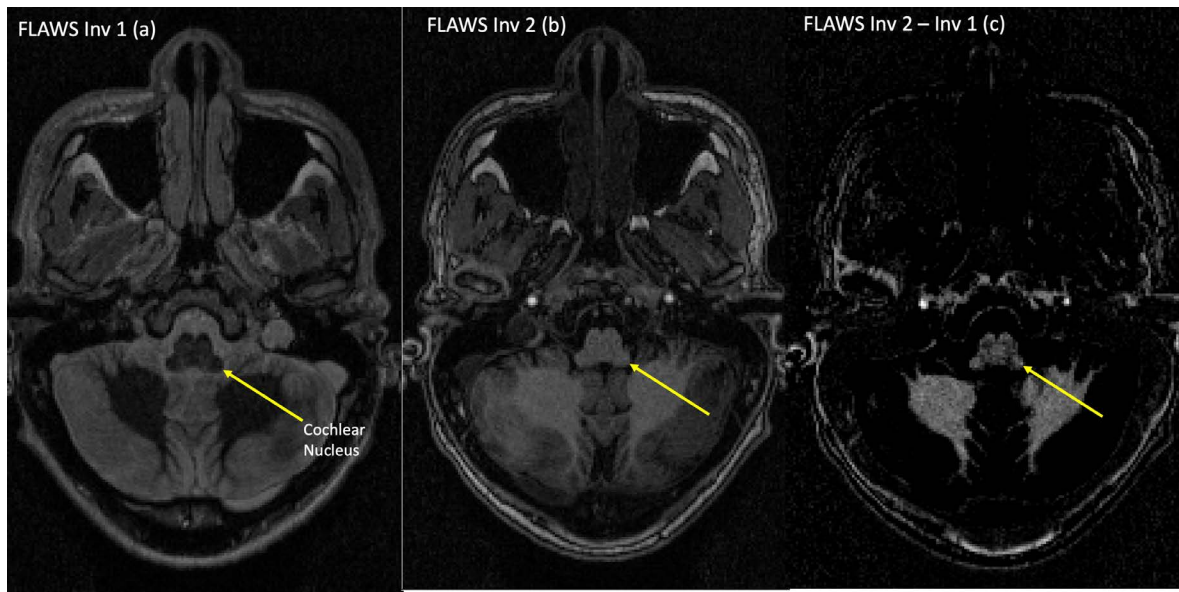
Images

Figure 1: Subtraction of (a) from (b) shows improved visualization of cochlear nucleus (arrow) in (c).

Results: Analysis of case study data of FLAWS on 3T MRI shows visualization of the cochlear nuclei after a post-processing image subtraction (Figure 1).

TOF MRA and DTI acquisitions are in progress. Preliminary TOF scans show that flow in the inner ear region can potentially be detected with the optimal parameters, which we are currently evaluating.

Conclusion: A combination of specialized MRI sequences and DTI can be utilized to analyze the ascending auditory pathway. There is potential that TOF MRA can be used to analyze blood flow to the inner ear.

Clinical Relevance: Over 5% of the population is impacted by some form of disabling hearing loss. Our state is also home to Fort Bragg and a significant veteran population. 7.5% of veterans report hearing loss associated with their deployment. Thus, this is a critical health problem in our community, especially our military community.

Statement Regarding Human Subjects: This study complies with informed consent and HIPAA authorization.

Statement Regarding Conflicts of Interest: There are no conflicts of interests to disclose.

Abstract # - 36 Healthy Eating Indices are associated with early cognitive and temperament development

Jiarui Tang[1], Yue Yang[1], Kyle Burger[1], Kristine Baluyot[1], Brittany R. Howell[2], Jed T. Elison[2], Heather C. Hazlett[1], Tengfei Li[1], Hongtu Zhu[1], Weili Lin[1]

[1]University of North Carolina, Chapel Hill, NC. [2]University of Minnesota, Minneapolis, MN

Background: Adequate nutrition is of critical importance for early cognitive and temperament development. In this study, we aimed to uncover the potential relationship between quality of dietary intakes and cognitive and temperament development in typically developing children aged 2 to 3 years old.

Materials and Methods: Dietary intake records (217 records) were collected using 24-hour dietary recall from 154 children aged between 2 to 3 years old. Two records were collected from each subject at each visit including one from a weekday and the other during the weekend. Subsequently, weighted averages were used to merge these two records for each subject. The Mullen Scales of Early Learning (MSEL) was used to assess cognition whereas The Early Childhood Behavior Questionnaire (ECBQ) was used for temperament. Healthy Eating Indices 2015 (HEI-2015) were calculated to evaluate the diet quality of each subject. Mixed effect linear regression models were utilized to determine the associations of MSEL and ECBQ with HEI total scores and its subgroup scores. The covariates included sex, maternal education and household income.

Results: No significant relationships were observed between HEI total scores and MSEL and ECBQ. In contrast, total vegetables HEI (adjusted p=0.005) and total fruits HEI (adjusted p=0.035) show significant positive associations with MSEL visual reception. In contrast, saturated fatty acid HEI (adjusted p=0.049) has a significant negative association with MSEL expressive language. Finally, added sugar HEI has a significant negative association with ECBQ surgency (adjusted p=0.048).

Conclusion: Our results shed light on our understanding of the associations between dietary intake quality and brain cognitive and temperament development in typically developing children aged 2 to 3 years old.

Clinical Relevance: Results from our study could provide guidance on proper dietary intake quality for cognitive and temperament development in early childhood.

Statement Regarding Human Subjects: All subjects have signed consent.

Statement Regarding Conflicts of Interest: WL is a consultant of and had received travel support from Nestlé SA, Switzerland.

_____

Abstract # - 37 The development and application of a cost-effective cervical spine phantom for use in fluoroscopically guided lateral C1-C2 puncture training

Victoria Risner; Benjamin Huang, MD; Kassie McCullagh, MD; Yueh Lee, MD, PhD

University of North Carolina, Chapel Hill, North Carolina

Background: Lateral C1-C2 puncture is a rare procedure performed by neuroradiologists for various purposes, including CSF collection and contrast injection, when lumbar puncture is not available. Due to the

infrequency of this procedure, there are limited opportunities to learn and practice the technique. We aimed to develop and assess the efficacy of a low-cost, reusable cervical spine phantom for use in fluoroscopically guided lateral C1-C2 puncture training.

Methods and Materials: Model Construction: The phantom was constructed using a modified PVC cervical spine model, an outer latex tubing with a 12.7mm inner diameter representing the spinal canal, an inner latex modeling balloon with 5mm outer diameter representing the spinal cord, and alginate encompassing the model to replicate soft tissue. The total cost of materials for one model was approximately $65. The outer tube was filled with water and the inner balloon filled with dyed water so the spinal tap would reveal dyed water if the "spinal cord" was punctured. A valve was placed on one end of the outer tubing and a hemostat was used to secure the other end to maintain pressure and seal the canal. This enabled refilling of the canal and replacing of the latex balloon if the balloon was punctured in a previous attempt. Assessment of Training Efficacy: Residents and fellows were provided with a pre- and post-survey assessing for comfort level in performing a puncture, confidence in having a successful puncture, and perception of current knowledge of the steps in a puncture. Training sessions were led by neuroradiology faculty at a single institution using the phantom model under fluoroscopic guidance. Survey questions were assessed on a 5-point Likert scale.

Results: The sample size of the training group was 9. Comfort level was improved by 1.6 points (standard deviation [SD]: 0.9), confidence by 1.2 points (SD: 0.8), and perception of current knowledge by 2.2 points (SD: 0.8). 78% of participants found the model to be "very helpful" (5/5 on Likert scale), and all participants were "very likely" to recommend others to sign up for this workshop.

Conclusions: This cervical phantom model is a low cost, replicable, and demonstrates clinical training utility to better prepare residents for lateral C1-C2 puncture.

Clinical Relevance/Application: Lateral C1-C2 punctures are rare procedures, so the use of a phantom model prior to patient encounters will be invaluable to resident education and training.

Images

Statement Regarding Human Subjects: This project has been reviewed by the Office of Human Research Ethics and was determined to be exempt from further review by the UNC IRB.

Statement Regarding Conflicts of Interest: The authors have no conflicts of interest to disclose.

_____

Abstract # - 38 A retrospective chart review exploring lesion characteristics, treatment, and outcomes of adenoid cystic carcinoma of the breast

Victoria Risner[1]; Thad Benefield[2]; Terry Hartman, MPH, MS[2]; Michael Taylor-Cho, MD, MPH[3]; Sheryl Jordan MD[2]

[1]UNC School of Medicine, Chapel Hill, North Carolina. [2]University of North Carolina at Chapel Hill, Chapel Hill, North Carolina. [3]Duke University, Durham, North Carolina

Background: Adenoid cystic carcinoma (AdCC) tumors of the breast are uncommon, and it is important for radiologists to recognize these tumors and the next appropriate step in patient care. We aimed to expand current knowledge of AdCC diagnoses by correlating newly published (and revised) 2019 World Health Organization classification system with two institutions' case-based experience of AdCC.

Materials and Methods: We conducted a retrospective chart review of patients diagnosed with AdCC of the breast at UNC Chapel Hill and Duke University from January 1, 2001 to March 29, 2021. Variables included lesion location/size, radiologic description, imaging data, breast density, axillary node involvement, pack-years, and treatment modalities.

Results: 25 patients were diagnosed with AdCC between 2001 and 2021 at UNCCH and Duke, with three patients receiving a diagnosis after release of the 2019 WHO classification system. 92% were female and average age of diagnosis was 56.88 (SD: 13.78). There was minimal smoking history, with average pack-years of 2.15 (SD: 4.32). One patient was BRCA2 positive, 6 had negative genetic results, and 18 did not undergo genetic testing. 80% of patients received a mammogram, with 20% BIRADS breast density category A, 50% BIRADS B, 30% BIRADS C, and no patients with BIRADS D (extremely dense breast). Average lesion size on imaging was 1.98 cm (SD: 1.24), while average tumor size on resection was 2.42 cm (SD: 1.12). 19 patients had on average 3.05 (SD: 2.9) axillary lymph nodes biopsied, but only one patient was positive. Four tumors were ER+, the remaining were triple negative. 60% only received surgical resection, and 28% received chemotherapy, 40% radiation therapy, 20% hormonal therapy in addition to surgical resection. Follow up time was highly variable, but 96% of patients survived to follow up.

Conclusion: There was wide variability in treatment plan, yet the vast majority of patient's survived to follow up, consistent with the excellent prognosis of AdCC of the breast. 76% of patients received axillary lymph node biopsy; however, only 5.3% had positive nodes. Future analytical plans include comparing changes based on the new WHO criteria, and comparing differences in population, presentation, and treatment between two institutions.

Clinical Relevance: This retrospective cohort provides valuable information on lesion characteristics, treatments, and outcomes in institutional-specific populations of AdCC of the breast.

Statement Regarding Human Subjects: The IRB has determined that the study-specific rationale provided

by the investigator is sufficient to justify the waiver of informed consent for research and waiver of HIPAA authorization.

Statement Regarding Conflicts of Interest: The authors have no conflicts to disclose.

_____

Abstract # - 39 19F Cenya BEACONs magnetic resonance imaging parameter optimization

Sang Hun Chung[1,2]; Yueh Z Lee, MD, PhD[3,4,5]

[1]UNC Chapel Hill, Chapel Hill, NC. [2]Biomedical engineering, Chapel Hill, NC. [3]UNC CHapel Hill, Chapel Hill, NC. [4]Department of Radiology and Biomedical Research imaging, Chapel Hill, NC. [5]Division of Pulmonary and Critical Care Medicine, Chapel Hill, NC

Background: Fluorinated compounds are chemically inert, non-toxic and abundant in nature, furthermore, the fluorine isotope 19F has negligible endogenous magnetic resonance (MR) signal, making 19F a promising compound for cell tracking. 19F labeled cells, when imaged with magnetic resonance imaging (MRI) opens the possibility of radiation free tracking and quantification of therapeutic and immune cells. Cenya© BEACONs have been shown to be non-toxic in vivo, have retention with cell division, and MRI detectable for up to 2 weeks. This study shows the preliminary results of MRI parameter optimization using Cenya BEACONs phantoms.

Materials: MRI scans were performed on the Bruker Biospec 9.4T using a custom volume coil dual tunned to 1H and 19F. scans were performed on Cenya BEACON phantoms (2mg/mL) and trifluoroacetic acid (TFA) (50 Mm).

Methods: Imaging was performed at 9.4T using the Bruker FLASH sequence (TE 1.77 ms; TR 50,100,500,1000,1500 ms; resolution 1.5X1.5X5 mm; averages 380,188,38,19,13; Flip angles 38.8 52.6 85.3 89.6 90; scan time 10 min). A reference TFA sample was included in each scan.
SNR was calculated for each image and background noise was compared to number of averages. T1 was calculated using the variable flip-angle estimation.

Results:
Cenya BEACONs was found to be -15.81 ppm from TFA and T1 was calculated to be 832.9 ms at 9.4T. The resulting SNR for each image was 14, 10.9, 10.6, 9, 6.78. The background noise standard deviation reduction from averages plateaus near 380 averages as shows in Fig 1.

Conclusion: For optimal Cenya BEACONs MR imaging, we have found that ~200 averages is the point were SNR gains start losing efficiency for a scan time of 10 minutes. A TR of 50 and a flip angle of 38.8 yielded the best SNR. For longer scans it is recommend to keep the averages to 200, adjust TR to maximize flip angle based on the Ernst equation and minimize bandwidth.

Clinical Relevance: Optimizing MRI parameters allows minimizing scan time and increasing sensitivity of the target compound, allowing achievement of maximum sensitivity given existing time constraints. further work will continue optimization for 3T and potentially 7T acquisitions for clinical/translational imaging of cells, such as macrophages or CAR-T cells.

Images
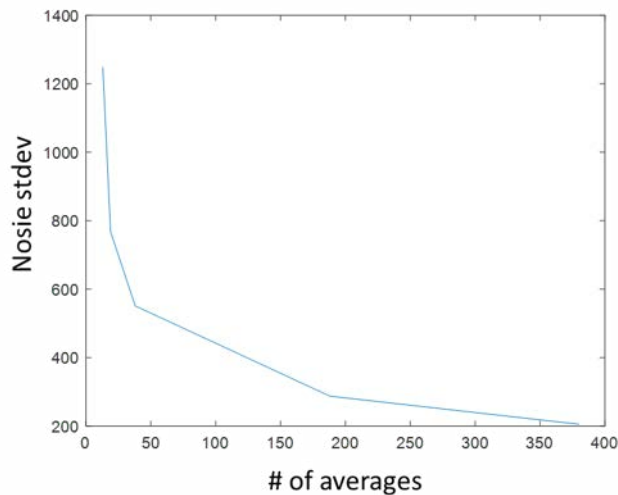
Statement Regarding Human Subjects: No human subjects participated in this study

Statement Regarding Conflicts of Interest: The authors have no conflicts of interest to disclose

_____

Abstract # - 40 Association of Liver Reporting and Data System Treatment Response (LR-TR) and modified Response Evaluation Criteria in Solid Tumor (mRECIST) Classification Systems for Stereotactic Body Radiation Therapy (SBRT)-treated Hepatocellular Carcinoma (HCC) Lesions

Diwash Thapa, BS; Thad Banefield, MS; Andrew Moon, MD, MPH; Katrina McGinty, MD; Lauren Burke, MD

University of North Carolina School of Medicine, Chapel Hill, NC

Background: LIRADS Treatment Response (LR-TR) is an image classification system that aims to provide a simple assessment of response to locoregional therapy for hepatocellular carcinoma (HCC). The LR-TR algorithm is similar to a predecessor, modified Response Evaluation Criteria in Solid Tumor (mRECIST), given that they are both based on imaging assessment of arterial enhancement of masses. However, LR-TR expands upon the criteria considered for a viable tumor, which may need to be considered for retreatment. HCC lesions treated with stereotactic body radiation therapy (SBRT) may be more difficult to characterize with these two systems given that persistence of arterial phase hyperenhancement (APHE) immediately following stereotactic body radiation therapy (SBRT) is known to occur even in pathologically nonviable tumors.

Materials and Methods: We performed a retrospective analysis of SBRT-treated lesions from 2012 to 2018 at UNC-CH. Two board-certified body radiologists with >10 years of experience read MRI pre-procedure and post-procedure at 3, 6, 9, and 12 months. The reader assigned each nodule LR-TR and mRECIST categories. Nodules without any post-procedure MRI were excluded.

To study the temporal association of mRECIST and LR-TR we implemented a mixed-effects logistic

regression. We also performed a receiver operator curve (ROC) analysis to determine if the difference in mRECIST size from pretreatment is predictive of disease recurrence for LR-TR equivocal lesions. The "gold standard" for recurrence was defined as need for retreatment of the same or other nodules. The area under the curve (AUC) was generated at 3 months; 3 and 6 months; and all time points.

Results: In figure.

Lesion Characteristics

Total # of lesions	53
Average pre-treatment size of lesion (cm)	2.62

LR-TR – mRECIST Association

Overall association	Yes ($p = 0.011$)
Differential association in time	No ($p = 0.88$)
Predicted mRECIST probability LR-TR, non-viable	0.96
Predicted mRECIST probability LR-TR, equivocal	0.50 ($p = 0.098$)
Predicted mRECIST probability LR-TR, viable	0.41 ($p = 0.036$)

ROC Analysis of LR-TR Equivocal Lesions Using mRECIST Size Changes as Discriminator

Time	N	AUC	p value
3 months	14	0.57	>0.99
3, 6 months	22	0.55	0.77
3, 6, 9, and 12 months	30	0.48	0.94

Conclusion: There is no inflection point in time where the association in LR-TR and mRECIST classification changes. This might be because APHE can persist at least 12 months and our study didn't last long enough to capture this point. The predicted probability of mRECIST classification was higher for LR-TR non-viable lesions. Notably, these lesions lack APHE, and the finding might reflect reader confidence conferred by this imaging characteristic. We did not find evidence that mRECIST size could be used to provide further guidance in predicting recurrence for LR-TR equivocal lesions.

Clinical Relevance: Given the importance of accurately assessing treatment response after SBRT, this study elucidates the various associations between LR-TR and mRECIST classification schemes.
Image upload

Statement Regarding Human Subjects: A waiver for informed consent and HIPAA authorization for research participants was granted under UNC IRB 18-2376

Statement Regarding Conflicts of Interest: The authors do not have any COI to disclose.

_____

Abstract # - 41 Transcatheter Fluoroscopic Embolization of Rabbit Fallopian Tube Using n-butyl-2-cyanoacrylate (NBCA): A Pilot Study for Non-Surgical Sterilization

Diwash Thapa, BS[1]; Gabrielle Daso, BS[2]; Diego Hipolito, MD[1]; Stephanie Montgomery, PhD[1]; Maureen Kohi, MD[1]; Jessica Stewart MD[2]

[1]UNC SOM, Chapel Hill, NC. [2]David Geffen School of Medicine at UCLA, Los Angeles, CA

Background: Laparoscopic female sterilization techniques carry non-negligible surgical risks. Transvaginal

tubal occlusion is a viable alternative that can mitigate these risks. However, research on the use of appropriate technique is needed owing to the failure of prior hysteroscopic sterilization devices. Notably, complications of the Essure device were due in part to mispositioning. Interventional radiologists can use fluoroscopic guidance to selectively catheterize and embolize segments of the fallopian using transvaginal access. We test such an approach on a rabbit model using n-butyl-2-cyanoacrylate (NBCA) and micro-coil as embolic.

Materials and Methods: 10 experimental female rabbits were sterilized with NBCA in one tube and NBCA + microcoil in the contralateral tube. The cervix was accessed with a curved 5 french catheter and hydrophilic guidewire through a 9 french balloon catheter from the FluoroSet kit. The catheter-guidewire assembly was advanced up to the ostium to facilitate catheterization of the fallopian tubes with a 2.4 french microcatheter and microwire. After engaging the tubes with the microwire, immediate salpingography was performed to visualize tubal anatomy and the microwire was further advanced to the isthmic portion. NBCA mixed with lipiodol in a 1:2 mixture was then administered through the microcatheter while simultaneously withdrawing it and filling the entire middle portion of the tube. The contralateral fallopian tube was embolized next following the same steps but with the addition of a Tornado embolization coil prior to administration of the NBCA-lipiodol mixture. At the 30-day post-procedure mark, rabbits were evaluated for tubal occlusion with a bilateral salpingography. The rabbits were subsequently euthanized, and the fallopian tubes were harvested for grading of inflammation and fibrosis using a semi-quantitative scale: absent (0), mild (1), moderate (2), or marked (3).

Results: Summarized in table 1.

Result	Overall	NBCA	NBCA + Coil
Procedural success rate (%)	85	90	80
Radiological occlusion rate (%)	76	78	75
Histological occlusion rate (%)	82	100	63
Inflammation rate (%)	65	56	75
Mean inflammation score	0.62	0.56	0.69
Fibrosis rate (%)	65	67	63
Mean fibrosis score	0.94	1.00	0.88

Conclusion: This pilot study demonstrates that embolization of fallopian tubes using NBCA mixed with lipiodol administered via a microcatheter is technically feasible. A 76% short-term occlusion rate is reasonable but can be improved upon with intraoperative expertise.

Clinical Relevance: This study presents an important step in determining the feasibility of fallopian tube embolization as a potentially safe and non-surgical method of contraception.

Statement Regarding Human Subjects: No human subjects were used.

Statement Regarding Conflicts of Interest: The authors have no COI to disclose.

Abstract # - 43 Charting normal knee cartilage thickness trajectories and localizing individual cartilage changes using data from the entire Osteoarthritis Initiative cohort

Tengfei Li[1], Tianyou Luo[2], Boqi Chen[3], Chao Huang[4], Zhengyang Shen[3], Zhenlin Xu[3], Daniel Nissman[1], Yvonne M. Golightly[5], Amanda E. Nelson[6], Marc Niethammer[3], Hongtu Zhu[2]

[1]Department of Radiology, University of North Carolina at Chapel Hill, Chapel Hill, NC. [2]Department of Biostatistics, University of North Carolina at Chapel Hill, Chapel Hill, NC. [3]Department of Computer Science, University of North Carolina at Chapel Hill, Chapel Hill, NC. [4]Department of Statistics, Florida State University, Tallahassee, Florida. [5]Department of Epidemiology, University of North Carolina at Chapel Hill, Chapel Hill, NC. [6]Division of Rheumatology, Allergy, and Immunology, University of North Carolina at Chapel Hill, Chapel Hill, NC

Background: Osteoarthritis (OA) is the most common joint disorder in the United States with no highly effective therapies. It is challenging for early detection and progression monitoring based on current radiographic measures, such as the radiographic Kellgren Lawrence grade (KLG) and joint space narrowing, which have low reliability and are difficult to interpret and respond poorly to change. Although knee local cartilage thickness (LCT) has been applied based on magnetic resonance imaging (MRI), there are no reference knee cartilage thickness growth charts. The aim of this work is to construct normal knee thickness reference (NKTR) charts based on 957 normal adults from a longitudinal cohort---the Osteoarthritis Initiative (OAI) dataset, which helps localize individual dynamic cartilage abnormalities among the OA patients.

Materials and Methods: We constructed two-dimensional knee LCT maps for 957 normal adults and 362 subjects with normal-OA progression. We fitted both regional and vertex-wise developmental curves through the generalized addition mixed effects model (GAMM) using longitudinal scans from the 957 subjects. The developed model accounts for effects of age, sex, body mass index (BMI) and their interactions. Z-statistics and Bonferonni adjusted p-values were calculated based on distances of individual LCT from the NKTR charts to identify abnormal subjects and localize individualized disease regions. Longitudinal prediction results were evaluated on 362 independent OA patients and compared with the KLG diagnosis.

Results: The protocol generated knee cartilage thickness growth charts at both the local and regional levels. The developed NKTR approach detects the abnormal scans among 24.1%, 20.6%, 67.1%, 93.3% and 97.4% scans with KLG = 0, 1, 2, 3, and 4, respectively. ANOVA F-test showed that NKTR diagnosis results were significantly associated with KLG scores ($p < 1e-16$).

Conclusion: Our knee cartilage thickness templates were used to quantify differences between the cartilage of individuals and these templates. The identified abnormal subjects generally match well the common clinical diagnosis criterion. About 20% of the KLG normal subjects were labeled abnormal by the NKTR method, suggesting the potential of NKTR for OA early detection as an alternative approach.

Clinical Relevance: Our study provides an anchor point for basic OA research and will facilitate implementation of research-based standards in clinical studies.
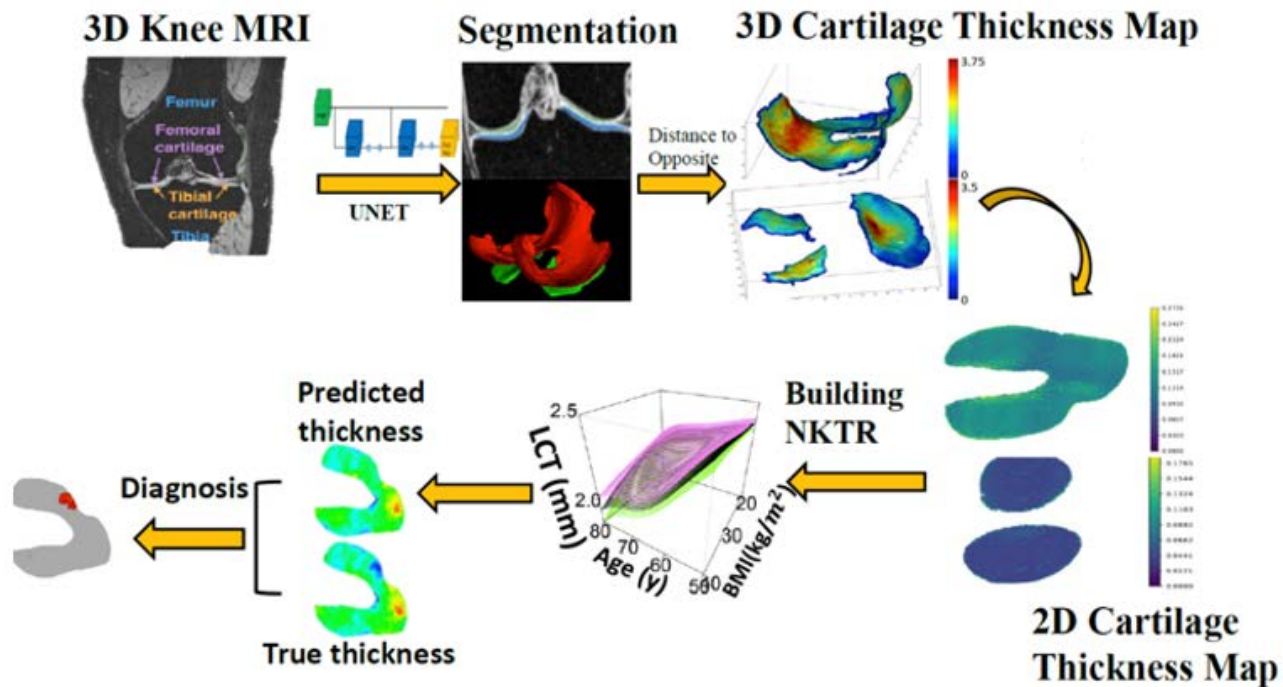
Images

Figure 1. The overall workflow of the NKTR approach.

Statement Regarding Human Subjects: In this study, we downloaded publicly available datasets (OAI datasets) and performed secondary data analyses only. Informed consent and HIPAA authorization were available from the initial OAI study https://www.nia.nih.gov/research/resource/osteoarthritis-initiative-oai.
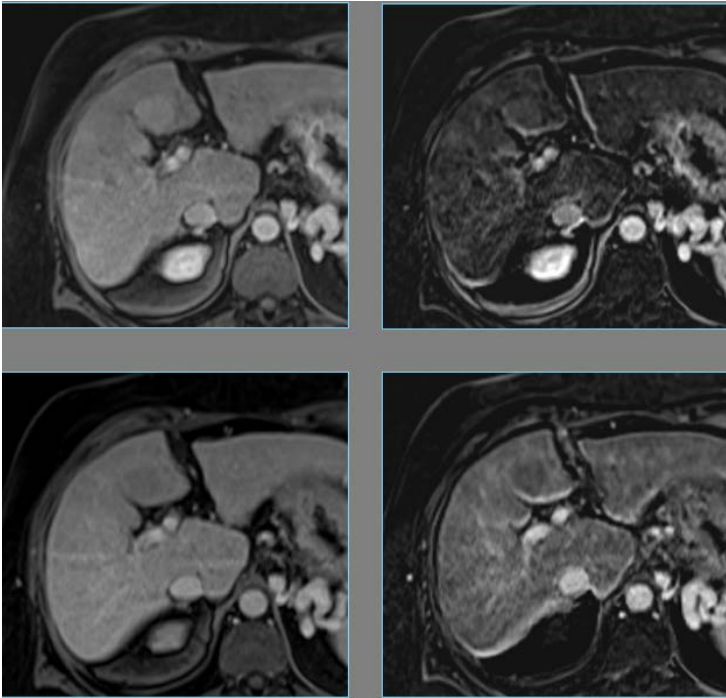
Statement Regarding Conflicts of Interest: The authors declare no conflict of financial interests.

_____

Abstract # - 44 Lumps and Bumps around the Gallbladder Fossa: A potential LI-RADS pitfall

Naishal Patel, BSPH; Vedang Patel, BS; Katrina McGinty, MD
University of North Carolina, Chapel Hill, North Carolina

LI-RADS is a valuable tool in imaging cirrhotic livers, serving as a biopsy surrogate for diagnosis of hepatocellular carcinoma. However, we have encountered multiple cases of regenerative nodules abutting the gallbladder fossa that demonstrate the arterial enhancement and washout characteristic of a LI-RADS 5 lesion but demonstrate benign pathology and stability at follow up imaging. In this exhibit, we will review appropriate use of LI-RADS, discuss regenerative nodules in cirrhosis of vascular etiologies and hypothesize about the role of third inflow phenomenon. This will be followed by a pictorial review of multiple cases of regenerative nodules abutting the gallbladder fossa mimicking hepatocellular carcinoma.

Images

Statement Regarding Human Subjects: The proposed abstract describes a case series which would completely retrospective with minimal risk to patient data.

Statement Regarding Conflicts of Interest: There are no conflicts of interest for the authors affiliated with this abstract.

_____

Abstract # - 46 Predictors of Recommended Follow-up after a Positive Lung Cancer Screening Examination

Louise M. Henderson, PhD[1]; Danielle D. Durham, PhD[1]; Pasangi S. Perera, MS[1]; Jason M. Long, MD, MPH[1]; Lindsay M. Lane, MPH[1]; Derek Lamb, BS[1]; Eman M. Metwally, MD-PhD[1]; M P Rivera MD[1,2]

[1]University of North Carolina, Chapel Hill, NC. [2]University of Rochester, Rochester, NY

Background: Cancer screening requires timely follow-up of positive test results to ensure cancer is diagnosed at an early stage. We compared rates of and identified patient factors associated with return for recommended follow-up after positive low dose CT (LDCT) lung cancer screening (LCS) exams. Methods We included individuals from five healthcare system sites who underwent LCS from 2015 to 2020 and had a positive LDCT result, defined as Lung-RADS 3, 4A, 4B, or 4X. For each individual, we determined when they returned for follow-up and the type of exam or procedure used to work up the LDCT finding. We classified receipt of follow-up based on the American College of Radiology and British Thoracic Society recommended time frames, including a grace period. Individuals with Lung-RADS 3 were classified as appropriate if they had a LDCT or CT within 9 months. Individuals with Lung-RADS 4A were classified as appropriate if they had LDCT or CT within 5 months or a PET within 2 months. Individuals with Lung-RADS 4B or 4X were classified as appropriate if they had a CT, PET, or biopsy within 2 months. We used multivariate logistic regression to determine predictors of returning for appropriate follow-up, stratified by

Lung-RADS. We evaluated and adjusted for predictors of age, race, sex, smoking status, COPD, referring provider type, and LCS exam year. We present adjusted odds ratios (aOR) and 95% confidence intervals (95%CI).

Results: Of 691 individuals with a positive LDCT, 53.0% (n=366) had Lung-RADS 3, 28.4% (n=196) had Lung-RADS 4A, and 18.7% (n=129) had Lung-RADS 4B/4X. Among individuals with Lung-RADS 3, 68.3% had appropriate follow-up with those who formerly smoked more than twice as likely to return for appropriate follow-up versus those who currently smoked (aOR=2.22, 95%CI:1.35-3.70). Among individuals with Lung-RADS 4A, 77.6% had appropriate follow-up with those with COPD almost three times more likely to return for appropriate follow-up versus those without COPD (aOR=2.96, 95%CI:1.32-6.64). Among individuals with Lung-RADS 4B/4X, 80.6% had appropriate follow-up with women more than four times as likely as men to return for appropriate follow-up (aOR=4.32, 95%CI:1.31-14.20).

Conclusion: Female sex, COPD, and smoking status are predictors of returning for appropriate follow-up after a positive LDCT. Though most individuals returned for follow-, more work is needed to understand barriers of returning to ensure timely diagnosis of early-stage lung cancer.

Statement Regarding Human Subjects: This study was approved by the University of North Carolina Institutional Review Board. The UNC IRB approved Waivers of Informed Consent and HIPAA Authorization.

Statement Regarding Conflicts of Interest: Authors have no Conflicts of Interest to disclose.

_____

Abstract # - 47 Lung Cancer Screening In Individuals With And Without Lung-related Comorbidities

Eman M. Metwally, MD-PhD[1]; M. P. Rivera, MD[1,2,]; Danielle D. Durham, PhD[1]; Lindsay M. Lane, MPH[1]; Pasangi S. Perera, MS[1]; Derek Lamb, BS[1]; Louise M. Henderson, PhD[1]

[1]University of North Carolina, Chapel Hill, NC. [2]University of Rochester, Rochester, NY

Background: Comorbidities characterize the health status of individuals eligible for lung cancer screening (LCS) and likely influence the benefits and harms of screening. We compared sociodemographic characteristics, low dose computed tomography (LDCT) findings, the cancer detection rate (CDR), and the false positive rate (FPR) among individuals undergoing LCS based on the presence of lung-related comorbidity.

Methods: We included individuals screened for lung cancer at five healthcare sites from 2014–2020 who completed a health history questionnaire (HHQ) containing risk factors of lung cancer and lung-related comorbidities. From electronic health records (EHRs) we abstracted clinical, radiological, histology, and staging data for lung cancer cases occurring within 365 days of the LCS exam. We categorized LCS examinations as positive (Lung-RADS 3, 4A, 4B, or 4X) or negative (Lung-RADS 1 or 2) based on the radiologist's report. The CDR and FPR were calculated per 100 screening exams using age-adjusted binary logistic regression. We compared sociodemographics, comorbidity, clinical, radiological findings, CDR, and FPR among those with versus without self-reported lung-related comorbidity using chi-square test and Fisher's Exact test. We also described characteristics of lung cancers diagnosed on screening.

Results: A total of 611 individuals underwent 971 LCS exams; 83.1% had at least one comorbid condition and 54.8% had at least one lung-related comorbidity. Individuals with a lung-related comorbidity were more

likely to be 70 years or older (27.7% vs 21.0%, p-value=0.004), female (53.7% vs. 44.6%, p-value=0.024), white (82.1% vs. 69.9%, p=0.0002), and have high school or less education (45.0% vs. 30.2%, p=0.001). There was no statistically significant difference in the CDR (1.57 vs.1.85, p-value=0.7312) or FPR (13.0 vs. 9.3, p-value=0.1627) for those with versus without lung related comorbidity. Of the 17 individuals diagnosed with lung cancer, 76.5% were diagnosed at an early stage (stage I or II) and 64.7% had adenocarcinoma.

Conclusion: Individuals with lung-related comorbidity undergoing LCS were older, more likely to be female, and had less education. While we found no statically significant difference in CDR or FPR, additional studies with larger numbers of screened individuals are needed to further understand LCS in those with comorbidities. Standardized comorbidity assessment during LCS is essential to maximize individual benefits from screening.

Statement Regarding Human Subjects: This study was approved by the University of North Carolina Institutional Review Board. The UNC IRB approved Waivers of Informed Consent and HIPAA Authorization.

Statement Regarding Conflicts of Interest: Authors have no conflicts of interest to disclose.

_____

Abstract # - 48 Uncommon Causes of Hemoptysis: A Post-surgical Case Study

Stephen M. Himmelberg, BS[1]; Marinelda Perleshi[1]; Clayton Commander, MD, PhD[2]

[1]UNC School of Medicine, Chapel Hill, NC. [2]UNC Hospitals, Chapel Hill, NC

Background: Hemoptysis stems from both benign and malignant disease with up to 14% of cases of hemoptysis being classified as massive, signifying a large risk for death and severe morbidity among this specific patient population (1). Commonly, bronchial arteries are the source of hemoptysis identified on angiogram in up to 90% of cases (2). However, when the source of bleeding is not attributed to the bronchial arteries this can pose a challenge to evaluate further potential bleeding sources. With our review we will focus on a selected case focusing on reviewing the patient holistically focusing on management, diagnosis, and treatment approach to uncommon causes of hemoptysis using a series of illustrative cases.

Case Study: A 75 year old male with past history of hypetrophic obstructive cardiomyopathy, atrial fibrilation, hypertension, colon cancer status post partial colectomy in 1993, and distal esophageal adenocarcinoma treated with Ivor-Lewis esophagectomy in 2018. In August 2021 the patient presented with hemoptysis leading to admission to medicine. Over a several-day period the patients hemoglobin decreased from 9.8 to 7.7 with no clear source of bleeding. He was taken for a bronchoscopy and EGD, the EGD showed clotted blood in the gastric cardia with bright red blood emanating from the proximal gastric conduit. Bronchoscopy showed bloody secretions in bilateral lower lobes, right greater than left. Given persistent active bleeding presumably within the right lower lobe of the lung and within the gastric cardia, we were consulted for potential embolization.

Access was obtained in the right common femoral artery and catheter aortogram showed no evidence of active contrast extravasation. Subsequent celiac arteriogram showed hyperemia to the gastric conduit. Selective catheter arteriogram of the right gastroepiploic artery showed opacification of a gastroepiploic to right pulmonary artery fistula. This was embolized using 400 micron Hydropearl particles and a gelfoam

slurry. Selective catheter arteriogram of the right bronchial artery shows fistulous communication with the right pulmonary artery and gelfoam embolization of a branch of the right bronchial artery was performed achieving stasis. Due to the patients prior history, along with CT correlate, we suspect this esophagectomy allowed access for his right gastroepiploic artery to be pulled through the diaphragm eventually forming a fistula with an aspect of his right pulmonary artery.
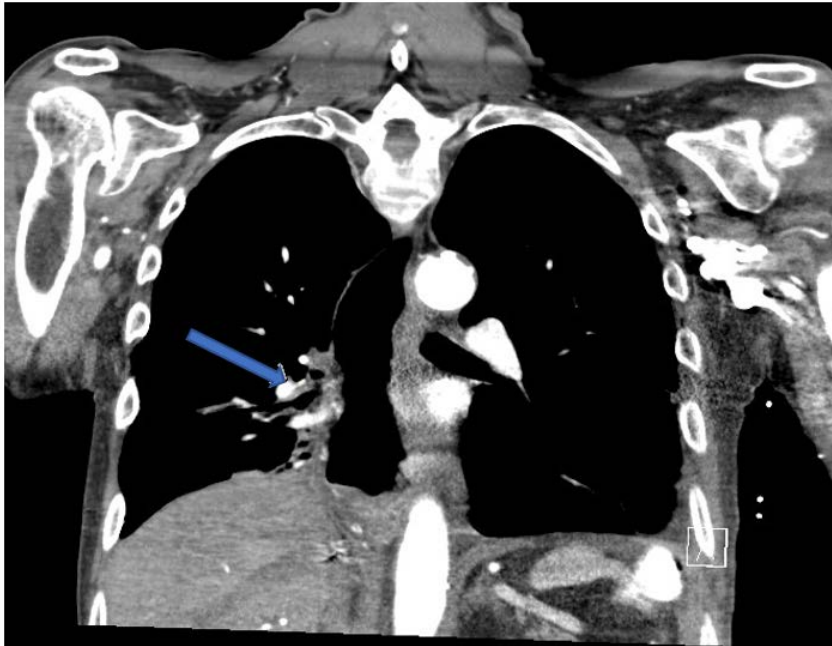
Images

Figure 1: CT scan demonstrating right gastroepiploic artery (blue arrow) to pulmonary artery fistula secondary to pull-through

Statement Regarding Human Subjects: Case study exempted from IRB approval

Statement Regarding Conflicts of Interest: No conflicts of interest

_____

Abstract # - 49 Clinical developments of a stationary head CT using CNT x-ray source arrays

Alex Billingsley, Christy Inscoe, Derrek Spronk, Yueting Luo, Otto Zhou, Jianping Lu, Yueh Lee

University of North Carolina, Chapel Hill, NC

Purpose: Benchtop experiments have proven the utility of a stationary computed tomography (CT) scanner for head imaging. The purpose of this study was for system control development and integration in a hospital setting for clinical use and evaluation. Software and interfaces for technologist operation of the complete system during patient scanning were also developed.

Method: A clinical imaging bed was integrated with the x-ray control system with off-the-shelf microcontrollers to drive the development of the system for clinical evaluation. The clinical imaging system

is composed of three carbon nanotube (CNT) x-ray source arrays and nine strip detectors. 135 projections are acquired per slice at 120kVp, 12.5mA, and 2.95ms exposure per projection. Anthropomorphic phantoms have been imaged in preparation for the first patients. Reconstruction was performed using adaptive steepest descent projection onto convex set (ASD-POCs) method. Scanner performance parameters were measured. Images are evaluated by neuroradiologists.

Results: A working stationary head CT (sHCT) system has been developed for patient imaging evaluation. Image quality is sufficient for starting the observational clinical trial as shown in images of the ACR accreditation phantom and KYOTO head phantoms.

Conclusion: This preliminary study has shown that the sHCT system is ready for patient imaging studies. Clinical utility will be assessed in a patient study with patients with prior head trauma.

Clinical Relevance: Clinical development of a scanner suitable for lower tier medical facilities for the military to reduce time to treatment for head trauma.

Image

Statement Regarding Human Subjects: No human subjects

Statement Regarding Conflicts of Interest: Otto Zhou has equity ownership and serves on the board of directors of XinRay Systems Inc., to which the technologies used or evaluated in this project may be licensed. Jianping Lu has equity ownership in XinRay. Some of the authors are inventors of a patent on the CNT x-ray source array and stationary CT technology. All relationships have been disclosed and are under management by the University of North Carolina's institutional COI committees.

Acknowledgements

UNC | SCHOOL OF MEDICINE
Radiology